ABSTRACT

Title of dissertation: RADIO ANALYTICS
                           FOR INDOOR LOCALIZATION
                           AND VITAL SIGN MONITORING

                           Chen Chen, Doctor of Philosophy, 2017

Dissertation directed by: Professor K. J. Ray Liu
                           Department of Electrical and Computer Engineering

Radio technology has been widely used for high-speed wireless communications. In the near future, radio technology would provide sensing capabilities to enable a diversified indoor applications in the era of Internet of Things (IoT). This is because that the electromagnetic (EM) wave, emitted from the transmitter propagates through multipath before arriving at the receiver, is varied by the environmental perturbations. Such variations in EM waves reveal important environmental changes useful for IoT applications. Thus, in IoT networks, radios are not only the ubiquitous communication interfaces but also exhibit augmented sensing potential.

Despite the wide variety of IoT devices, most of them are equipped with WiFi which is a very mature and cost-effective connectivity solution and has evolved significantly ever since its standardization. Meanwhile, as people are spending more and more time indoors, most indoor spaces have been already equipped with WiFi infrastructures, which makes the IoT devices empowered by WiFi to blend into the existing WiFi infrastructures without efforts. Therefore, it is highly valuable

to adopt radio analytics to analyze the WiFi radio signals to facilitate key IoT applications.

In this dissertation, we explore the viability of using WiFi for two important IoT applications: indoor localization and vital sign monitoring. In the first part, we propose two indoor localization systems (IPSs) leveraging the time-reversal (TR) technique on off-the-shelf WiFi devices. The proposed IPSs utilize the location-specific features, i.e., the channel frequency response (CFR), which is a fine-grained information readily available on off-the-shelf devices that depicts the propagation of EM waves from the transmitter to different locations. The proposed IPSs consist of an offline phase which collects CFRs from locations-of-interest, and an online phase which compares the instantaneous CFRs with those captured in the offline phase. To calculate the similarities among locations, the TR focusing effect is evaluated quantitively between each pair of CFRs associated with these locations using the TR resonating strength (TRRS). Realizing that the bandwidth limit on mainstream WiFi devices could lead to location ambiguity, we exploit two diversities inherent in WiFi devices, i.e., frequency diversity and spatial diversity, to expand the effective bandwidth. Extensive experiments show a localization accuracy of 1 to 2 centimeters even under strong non-line-of-sight (NLOS) conditions as well as enhanced robustness against environmental dynamics.

In the second part, we investigate the feasibility of high accuracy vital sign monitoring using CFRs. First of all, we present a highly accurate breathing monitoring system. Realizing that breathing injects tiny but periodic signals into the WiFi signal, we project the CFR time series onto the TRRS feature space to amplify

such CFR perturbations. Integrated with machine learning techniques, the proposed scheme could distinguish breathing rates associated with different people. In addition, it could detect the presence of breathing and count the number of people. The performance is demonstrated by extensive experiments in multiple environments. Secondly, we present a lightweight vital sign monitoring solution with a much reduced computational complexity. Moreover, we supplement the proposed vital sign monitoring system with a finite state machine (FSM) to remedy the impact of motions on the monitoring performance. Extensive experimental results demonstrate the excellent performance of both breathing monitoring schemes.

RADIO ANALYTICS FOR INDOOR LOCALIZATION
AND
VITAL SIGN MONITORING

by

Chen Chen

Dissertation submitted to the Faculty of the Graduate School of the
University of Maryland, College Park in partial fulfillment
of the requirements for the degree of
Doctor of Philosophy
2017

Advisory Committee:
Professor K. J. Ray Liu, Chair/Advisor
Professor Min Wu
Professor Gang Qu
Dr. Beibei Wang
Professor Lawrence C. Washington

Dedication

To my family—

Ming Chen, Meirong Hu

Lin Li, Cheng Li, and Liping Guo

Acknowledgments

First and foremost, I would like to express my deepest gratitude to my advisor, Prof. K. J. Ray Liu, for his guidance not only on my research but also on my life during my Ph.D. study. His pursuit of excellence on academic, research, teaching, and experiment has ignited my passion for cutting-edge radio analytics research. He always encourages me to explore unknown domains and try brand new ideas. He shepherds me patiently and shapes me into the person who is responsible, self-confident, and optimistic. I will always cherish his advice and suggestions during this long journey.

I would like to thank all of my dissertation committee members. I am grateful to Dr. Beibei Wang for her countless suggestions on my research and her patience during our discussions. Her rigorous working attitude impresses me very much. I am also thankful to Prof. Min Wu who has provided me many research ideas. I also thank Prof. Gang Qu and Prof. Lawrence Washington for being my dissertation committee and reviewing my thesis.

I would like to thank all members of Signal and Information Group for their support and help during these years. Thanks Yan Chen and Beibei Wang for providing me so many suggestions on my research; Hung-Quoc Lai for showing me the importance of knowing all details of implementation and project management; Feng Zhang for his helpful discussions and late-night company when I was conducting extensive experiments and sharing food with me; Yi Han for his working attitude and humorous; Zhung-Han Wu for his precious suggestions on writing C++

softwares; Qinyi Xu for her constructive discussions on research and on writing softwares; Chau-Wai Wong for his sharing of ideas and experiences in the diversified areas of research; Xuanyu Cao, Xiaoyu Chu, Chunxiao Jiang, Hang Ma for their support and discussions.

I thank all my friends for standing beside me. I thank Lida Lv for providing me a general picture of living and studying in the United States before I decided to pursue a Ph.D. degree at the University of Maryland College Park. I am very thankful to Shen Hui, Diyue Guo, and Hong Lin, for helping me out when I arrived in the United States on a cold night in the Baltimore area, and to their support during these years. I thank Jerry Cheng for his support since we befriended each other in Fudan University; thank Congxi Lu for his hospitality during my trip to Guangzhou as well as suggestions on travel, living, and study in the United States; thank Peisheng Wu for his long-term support overseas across the phone and screen.

Most importantly, I would like to give my deepest appreciation to my parents, Ming Chen and Meirong Hu, my girlfriend Lin Li and her parents, Cheng Li and Liping Guo. I would not be able to achieve this important academic achievement in my career without you. Your unconditional support and understanding mean everything to me during my low times and high times. This dissertation is dedicated to them.

The way ahead is long; I see no ending, yet high and low I will search with my will unbending.

iv

Table of Contents

List of Tables

List of Figures

xi

Chapter 1

Introduction

1.1 Motivation

The Internet of Things (IoT) is a novel paradigm that is gaining ground in the scenarios of modern wireless communications. The fundamental idea of this paradigm is: the things or objects — such as sensors, actuators, and mobile devices — are able to communicate with each other to accomplish common goals through unique addressing schemes. IoT has been envisioned for a long time and has finally become a reality thanks to the unprecedented development of integrated circuit (IC) technology which significantly shrinks device dimensions and costs. In terms of applicability of IoT, recent years have witnessed the revolutionary paradigm shift from mere sensor utilizations to highly complicated IoT applications covering diversified areas ranging from consumer electronics to business users, including assist-living, healthcare, enhanced learning, transport, home automation, industrial manufacturing, logistics, and so on [13]. As the IoT technology is expected to dramatically change everyday lives and behaviors of people, organizations such as Industrial Internet Consortium and IoT Acceleration are established to foster the standardization and commercialization of IoT technology. Moreover, due to its potentially huge

impact, IoT is included by the US National Intelligence Council in the list of six "Disruptive Civil Technologies" [31].

To facilitate wireless communications, IoT devices are equipped with one or even multiple radio interfaces such as WiFi [6], Bluetooth [1], Zigbee [8], Z-wave [7], etc. In addition to provide seamless connectivity among IoT devices, these radio technologies have the sensing capability to comprehend the environment [50]. This is because that the electromagnetic (EM) waves emitted by radios for information delivery propagates through the multipath environment before arriving at the receiver and is very sensitive to environmental perturbations. Such variations are embedded in EM waves and could be extracted at the receiver to reveal crucial information about the environment. Thus, IoT radios are not only the ubiquitous communication interfaces but also incorporated with augmented sensing potential. This makes radio analytics for IoT applications possible.

Among different IoT radio technologies, WiFi is a very mature technology. Since its standardization in 1997, WiFi technology undergoes significant improvements in terms of coverage, signal quality, and security [6]. Moreover, as people are spending more and more time indoor, WiFi access points (APs) have been deployed everywhere, and they could be the infrastructure to accommodate a large number of IoT devices. Therefore, it is highly valuable to implement IoT applications using WiFi signals, which is the motivation of this dissertation. More specifically, we study two IoT applications — indoor localization and vital sign monitoring.

Indoor localization is a very important application in IoT with high pragmatic value. It could enable many location-based services such as indoor navigation and

object tracking. A straightforward solution is to utilize the Global Positioning System (GPS) for indoor localization, which is, unfortunately, a non-starter due to a variety of reasons including poor signal strength, multipath effect, and limited on-device computation and communication power [45]. Thus, a WiFi-based indoor positioning system (IPS) is highly valuable since it leverages the WiFi infrastructure available in almost all indoor spaces.

Vital sign monitoring is another paramount IoT application. Thanks to the advancements in on-body sensors and wearable devices, people can now monitor their health status anywhere anytime with IoT devices. Meanwhile, the wearable monitoring systems could provide long-term, prompt, and accurate physiological data to doctors remotely. The integration of IoT technology and wearable sensors have already made the remote vital sign monitoring a reality and could potentially improve the life qualities of millions of people. The WiFi-based vital sign monitoring solutions could make the IoT-based healthcare system even better since it is non-invasive, infrastructure-free, and could work remarkably well even if the subject under monitoring is not in the same room as the WiFi radio.

1.2   Dissertation Outline and Contributions

From the previous discussions, we can see the significance of using WiFi signals to accomplish IoT applications. In this dissertation, we focus on WiFi-based indoor localization and vital sign monitoring. For the proposed systems, we exploit the channel frequency response (CFR), a location-specific WiFi signal available on

off-the-shelf WiFi devices that contains rich information about the environment. The first part of this dissertation focuses on the implementation of centimeter-level indoor localization systems using the TR technique, and the second part of this dissertation focuses on the implementation of breathing monitoring systems with different complexities and architectures. The rest of this dissertation is organized as follows.

1.2.1   Channel Frequency Response and Time-Reversal (Chapter 2)

In this chapter, firstly, we introduce the CFR models in the presence of inevitable phase distortions caused by synchronization errors in WiFi systems. Then, we explain the way to extract CFRs from WiFi signals by introducing the channel estimation algorithms in both single-input-single-output (SISO) and multiple-input-multiple-output (MIMO) orthogonal frequency-division multiplexing (OFDM) WiFi systems. After that, we present the CFR models for indoor localization and vital sign monitoring.

Secondly, we elaborate on the TR technique and present the calculation of TR resonating strength (TRRS) to quantify the similarities among CFRs, which lays the foundation of the proposed indoor localization and vital sign monitoring systems.

1.2.2 Time-Reversal Indoor Positioning with Frequency Diversity (Chapter 3)

In this chapter, we propose a centimeter-level accuracy indoor localization system using commercial WiFi. Considering the lack of physical bandwidth on mainstream WiFi systems which leads to location ambiguity, we propose to utilize frequency hopping to obtain CFRs from a multitude of WiFi channels and concatenate these CFRs into location fingerprints. This leads to a much larger effective bandwidth and greatly reduces the location ambiguity. The proposed system consists of an offline phase to collect CFRs from locations-of-interest and an online phase for indoor localization based on instantaneous CFRs. The similarities among locations are characterized by the TRRS calculated based on the associated CFRs with these locations as introduced in Chapter 2. Extensive experimental results show that a centimeter-level indoor localization is achievable even under a strong NLOS condition.

1.2.3 Time-Reversal Indoor Positioning with Spatial Diversity (Chapter 4)

In this chapter, we propose an indoor localization system harvesting spatial diversity to achieve a centimeter-level localization accuracy. Different from Chapter 3 where frequency hopping is adopted, we make full use of the multiple antenna links in MIMO-OFDM systems to achieve a large effective bandwidth. In addition to demonstrating the centimeter-level accuracy, we conduct many experiments in the

presence of environmental dynamics to show the robustness of the proposed system.

1.2.4   High Accuracy Vital Sign Monitoring (Chapter 5)

In this chapter, we propose a high accuracy vital sign monitoring system using commercial WiFi and TR signal processing technique, termed as TR-BREATH. TR-BREATH extracts useful information relevant to human breathing embedded in CFRs by performing TRRS calculation and spectral analysis via Root-MUSIC algorithm. Moreover, TR-BREATH is able to detect the presence of breathing leveraging machine learning techniques. In case that the people number under monitoring is unknown, TR-BREATH could formulate an estimation of the people number as well. Extensive experimental results demonstrate that TR-BREATH could resolve the breathing rates from a total of 12 people under a LOS condition and up to 7 people under an NLOS condition, and TR-BREATH could estimate the number of people within an error of 1 person. Meanwhile, TR-BREATH can achieve a perfect detection performance.

1.2.5   Robust Vital Sign Tracking (Chapter 6)

In this chapter, we present a robust and lightweight vital sign tracking system. To concentrate the energy of breathing signal, the proposed scheme performs inverse Fourier transform to convert CFRs into CIRs. Then, it performs spectral analysis on multiple channel taps in CIRs and combines the spectrum from multiple antenna links. To mitigate the impact of motion, the proposed scheme incorporates

a finite state machine (FSM) to automatically tune the parameters for breathing monitoring under different scenarios. Extensive experiments show the robustness of the proposed system.

Chapter 2

Channel Frequency Response and Time-Reversal

In the proposed indoor localization and vital sign monitoring systems, CFR plays a paramount role as it captures centimeter-level changes of device locations as well as centimeter-level chest displacement. In this chapter, we present a detailed introduction to CFR, including a brief discussion of the phase distortion that affects the CFR quality and an explanation on why CFRs can be used for indoor localization and vital sign monitoring.

Then, we introduce the time-reversal signal processing technique which is utilized in the proposed indoor localization and Root-MUSIC-based vital sign monitoring systems for both SISO-OFDM and MIMO-OFDM systems. Furthermore, we introduce the concept of effective bandwidth to measure the available bandwidth resources for IoT applications.

2.1 Channel Frequency Response

2.1.1 Multipaths Propagation

In wireless telecommunications, multipath is the propagation phenomenon that results in radio signals reaching the receiving antenna by two or more paths.

Causes of multipath include atmospheric ducting, ionospheric reflection and refraction, and reflection from water bodies and terrestrial objects such as mountains and buildings [34].
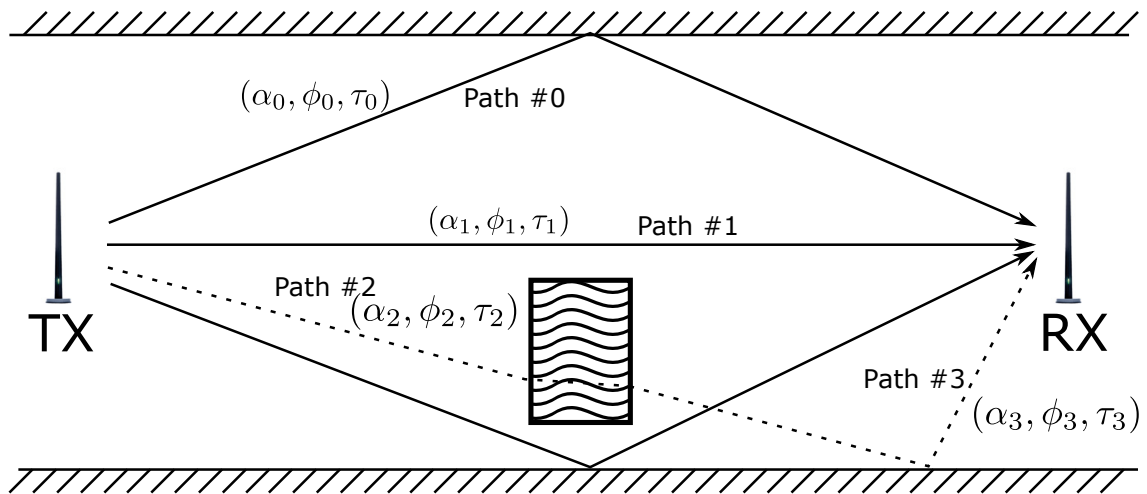
Figure 2.1: Illustration of multipath propagation

Due to this phenomenon, the received signal is a superposition of multiple scaled, phase shifted, and delayed replicas of the transmitted signal. Denote the transmitted waveform as $x(t)$, the received signal $y(t)$ can be written as

$$y(t) = \sum_{\ell=0}^{L-1} h_\ell(t)x(t - \tau_\ell(t)) + w(t) \tag{2.1}$$

where $w(t)$ is the receiver noise and $\tau_\ell(t)$ is the time delay of the ℓ-th channel coefficient. $h_\ell(t)$ is the complex channel coefficient at time t and can be expressed as $\alpha_\ell(t)e^{j\phi_\ell(t)}$ where α_ℓ is the magnitude of multipaths component (MPC) ℓ and $\phi_\ell(t)$ is the phase of MPC ℓ at time t. Eqn. (2.1) shows that the received signal $y(t)$ can be either significantly attenuated in case that $h_\ell(t)x(t - \tau_\ell(t))$ are combined incoherently, or improved in case that $h_\ell(t)x(t - \tau_\ell(t))$ are accumulated coherently.

In a static environment, $(\alpha_\ell(t), \phi_\ell(t), \tau_\ell(t))$ can be considered as time-invariant and substituted as $(\alpha_\ell, \phi_\ell, \tau_\ell)$. In this scenario, the multipath channel can be treated as a time-invariant finite impulse response (FIR) filter given as

$$h(t) = \sum_{\ell=0}^{L-1} \alpha_\ell e^{j\phi_\ell} \delta(t - \tau_\ell) \tag{2.2}$$

where $\delta(t)$ is the Dirac function. $h(t)$ is generally referred as CIR with continous time.

Fig. 2.1 visualizes the multipaths propagation. There are in total 4 MPCs, with MPC #1 as one line-of-sight (LOS) MPC and the others non-line-of-sight (NLOS) MPC. MPC #2 is a fully occluded path that experiences reflection and diffraction. As EM wave penetrates through objects, signals traveled on MPC #2 can still reach the receiver with a much reduced energy.

2.1.2 Multipath Channel in OFDM Systems

The multipath propagation could introduce very severe inter-symbol-interference (ISI) in single-carrier communication schemes [46, 69]. To mitigate this impact, multi-carrier communication schemes such as the orthogonal frequency-division multiplexing (OFDM) are generally used. In OFDM systems, data are transmitted on multiple subcarriers in parallel. The waveform of each subcarrier is orthogonal to the waveforms on the other subcarriers. An example is shown in Fig. 2.2 with four subcarriers f_1, f_2, f_3, f_4. As we can see, there is no interference between different subcarriers under ideal situations. Since the spacing between adjacent subcarriers is very narrow, the multipath channel can be regarded as a one-tap complex scalar
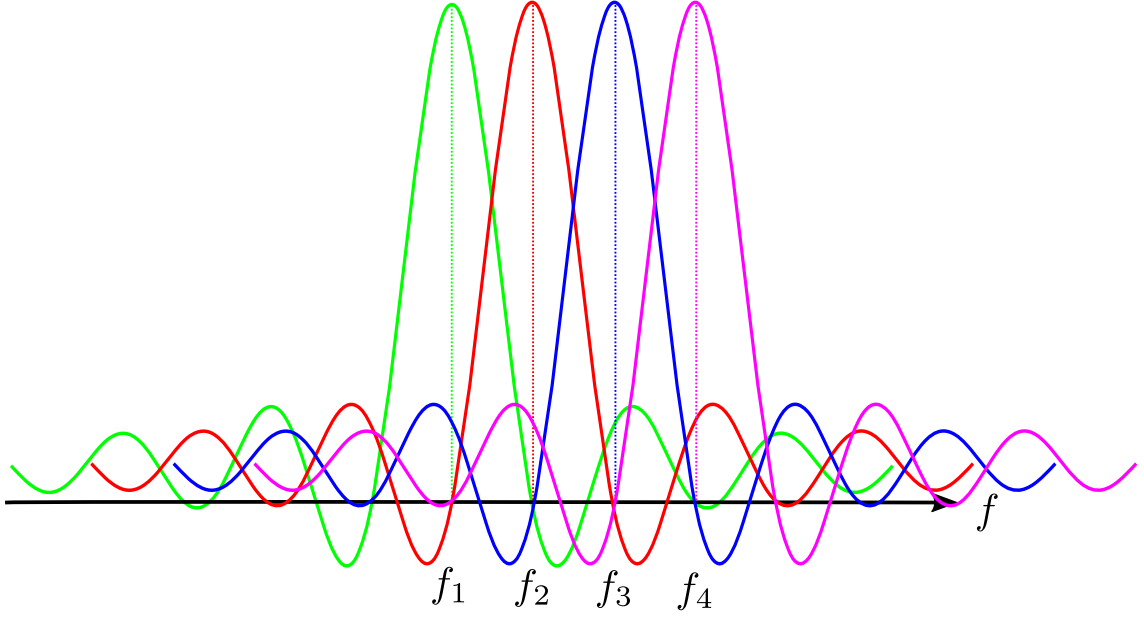
Figure 2.2: An illustration of the orthogonal waveforms used in OFDM systems

for each subcarrier.

Therefore, the multipath channel exhibits itself as a vector composed by the complex scalars on each subcarrier in OFDM systems [24, 53, 54], known as CFR. Mathematically, CFR is the discrete Fourier transform (DFT) of the discrete CIR presented in (2.2) that takes the form

$$H_{u_k} = \sum_{\ell=0}^{L-1} \alpha_\ell e^{j\phi_\ell} e^{-2\pi \tau_\ell \frac{u_k}{NT_s}}, \;\; k = 1, 2, \cdots, K \qquad (2.3)$$

where u_k is the subcarrier index for the k-th subcarrier, K is the total number of usable subcarriers which is the number of subcarriers used for data transmission, N is the size of the DFT as well as the number of samples for each OFDM symbol.
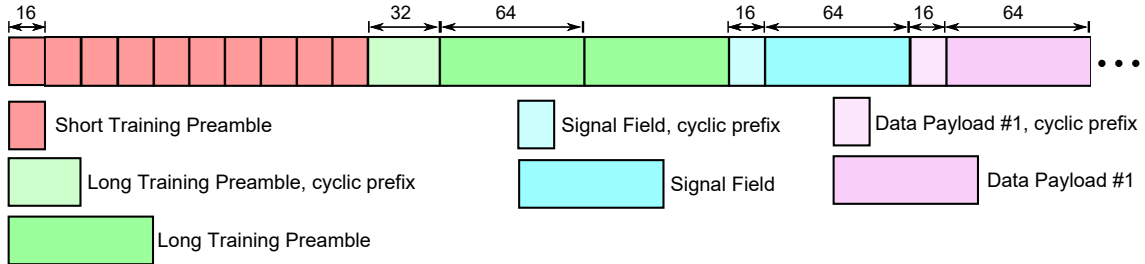
Figure 2.3: Frame structure in 802.11a OFDM systems.

2.1.3 Channel Estimation in SISO-OFDM Systems

First of all, we introduce the channel estimation scheme in single-input-single-output (SISO) OFDM systems. To facilitate accurate channel estimations, OFDM transmitter emits specialized OFDM symbols, known as the training preambles, to the receiver. The training preambles can be further classified into two classes: short training preambles (STP) and long training preambles (LTP). STP is utilized for symbol timing synchronization and coarse carrier frequency offset estimation, while LTP is used for fine carrier frequency offset estimation as well as channel estimation [24]. Cyclic prefix (CP) blocks are also inserted to protect different OFDM symbols against multipath propagation. An example of the frame structure for 802.11a OFDM system is shown in Fig. 2.3. Denote the length of a STP as L_{STP}, the length of a LTP as L_{LTP}, the length of a CP for the LTP as $L_{CP,LTP}$, the length of a CP for the data block as L_{CP}, the length of a data block as L_{data}, we have $L_{STP} = 16$, $L_{LTP} = 64$, $L_{CP,LTP} = 32$, $L_{CP} = 16$, $L_{data} = 64$ for the 802.11a OFDM system.

Here, we focus on the LTP since it provides us the estimated CFR. Assume that the received OFDM symbols in frequency domain on subcarrier u_k is written

as Y_{u_k} and the transmitted OFDM symbol on subcarrier u_k as X_{u_k}, we have

$$Y_{u_k} = H_{u_k}X_{u_k} + W_{u_k}, \ \ k = 1, 2, \cdots, K \tag{2.4}$$

where W_{u_k} is the frequency-domain noise on subcarrier u_k and is considered as white Gaussian noise with zero mean and variance σ_w^2. (2.4) can be written into its matrix form as

$$\mathbf{Y} = \mathbf{XH} + \mathbf{W} \tag{2.5}$$

where $\mathbf{Y}$ is the $K \times 1$ column vector for the received signal expressed as $[Y_{u_1}, Y_{u_2}, \cdots, Y_{u_K}]^T$, $\mathbf{X}$ is the $K \times K$ diagonal matrix with its diagonal elements given by $\{X_{u_k}\}_{k=1,2,\cdots,K}$, $\mathbf{H}$ is the $K \times 1$ column vector given as $[H_{u_1}, H_{u_2}, \cdots, H_{u_K}]^T$.

The most intuitive way of estimating $\mathbf{H}$ from $\mathbf{Y}$ is the least-square (LS) estimation [56] which aims at minimizing $||\mathbf{Y} - \mathbf{XH}||_2^2$, i.e, the ℓ_2 norm of $\mathbf{Y} - \mathbf{XH}$, which leads to the estimation $\widehat{\mathbf{H}} = \mathbf{X}^{-1}\mathbf{H}$ where $\mathbf{X}^{-1}$ is the inverse matrix of $\mathbf{X}$. In other words, the k-th element of $\widehat{\mathbf{H}}$ can be written as

$$\widehat{H}_{u_k} = \frac{Y_{u_k}}{X_{u_k}} = H_{u_k} + \frac{W_{u_k}}{X_{u_k}} \ . \tag{2.6}$$

Eqn. (2.6) is also known as the zero-forcing solution and suffers from noise amplification when X_{u_k} is very small on some k. However, due to its low complexity, the LS channel estimator is widely used in commercial WiFi chips.

2.1.4 Impacts of Timing and Frequency Synchronization Errors on CFRs

Eqn. (2.6) is only valid in the absence of timing and frequency synchronization errors, which cannot be neglected in reality. The synchronization errors mainly stem from two sources:

Misalignment of RF components: the RF components on the transmitter and receiver are not exactly the same even if they are manufactured by the same vendor.

- The first discrepancy is the up-conversion and down-conversion center frequencies at the transmitter and receiver. More specifically, during the up-conversion process, the transmitter modulates the baseband signal onto a much higher center frequency known as the carrier frequency and denoted as f_c^{Tx}. The receiver down-converts the carrier signal to the baseband by a carrier frequency f_c^{Rx} which is not necessarily the same as f_c^{Tx}, known as the carrier frequency offset (CFO) given as $\Delta f = f_c^{Tx} - f_c^{Rx}$. Given L_{LTP} samples for each LTP and a sampling interval of T_s, the normalized CFO ϵ can be written as $\Delta f L_{LTP} T_s$ in the duration of LTP blocks.

- The second discrepancy is the sampling frequency at the transmitter and receiver, known as the sampling frequency offset (SFO) denoted as η. Given a sampling interval of T_s at the transmitter side and a sampling
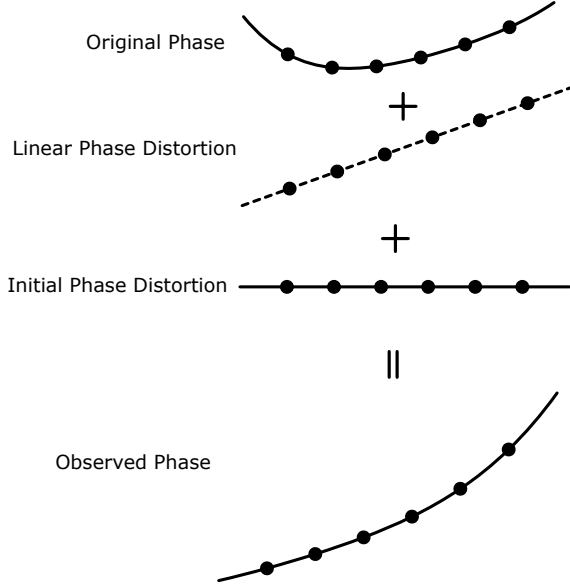
Figure 2.4: Observed phase under the influence of CFO, SFO, and STO.

interval of T_s' at the receiver side, η can be expressed as $(T_s' - T_s)/T_s$.

Error in Coarse Timing synchronization: OFDM receivers perform coarse timing syn-
chronization to localize the starting position of the first OFDM symbol utiliz-
ing the STFs appended before LTFs [57]. Nevertheless, the presence of channel
noise and multipath propagation give rise to estimation errors of the starting
position. Assume that the ground-truth starting position of the first OFDM
symbol is n_0 and the estimated starting position is n_0' instead, the difference
$\Delta n_0 = n_0 - n_0'$ is known as the symbol timing offset.

Both SFO and STO introduces linear phase offset which grows with the subcarrier
index, and CFO introduces initial phase offset which is constant for each OFDM
symbol. In Fig. 2.4, we show an example of the impact of different synchronization
errors on the overall phase.

The OFDM receiver performs timing and frequency synchronizations to re-

move the major part of these errors before channel estimation. However, the residual errors cannot be neglected and thus affect the CFRs. Denote the residual CFO, SFO, and STO errors as $\Delta\epsilon$, $\Delta\eta$, and Δn_0 respectively, and write the estimated CFR associated with the i-th received OFDM symbol on the k-th subcarrier as $\widehat{H_{i,u_k}}$. With residual synchronization errors and channel noise, $\widehat{H_{i,u_k}}$ can be modified from (2.6) into [24]

$$\widehat{H_{i,u_k}} = \mathrm{sinc}(\pi(\Delta\epsilon + \Delta\eta u_k))H_{u_k}e^{j2\pi(\beta u_k + \zeta)} + W_{i,u_k} \qquad (2.7)$$

for $k = 1, 2, \cdots, K$, where

$$\beta = \frac{\Delta n_0}{L_{LTP}} + \left(\frac{1}{2} + \frac{iL_s + L_{CP,LTP}}{L_{LTP}}\right)\Delta\eta \qquad (2.8)$$

$$\zeta = \left(\frac{1}{2} + \frac{iL_s + L_{CP}}{L_{LTP}}\right)\Delta\epsilon \qquad (2.9)$$

are the initial and linear phase distortions respectively. $\mathrm{sinc}(\pi(\Delta\epsilon + \Delta\eta u_k))$ is the amplitude attenuation. L_s is given as $L_{LTP} + L_{CP}$, and W_{i,u_k} is the estimation noise on subcarrier u_k for the i-th OFDM symbol that can be modeled as white Gaussian noise [54].

For typical values of $\Delta\epsilon$ and $\Delta\eta$, $\mathrm{sinc}(\pi(\Delta\epsilon + \Delta\eta u_k))$ can be approximated as 1. Ignoring the subscript i in $\widehat{H_{i,u_k}}$, the approximated expression of the channel estimation under synchronization errors and channel noise is

$$\widehat{H_{u_k}} = H_{u_k}e^{j2\pi(\beta u_k + \zeta)} + W_{u_k} \qquad (2.10)$$

2.1.5 Channel Estimation in MIMO-OFDM Systems

The scheme of channel estimation in SISO-OFDM can be extended to the multiple-input-multiple-output (MIMO) OFDM systems [55]. Given a MIMO-OFDM

system equipped with N_{tx} transmitting antennas and N_{rx} receiving antennas, the CFR between transmitting antenna n_{tx} and receiving antenna n_{rx} can be written as

$$\widehat{H_{u_k}^{n_{tx},n_{rx}}} = H_{u_k}^{n_{tx},n_{rx}} e^{j2\pi(\beta^{n_{tx},n_{rx}}u_k + \zeta^{n_{tx},n_{rx}})} + W_{u_k}^{n_{tx},n_{rx}} \tag{2.11}$$

where $\beta^{n_{tx},n_{rx}}$ is the linear phase offset slope for the i-th OFDM symbol on link (n_{tx}, n_{rx}), $\zeta^{n_{tx},n_{rx}}$ is the initial phase offset for the i-th OFDM symbol on link (n_{tx}, n_{rx}), and $W_{u_k}^{n_{tx},n_{rx}}$ is the channel noise of the i-th OFDM symbol on link (n_{tx}, n_{rx}).

Fig. 2.5 visualizes a conventional scheme for estimating CFRs in a MIMO-OFDM system with $N_{tx} = 3, N_{rx} = 3$. As we can observe, when any transmitting antenna is emitting training symbols, the other two remain silent so that each receiving antenna could uniquely estimate the channel between the transmitting antenna to itself. For example, when transmitting antenna 1 is emitting signals, the three receiver antennas could estimate $\{\widehat{H_{u_k}^{1,1}}\}_{k=1,2,\cdots,K}$, $\{\widehat{H_{u_k}^{1,2}}\}_{k=1,2,\cdots,K}$, and $\{\widehat{H_{u_k}^{1,3}}\}_{k=1,2,\cdots,K}$ respectively. When transmitting antenna 2 is emitting, the receiver obtains $\{\widehat{H_{u_k}^{2,1}}\}_{k=1,2,\cdots,K}$, $\{\widehat{H_{u_k}^{2,2}}\}_{k=1,2,\cdots,K}$, and $\{\widehat{H_{u_k}^{2,3}}\}_{k=1,2,\cdots,K}$, respectively. The same procedure is repeated until CFRs on all links are estimated.

To illustrate the impact of phase distortions on CFRs in MIMO-OFDM systems, we show the normalized amplitudes and phases of 200 CFRs captured within 4 seconds in Fig. 2.6(a) and Fig. 2.6(b). The total number of usable subcarriers is 114 with $\{u_k\}_{k=1,2,\cdots,114} = \{-58, -57, \cdots, -2, 2, 3, \cdots, 57, 58\}$. Despite the consistency in the normalized amplitudes, the variations in the phases caused by the aforementioned initial and linear phase distortions are very distinctive.

17
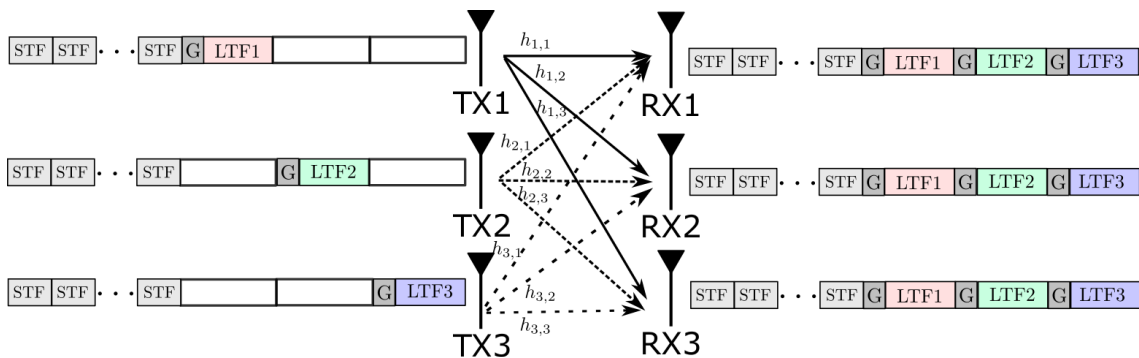
Figure 2.5: Channel estimation in MIMO-OFDM WiFi system.
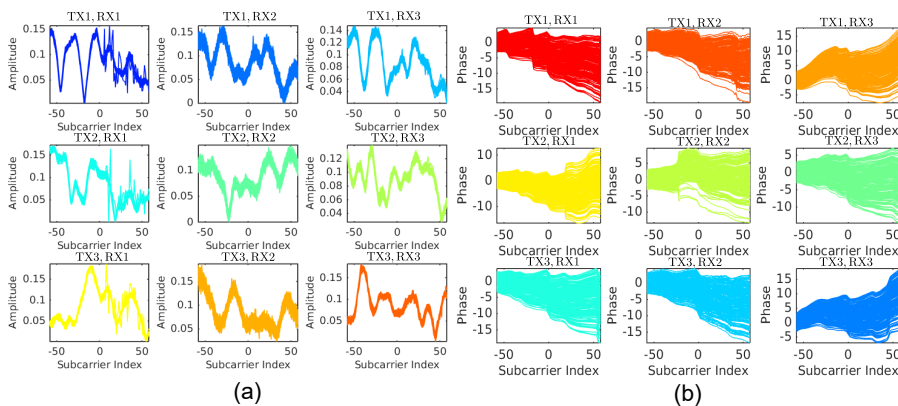
Figure 2.6: A snapshot of CFRs of 9 links in a 3×3 MIMO-OFDM system collected in 4 seconds with a bandwidth of 40 MHz. (a) Normalized amplitudes (b) Unwrapped phases.

In the next two sections, we explain why CFRs can be utilized for indoor localization and vital sign monitoring. For convenience, SISO-OFDM CFR model is utilized.

2.1.6 Channel Frequency Response Model for Indoor Localization

Fig. 2.7 shows the multipath profiles associated with two different locations. The location difference leads to very different channel profiles and thus different CFRs. In fact, under an ideal scenario, two CFRs would be highly uncorrelated if they are obtained at two locations with a distance larger than the half wavelength, which is around 2.5862 cm for the 5 GHz industrial, scientific, and medical radio (ISM) band for WiFi systems. This indicates the feasibility of using CFR as the location-specific feature, denoted as the *fingerprint*, for centimeter-level indoor localization.
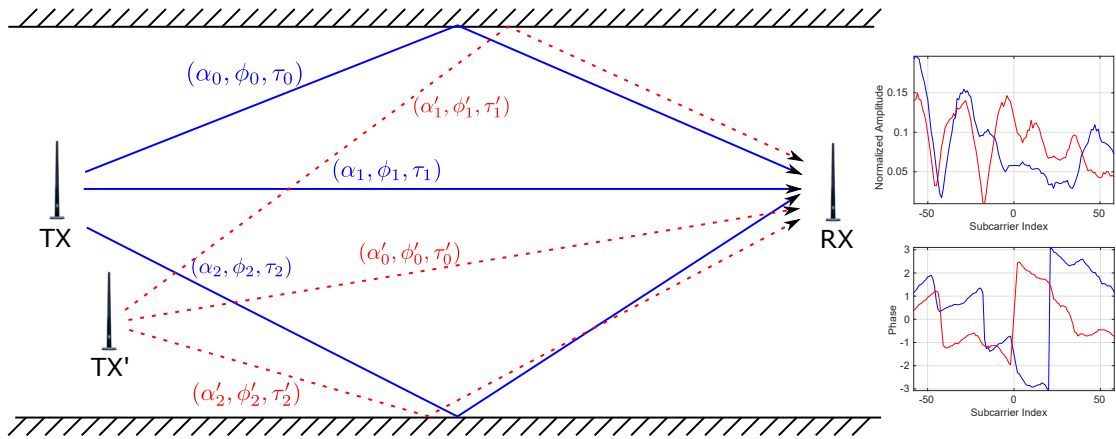
Figure 2.7: Model of CFR for indoor localization.

19

2.1.7 Channel Frequency Response Model for Vital Sign Monitoring

Fig. 2.8 shows the interaction between the subject under vital sign monitoring and the CFR. Different from the indoor localization scheme shown in Fig. 2.7, the location of the transmitter and receiver are fixed in this scheme, known as the device-free scheme. As can be seen from Fig. 2.8, the chest displacement of the subject on the order of several centimeters incorporates very small variations into MPC #0. Under the scenario of breathing, such displacement is periodic in time and thus introduces periodic variations of MPC #0. Since MPC #0 contributes to the overall multipath profile and thus perturbs CFR, it is feasible to perform breathing monitoring utilizing CFRs.
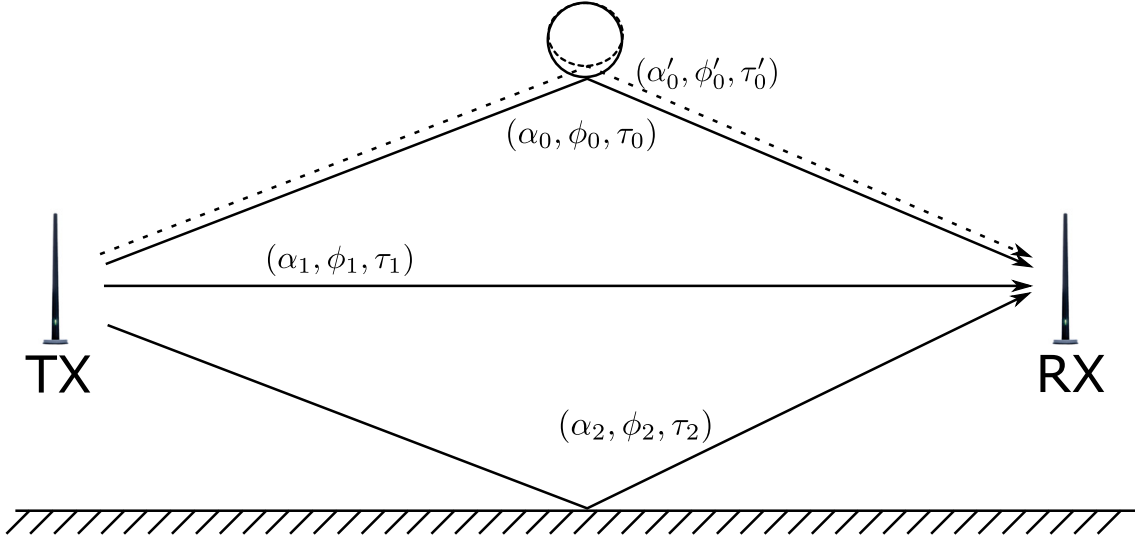
Figure 2.8: Model of CFR for vital sign monitoring.

Now, we study the impact of chest displacement on CFRs in details. Using the simplified model in Fig. 2.7, the gain of MPC #0 is time-varying and takes the

form [34]

$$\alpha_0(t) = \alpha_0 \times \left(1 + \frac{\Delta d_0}{d_0} \sin\theta \sin(\frac{2\pi b}{60}t + \phi)\right)^{-\psi} \tag{2.12}$$

where α_0 and d_0 are the path gain and path length of MPC #0 without breathing, Δd_0 is the displacement of MPC #0 under breathing, ψ is the path-loss exponent, θ is the angle between the subject and the impinging EM wave, b is the breathing rate measured in BPM, ϕ is the initial phase of breathing. Given that $d_0 \gg \Delta d_0$, we can approximate $\alpha_0(t)$ with the time-invariant MPC gain α_0.

On the other hand, breathing affects the phase of MPC #0 by changing its path length $d_0(t)$ expressed as

$$d_0(t) = d_0 + \Delta d_0 \sin\theta \sin(\frac{2\pi b}{60}t + \phi) \ . \tag{2.13}$$

Now, (2.10) can be rewritten as

$$\widehat{H_{u_k}}(t) = \left[\alpha_0 e^{-j2\pi \frac{d_0(t)}{\lambda_{u_k}}} + \sum_{\ell=1}^{L-1} \alpha_\ell e^{-j2\pi \frac{d_\ell}{\lambda_{u_k}}}\right] e^{j2\pi(\beta(t)u_k + \zeta(t))} + W_{u_k}(t) \ , \tag{2.14}$$

which can be further written as

$$\widehat{H_{u_k}}(t) = \left[\alpha_0 e^{-j2\pi \frac{d_0}{\lambda_k}} e^{-j2\pi \frac{\Delta d_0 \sin\theta \sin(\frac{2\pi b}{60}t + \phi)}{\lambda_{u_k}}} + \sum_{\ell=1}^{L-1} \alpha_\ell e^{-j2\pi \frac{d_\ell}{\lambda_{u_k}}}\right] e^{j2\pi(\beta(t)u_k + \zeta(t))} + W_{u_k}(t) \ , \tag{2.15}$$

where λ_{u_k} is the wavelength of subcarrier u_k given by

$$\lambda_{u_k} = \frac{c}{f_c + \frac{u_k}{L_{LTP}T_s}} \ , \tag{2.16}$$

where f_c is the carrier frequency, c is the speed of the light, T_s is the sampling interval given as $T_s = 1/B$ where B is the baseband bandwidth of the WiFi signal.

The first term on the right hand side of $\widehat{H_{i,u_k}}(t)$ in (2.15) can be decomposed into an infinite summation according to the Jacobi-Anger expansion [10] as

$$e^{-j2\pi \frac{\Delta d_0 \sin\theta \sin(\frac{2\pi b}{60}t+\phi)}{\lambda_{u_k}}} = \sum_{m=-\infty}^{+\infty} (-1)^m J_m(\nu_{u_k}) e^{jm\frac{2\pi b}{60}t} e^{jm\phi} \qquad (2.17)$$

where $\nu_{u_k} = 2\pi \sin\theta \Delta d_0/\lambda_{u_k}$ and $J_m(x)$ is the m-th order Bessel function with argument x. It can be seen that in addition to the spectral line at b, there also exists an infinite number of harmonics with spectral lines at mb where m is a non-zero integer.

In practice, $J_m(\nu_{u_k})$ decays quickly for $|m| \geq 2$ given the typical values of ν_{u_k}, and (2.17) can be approximated as

$$e^{-j2\pi \frac{\Delta d_0 \sin\theta \sin(\frac{2\pi b}{60}t+\phi)}{\lambda_{u_k}}} \approx \sum_{m=-1}^{+1} (-1)^m J_m(\nu_{u_k}) e^{jm\frac{2\pi b}{60}t} e^{jm\phi} \qquad (2.18)$$

which consists of two spectral lines at $\pm b$ with respect to $m = \pm 1$ as well as a DC component with respect to $m = 0$. Thus, $\widehat{H_{u_k}}(t)$ can be expressed as

$$\widehat{H_{u_k}}(t) \approx \left[\underbrace{\alpha_0 e^{-j2\pi \frac{d_0}{\lambda_{u_k}}} \sum_{m=-1}^{+1} (-1)^m J_m(\nu_{u_k}) e^{jm\frac{2\pi b}{60}t} e^{jm\phi}}_{S_{u_k}(t)} + \underbrace{\sum_{\ell=1}^{L-1} \alpha_\ell e^{-j2\pi \frac{d_\ell}{\lambda_{u_k}}}}_{I_{u_k}} \right]$$

$$\times e^{j2\pi(\beta(t)u_k + \zeta(t))} + W_{u_k}(t) , \qquad (2.19)$$

where $S_{u_k}(t)$ stands for the useful signal for breathing monitoring on subcarrier u_k, and I_{u_k} represents the time-invariant part due to the static environment and regarded as the interference. Eqn. (2.19) shows that the temporal variation of CFR contains the breathing frequency along with the harmonic frequencies.

2.2 Time-Reversal

In this section, we introduce the time-reversal technique, the core algorithm that calculates the similarity among CFRs used in indoor localization and vital sign monitoring. First of all, we briefly introduce the history of time-reversal (TR) technique. Secondly, we introduce the calculation of time-reversal resonating strength (TRRS), a metric that evaluates the TR focusing effect quantitatively, in both SISO-OFDM and MIMO-OFDM systems.

2.2.1 History of Time-Reversal

TR is a signal processing technique that could focus the energy of the wave onto the source location from where the wave is emitted [30]. The history of TR dates back to 1950's when Bogert uses TR to correct delay distortion in a slow-speed picture transmission system [16]. Later, it is shown by Amoroso that the TR waveform is the optimal solution to a constrained optimization problem in digital communications [12]. An important property of TR is the spatial-temporal focusing effect: the energy of signal waves is concentrated at a specific location in the space and at a specific time instance. This effect is verified experimentally using ultrasonic and acoustics waves [28, 29], and later with electromagnetic waves [59].

Thanks to the focusing effect, TR is widely used in a variety of applications. In [27], Devaney utilized TR-MUSIC algorithm to resolve targets within a certain area, known as TR imaging. The performance of TR-MUSIC is studied in [25] and its stability is analyzed in [26]. Moura and Jin adopted TR in a single antenna

system and later an antenna array for target detection in highly cluttered environment [38, 42]. Moreover, TR is a promising candidate in future 5G communication systems, since it could collectively address the major challenges in indoor wireless communications, thanks to its massive multipath effect, high capacity, and scalability [22]. In [35], Han *et al.* presented a TR-based multi-user multiple access wireless communication system.

Additionally, TR is a promising paradigm for green internet-of-things (IoT) by extending the battery life, accommodating low-cost and heterogeneous terminals, and providing physical layer security [23, 36]. Applications of TR in IoT include centimeter-level indoor localization [21, 61], human recognition [64], event detection [65], speed estimation [68], and monitoring of vital signs [20].

2.2.2 Calculating Time-Reversal Resonating Strength in SISO-OFDM Systems

To characterize the time-reversal focusing effect quantitatively, TRRS is calculated as follows.

$$\mathcal{TR}[\widehat{\mathbf{H}}, \widehat{\mathbf{H'}}] = \left| \mathcal{TR}_{\phi^\star}[\widehat{\mathbf{H}}, \widehat{\mathbf{H'}}] \right|^2, \tag{2.20}$$

$$\mathcal{TR}_{\phi^\star}[\widehat{\mathbf{H}}, \widehat{\mathbf{H'}}] = \frac{\eta}{\sqrt{\Lambda}\sqrt{\Lambda'}} , \tag{2.21}$$

with

$$\eta = \sum_{k=1}^{K} \widehat{H_{u_k}} \widehat{H'^*_{u_k}} e^{-ju_k\phi^\star} \tag{2.22}$$

$$\phi^\star = \underset{\phi}{\operatorname{argmax}} \left| \sum_{k=1}^{K} \widehat{H_{u_k}} \widehat{H'^*_{u_k}} e^{-ju_k\phi} \right| \tag{2.23}$$

$$\Lambda = \sum_{k=1}^{K} |\widehat{H_{u_k}}|^2 \tag{2.24}$$

$$\Lambda' = \sum_{k=1}^{K} |\widehat{H'_{u_k}}|^2 \tag{2.25}$$

where $\widehat{\mathbf{H}} = [\widehat{H_{u_1}}, \widehat{H_{u_2}}, \cdots, \widehat{H_{u_K}}]^T$ and $\widehat{\mathbf{H'}} = [\widehat{H'_{u_1}}, \widehat{H'_{u_2}}, \cdots, \widehat{H'_{u_K}}]^T$ represent two CFR vectors either from the same locations or two different locations, x^* is the conjugate of argument x, η is the modified cross-correlation between $\widehat{\mathbf{H}}$ and $\widehat{\mathbf{H'}}$ with synchronization error compensated, and Λ, Λ' are the channel energies of $\widehat{\mathbf{H}}$ and $\widehat{\mathbf{H'}}$, respectively. Notice that in calculating $\mathcal{TR}[\widehat{\mathbf{H}}, \widehat{\mathbf{H'}}]$, we compensate the initial and linear phase distortions by employing $e^{-ju_k\phi^\star}$ in η as well as taking absolute value on $\mathcal{TR}_{\phi^\star}[\widehat{\mathbf{H}}, \widehat{\mathbf{H'}}]$.

Eqn. (2.20) implies that $\mathcal{TR}[\widehat{\mathbf{H}}, \widehat{\mathbf{H'}}] \in [0, 1]$. More specifically, a larger TRRS indicates a higher similarity between two fingerprints and thus the two associated locations.

Notice that, we use $\mathcal{TR}[\widehat{\mathbf{H}}, \widehat{\mathbf{H'}}]$ for indoor localization and $\mathcal{TR}_{\phi^\star}[\widehat{\mathbf{H}}, \widehat{\mathbf{H'}}]$ for vital sign monitoring, mainly because that the phase information is more important in the latter case.

Due to the bandwidth limit on mainstream WiFi systems, the TRRS calculated in SISO-OFDM systems is in general insufficient to characterize the differences between two locations centimeters away from each other. To clearly illustrate the
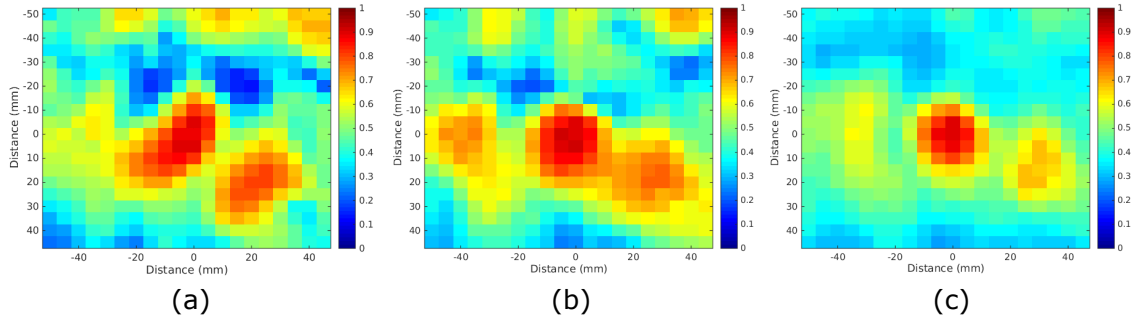
Figure 2.9: Ambiguity among nearby locations under (a) 40 MHz bandwidth (b) 120 MHz bandwidth (c) 360 MHz bandwidth.

impact of bandwidth on localization performance, we have conducted experiments to collect CSIs under different bandwidths in a typical indoor environment. Two channel sounders are placed in an NLOS setting, where one of them is placed on a customized experiment structure with 5 mm resolution.

The corresponding TRRS between the target location and nearby locations are illustrated in Fig. 2.9 under different bandwidth settings. It is shown in Fig. 2.9(a) that with 40 MHz bandwidth, a large region of nearby locations is ambiguous with the target location in terms of the TRRS. Enlarging the bandwidth shrinks the area of ambiguous regions. As demonstrated in Fig. 2.9(c), when the bandwidth increases to 360 MHz, the ambiguous region is reduced to a ball of 1 cm radius which implies centimeter accuracy in localization.

The experiment results motivate us to formulate a large effective bandwidth by exploiting diversities on WiFi devices to facilitate centimeter accuracy indoor localization as shown in Section 2.2.3.

2.2.3 Calculating Time-Reversal Resonating Strength with Frequency and Spatial Diversity

Based on extensive experimental results, The TRRS calculation in 2.2.2 for SISO-OFDM systems is not sufficient to characterize differences of location fingerprints associated with locations centimeter away. As mentioned in Chapter 1, this is mainly because that the 20/40 MHz bandwidth only provides a very vague multipath profile and leads to ambiguity among locations. To enhance the quality of TRRS calculation, we exploit diversities inherent in modern WiFi systems empowered by MIMO-OFDM techniques, namely, the frequency diversity and the spatial diversity.

According to IEEE 802.11n, 35 WiFi channels are dedicated to WiFi transmission in 2.4GHz and 5GHz frequency bands with a maximum bandwidth of 40 MHz. The multitude of WiFi channels leads to frequency diversity in that, they provide opportunities for WiFi devices to perform frequency hopping when experiencing deep fading or severe interference. On the other hand, spatial diversity can be exploited on MIMO-OFDM WiFi devices, a mature technique that significantly boosts the spectral efficiency. MIMO has not only become an essential component of IEEE 802.11n/ac but also been ubiquitously deployed on numerous commercial WiFi devices. Both diversities can be harvested to provide fingerprints with much finer granularity and lead to less ambiguity in comparison with the fingerprint measured with a bandwidth of only 40 MHz.

The calculation of TRRS is modified for MIMO-OFDM systems with frequency

diversity such that CFRs on different antennas as well as channels contribute to the overall TRRS weighted by their channel powers. In particular, η, Λ, and Λ' are modified as

$$\eta = \sum_{n_{tx}=1}^{N_{tx}} \sum_{n_{rx}=1}^{N_{rx}} \sum_{f=1}^{F} \eta_{n_{tx},n_{rx},f}, \ \Lambda = \sum_{n_{tx}=1}^{N_{tx}} \sum_{n_{rx}=1}^{N_{rx}} \sum_{f=1}^{F} \Lambda_{n_{tx},n_{rx},f}, \ \Lambda' = \sum_{n_{tx}=1}^{N_{tx}} \sum_{n_{rx}=1}^{N_{rx}} \sum_{f=1}^{F} \Lambda'_{n_{tx},n_{rx},f} \ ,$$

(2.26)

where N_{tx}, N_{rx}, F are the number of transmitting antennas, receiving antennas, and WiFi channels respectively, and

$$\eta_{n_{tx},n_{rx},f} = \sum_{k=1}^{K} \widehat{H_{u_k}^{n_{tx},n_{rx},f}} \widehat{H_{u_k}^{'*n_{tx},n_{rx},f}} e^{-ju_k\phi^{\star}_{n_{tx},n_{rx},f}}$$

(2.27)

where

$$\phi^{\star}_{n_{tx},n_{rx},f} = \operatorname*{argmax}_{\phi} \left| \sum_{k=1}^{K} \widehat{H_{u_k}^{n_{tx},n_{rx},f}} \widehat{H_{u_k}^{'*n_{tx},n_{rx},f}} e^{-ju_k\phi} \right|$$

(2.28)

represents the modified cross-correlation on the resource block (n_{tx}, n_{rx}, f). $\Lambda_{n_{tx},n_{rx},f}$ and $\Lambda'_{n_{tx},n_{rx},f}$ are given by

$$\Lambda_{n_{tx},n_{rx},f} = \sum_{k=1}^{K} |\widehat{H_{u_k}^{n_{tx},n_{rx},f}}|^2$$

(2.29)

$$\Lambda'_{n_{tx},n_{rx},f} = \sum_{k=1}^{K} |\widehat{H_{u_k}^{'n_{tx},n_{rx},f}}|^2 \ .$$

(2.30)

Finally, TRRS is calculated as

$$\mathcal{TR}[\widehat{\mathbb{H}}, \widehat{\mathbb{H'}}] = \left| \mathcal{TR}_{\phi^{\star}}[\widehat{\mathbb{H}}, \widehat{\mathbb{H'}}] \right|^2,$$

(2.31)

$$\mathcal{TR}_{\phi^{\star}}[\widehat{\mathbb{H}}, \widehat{\mathbb{H'}}] = \frac{\eta}{\sqrt{\Lambda}\sqrt{\Lambda'}} \ ,$$

(2.32)

where $\widehat{\mathbb{H}}$ stands for the fused CFRs from multiple links given as

$$\widehat{\mathbb{H}} = \underbrace{\left[\widehat{H_{u_1}^{1,1,1}} \ \ \widehat{H_{u_2}^{1,1,1}} \ \ \cdots \ \ \widehat{H_{u_K}^{1,1,1}} \ \ \cdots \ \ \widehat{H_{u_K}^{N_{tx},N_{rx},F}} \right]}_{N_{tx} \times N_{rx} \times F \times K}$$

(2.33)

Fig. 2.10 visualizes an example of harvesting frequency and spatial diversity independently/jointly on WiFi devices.

$\mathbf{H}_{s_1,f_1}$	$\mathbf{H}_{s_1,f_2}$	$\mathbf{H}_{s_1,f_3}$	$\mathbf{H}_{s_1,f_4}$

(a) Frequency Diversity

$\mathbf{H}_{s_1,f_1}$	$\mathbf{H}_{s_2,f_1}$	$\mathbf{H}_{s_3,f_1}$	$\mathbf{H}_{s_4,f_1}$

(b) Spatial Diversity

$\mathbf{H}_{s_1,f_1}$	$\mathbf{H}_{s_2,f_1}$	$\mathbf{H}_{s_1,f_2}$	$\mathbf{H}_{s_2,f_2}$

(c) Frequency − Spatial Diversity
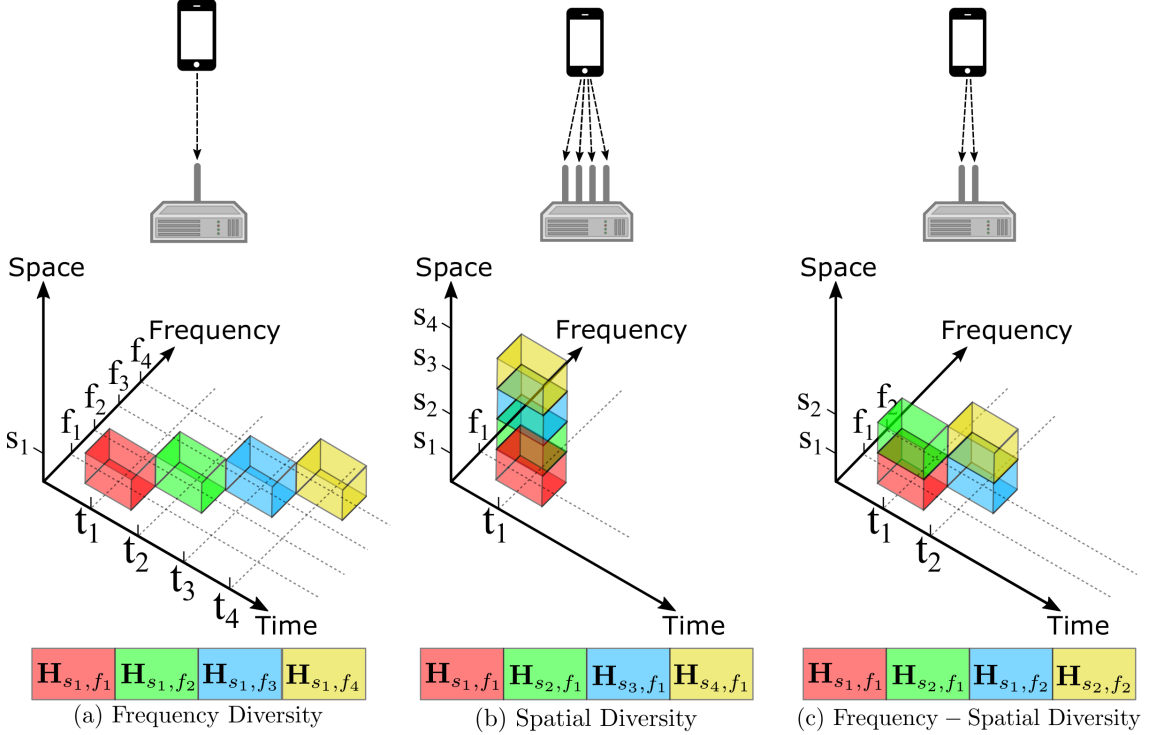
Figure 2.10: Leveraging frequency and spatial diversities in WiFi to achieve large effective bandwidth.

2.2.4 Effective Bandwidth

Since we fully utilize the information contained in multi-antenna WiFi systems in TRRS calculation, we achieve an effective bandwidth W_e of

$$W_e = \frac{K N_{tx} N_{rx} F B}{N} \;, \tag{2.34}$$

where B is the bandwidth per link. In 802.11n WiFi systems, B can be as large as 40 MHz. K/N illustrates the ratio of available subcarriers over the total number of

subcarriers.

The effective bandwidth acts as a metric that quantifies the available resources in a fingerprint-based IPS that can be harnessed for localization. A large effective bandwidth generally leads to an improved localization performance in terms of the detection rates and the false alarm rates.

2.3   Summary

In this chapter, we have introduced the CFR models for indoor localization and vital sign monitoring. We also show the concept of TR techniques and present the calculation of TRRS in SISO-OFDM and MIMO-OFDM systems with frequency diversity. The concept of effective bandwidth is also presented.

Chapter 3

Time-Reversal Indoor Positioning with Frequency Diversity

From the previous discussion, it is clear that indoor localization is crucial in IoT applications. Sampling the rich literature, we find that the indoor positioning systems (IPSs) can be classified into two classes: ranging-based and fingerprint-based [66]. Details of both classes are elaborated below.

- For the ranging-based methods, at least three anchors are deployed into the indoor environment to triangulate the device through measuring the relative distances between the device to the anchors. The distances are generally obtained from other measurements, e.g., RSSI, ToA, ToF, and AoA. RSSI-based ranging methods [37, 44, 70] utilizes the path-loss model to derive the distance and can typically achieve an accuracy of $1 \sim 3$m on average under LOS scenarios, while ToA-based ranging methods retrieve the ToA of the first arrived multipath component from the CIR. To achieve a fine timing resolution, ToA-based methods require a large bandwidth, which is achievable with ultra-wideband (UWB) techniques that lead to an accuracy of $10 \sim 15$cm in a LOS setting [5,18]. In [58], Vasisht *et al.* present a decimeter-level localization using a single WiFi access point. They utilize frequency hopping to acquire CFRs. Leveraging the non-uniform discrete Fourier Transform (NDFT), they

31

recover the time-domain CIR and use the time delay of the dominant peak in the recovered CIR as the ToF measurement. However, in a strong NLOS environment, the dominant peak of CIR does not necessarily characterize the direct path between the WiFi devices which leads to an increased localization error. The AoA-based schemes proposed in [33] and [63] have the same issue that degrades localization accuracy in a complicated NLOS indoor environment.

- The fingerprint-based approaches harness the naturally existing spatial features associated with different locations, e.g., RSSI, CIR, and CFR. In these schemes, fingerprints of different locations are stored in a database during the offline phase. In the online phase, the fingerprint of the current location is compared against those in the database to estimate the device location. In [14, 48, 67], RSSI values from multiple access points (APs) are utilized as the fingerprint, leading to an accuracy of $2 \sim 5$m. In [60], Wu *et al.* utilize multi-dimensional scaling to construct a stress-free floorplan as well as its associated fingerprint space containing the RSSI values obtained from locations on the stress-free floorplan for crowdsourcing-based indoor localization. The average error is around 2m with the maximum error of 8m. The accuracy can be further improved to $0.95 \sim 1.1$m by taking CFRs as the fingerprint [19,52,62]. In [61], Wu *et al.* obtain CIR fingerprints under a bandwidth of 125 MHz and calculate TRRS as the similarity measure among different locations, leading to an accuracy of $1 \sim 2$cm under NLOS scenarios.

Summarizing the ranging-based and fingerprint-based schemes, we find that

1. *The accuracy of the ranging-based methods are susceptible to the correctness of the physical rules, e.g., path-loss model, which degrades severely in the complex indoor environment.* The existence of a large number of multipath components and blockage of obstacles in indoor spaces impair the precision of the physical rules.

2. *The fingerprint-based methods, which can work under strong NLOS environment, require a large bandwidth for accurate localization.* Since the maximum bandwidth of the mainstream 802.11n is 40 MHz, IPSs utilizing WiFi techniques cannot resolve enough independent multipath components in the environment which introduces ambiguities into fingerprints associated with different locations. Thus, the localization performance is degraded. On the other hand, a bandwidth as large as 125 MHz that leads to centimeter accuracy [61] can only be achieved on dedicated hardware and incurs additional costs in deployment.

In this chapter, we propose an IPS that achieves centimeter accuracy using only one pair of single-antenna WiFi devices.By frequency hopping, the presented scheme collects CFRs from a large multitude of channels and concatenate the CFRs into a location fingerprint with a very large effective bandwidth. The scheme can work very well under strong NLOS conditions in a complicated indoor environment. It is also robust against RF interference. Moreover, it is an infrastructure-free scheme built upon WiFi infrastructures readily available indoor. The performance of the

proposed IPS is verified by extensive experiments in a typical office environment to demonstrate the centimeter accuracy within an area of 20cm×70cm under strong NLOS conditions.

The rest of this chapter is organized as follows. In Section 3.1, we elaborate on the proposed localization algorithm. In Section 3.2, we present the frequency hopping mechanism. In Section 3.3, we demonstrate the experiment results in a typical office environment. In Section 3.4, we present some discussions on several aspects of the proposed IPS. Finally, we draw conclusions in Section 3.5.

3.1 Proposed Algorithm

3.1.1 Indoor Localization Based on TRRS

The proposed localization algorithm consists of an offline phase and an online phase. The details of the two phases are elaborated below.

3.1.1.1 Offline Phase

In the offline phase, the CFRs are measured from a total of F different channels, denoted by $1, 2, \cdots, f, \cdots, F$, and from L locations-of-interest, denoted by $1, 2, \cdots, \ell, \cdots, L$. The CFR matrix $\widehat{\mathbb{H}}$ is given as (2.31).

3.1.1.2 Online Phase

The CFRs from an unknown location are formulated into the location fingerprint in the same manner as described in the offline phase. Assume that the location

fingerprint from the unknown location ℓ' is given by $\widehat{\mathbb{H}_\ell}$, the TRRS between location ℓ' and location ℓ is computed as $\mathcal{TR}\left[\widehat{\mathbb{H}_\ell}, \widehat{\mathbb{H}_{\ell'}}\right]$ based on (2.31) with $N_{tx} = 1$ and $N_{rx} = 1$. Define $\ell^\star = \underset{\ell=1,2,\cdots,L}{\operatorname{argmax}} \mathcal{TR}\left[\widehat{\mathbb{H}_\ell}, \widehat{\mathbb{H}_{\ell'}}\right]$, the estimated location $\hat{\ell'}$ takes the form

$$\hat{\ell'} = \begin{cases} \ell^\star, & \text{if } \mathcal{TR}\left[\widehat{\mathbb{H}_{\ell^\star}}, \widehat{\mathbb{H}_{\ell'}}\right] \geq \Gamma \\ \\ 0, & \text{Otherwise} , \end{cases} \tag{3.1}$$

where Γ is a tunable threshold. In case of $\mathcal{TR}\left[\widehat{\mathbb{H}_{\ell^\star}}, \widehat{\mathbb{H}_{\ell'}}\right] < \Gamma$, the proposed IPS fails to localize the device, and the algorithm returns 0 to imply an *unknown location.*

In Fig. 3.1, we show an example of location fingerprints generated at two different locations in different colors. For each location, we formulate 5 location fingerprints. As we can see, the differences among the location fingerprints at the same location are minor, while the differences of location fingerprints between the two different locations are much more pronounced.
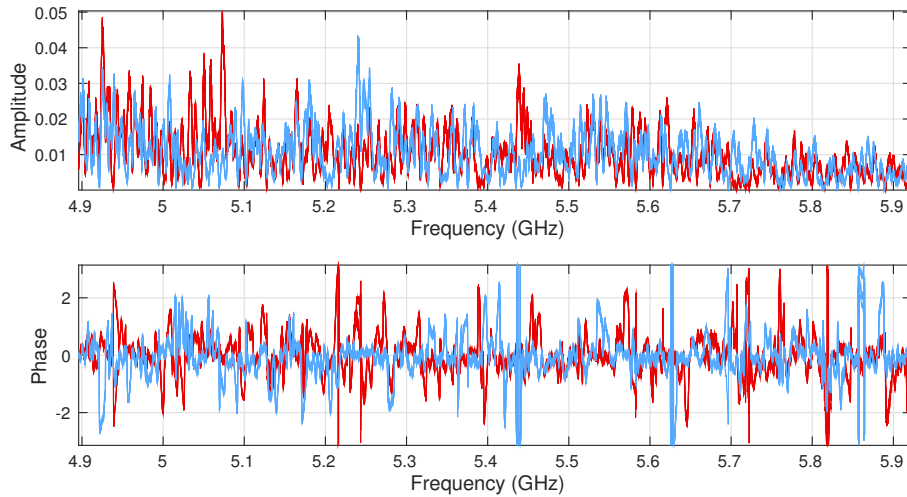
Figure 3.1: A snapshot of location fingerprints after bandwidth concatenation at two different locations.

3.2 Frequency Hopping Mechanism

In this section, we elaborate on the implementation details of the proposed IPS.

3.2.1 CFR Acquisition using USRPs

We build two Universal Software Radio Peripherals (USRP) N210 [2] into prototypes for localization. Each USRP is equipped with one omni-directional antenna.

In [15], Bastian *et al.* develop a WiFi transceiver supporting WiFi standards 802.11a/g/p under the framework of GNU Radio [4]. The proposed WiFi transceiver in [15] extracts the CFRs by the 4 frequency-domain subcarrier pilots followed by an interpolation to fully recover the CFRs on the 48 usable data subcarriers. However, due to the scarcity of the subcarrier pilots, the estimated CFRs are not accurate enough to provide fine details about the environment to facilitate indoor localization.

To acquire CFRs with high quality, we extend the framework in [15] by including a channel estimator leveraging the two LTPs as shown in the WiFi frame structure in Fig. 2.3. Each LTP is composed by 56 data subcarriers which are known in advance at the receiver side. The CFRs are extracted based on the LTPs which are further used to equalize the signal field frame that contains the information of the coding rate as well as the signal constellation of the transmitted OFDM symbols. Then, the receiver decodes the data payloads based on this information.

We also notice that the framework in [15] lacks the mechanism of carrier sense multiple access (CSMA) and interference from other WiFi devices is unavoidable.

In light of this issue, we only keep those CFRs associated with data payloads successfully decoded.

3.2.2 Implementing the Frequency Hopping Mechanism

In the proposed IPS, frequency hopping is used to acquire CFRs from a multitude of frequency bands. In Fig. 3.2, we demonstrate the timing diagram of the mechanism of synchronous frequency hopping with feedback between two devices from the center frequency f_0 to f_1. Here, ACK stands for the acknowledgement frame, and REQ denotes the frequency hopping request frame. Device 2 initializes the procedure by tuning its center frequency at f_0. Then, device 1 starts transmission at f_0 as well to facilitate CFR acquisition on device 2. Assume that the minimum number of CFRs per frequency band is $M_{\min}$. After obtaining $M_{\min}$ CFRs at f_0, device 2 sends an ACK frame to device 1, and device 1 feedbacks a REQ frame to device 2. On reception of the REQ frame, device 2 adjusts its center frequency to f_1, and device 1 begins transmission at f_1.

In Fig. 3.2, we assume that the two devices perform full-duplex communication, i.e., transmitting signals while listening simultaneously to acquire the ACK and REQ frames. However, in practice, the USRP N210 devices in the proposed IPS are half-duplex, i.e., one device cannot perform WiFi transmitting and receiving at the same time. Thus, each device needs to switch between the transmitting mode and the receiving mode in different time slots. Fig. 3.3 shows an example of frequency hopping from f_0 to f_1. The details for each time-of-interest denoted as $t_1, t_2, \cdots, t_{12}$
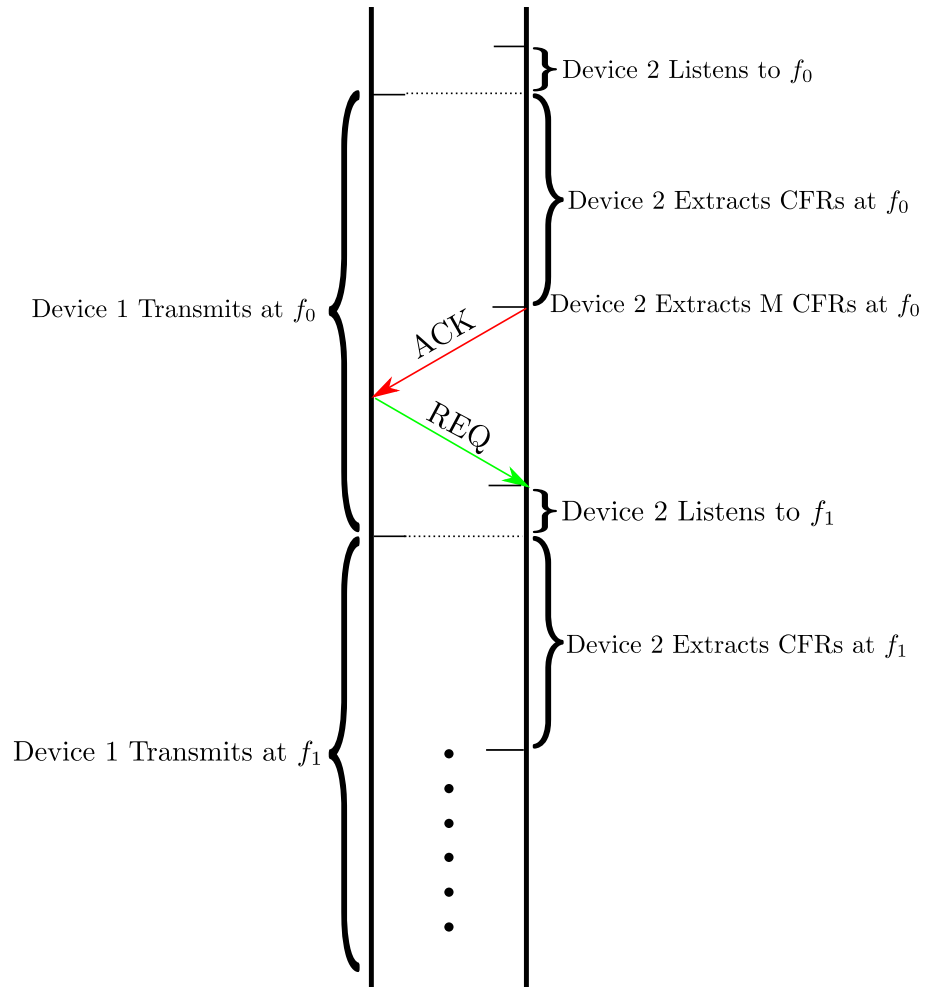
Figure 3.2: Timing diagram of the frequency hopping mechanism.

in Fig. 3.3 are presented below.

t_0: Device 2 (D2) tunes its center frequency to f_0 and stays in the receiving mode.

t_1: Device 1 (D1) tunes its center frequency to f_0 and begins data transmission. D2 detects the presence of data transmission and performs channel estimation to extract CFRs from each data frame. Device D2 stays in the receiving mode until the number of CFRs exceeds $M_{\min}$.

t_2: D1 switches to receiving mode to determine whether D2 sends an acknowledgement signal (ACK) by encoding the message in the data payloads. Suppose that at this moment, D2 obtains $M' < M_{\min}$ CFRs. Since the number of CFRs is insufficient, D2 still stays in the receiver mode. Notice that, if D2 acquires sufficient CFRs in this stage, D2 would switch to the transmitter mode and send an ACK frame to D1, and the procedure would continue from t_7.

t_3: D1 does not receive the ACK frame from D2 and thus switches back to the transmitter mode and continues data transmission.

t_4: D2 receives the targeted $M_{\min}$ CFRs and switches to the transmitter mode. It then transmits an ACK signal to D1. Nevertheless, since D1 is in transmitter mode, the ACK signal transmission fails.

t_5: D2 switches to receiver mode to decide whether D1 sends a frequency hopping request (REQ) which is encoded into the data payloads. Due to the failure of the ACK signal transmission at t_4, D1 is unable to send the REQ signal.

t_6: D1 switches to the receiver mode again.
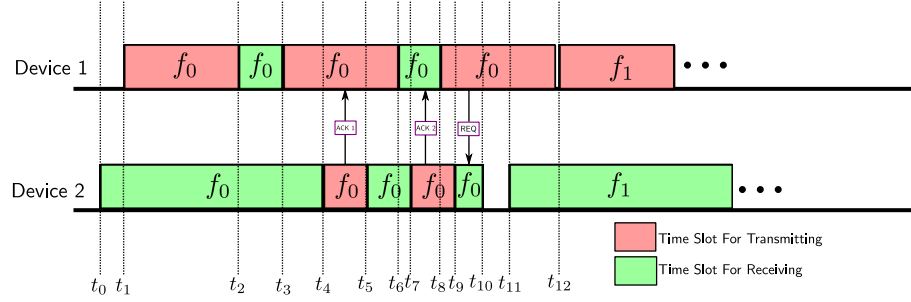
Figure 3.3: The timing diagram for frequency hopping.

t_7: D2 switches to the transmitter mode again and sends out another ACK signal.

t_8: D1 receives the ACK signal and switches to the transmitter mode to send out an REQ. However, Device 2 is still in the transmitter mode and cannot receive the request at this moment.

t_9: D2 switches to the receiver mode and receives the REQ signal because that D1 stays in the transmitter mode.

t_{10}: D2 begins the process of tuning its center frequency to f_1.

t_{11}: D2 successfully tunes its center frequency to f_1 and awaits the transmission from D1 at f_1 as well. Since D1 is still transmitting using f_0, D2 is unable to decode the signal.

t_{12}: D1 also tunes its center frequency to f_1 and begins transmission.

The same protocol is repeated until CFRs from all desirable frequency bands are measured.

3.3 Experimental Results

3.3.1 Experimental Settings
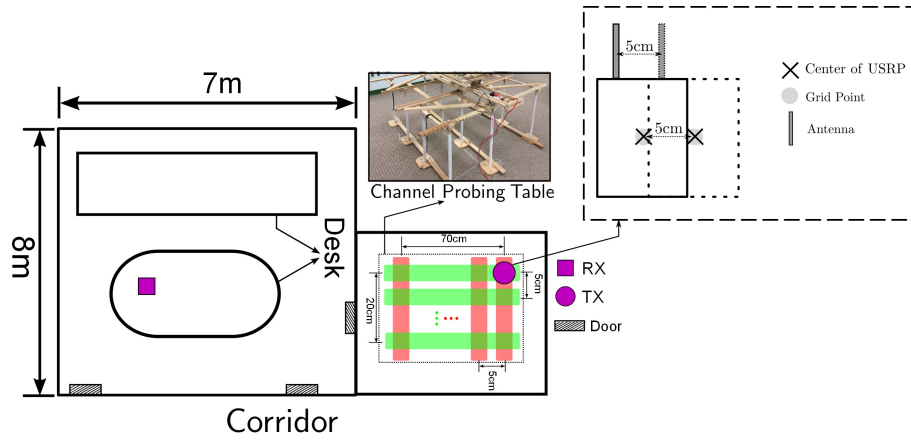
Figure 3.4: Experimental settings.

Fig. 3.4 shows the setups of the experiments with details given below.

3.3.1.1 Environment

The experiments are conducted in a typical office suite composed by a large and a small office room in a multi-story building. The two office rooms are blocked by a wall. In addition to the two large desks, the indoor space is filled with other
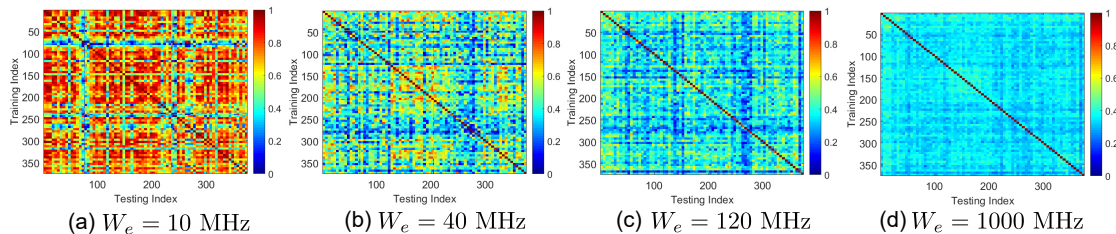
Figure 3.5: TRRS matrix under different W_e.
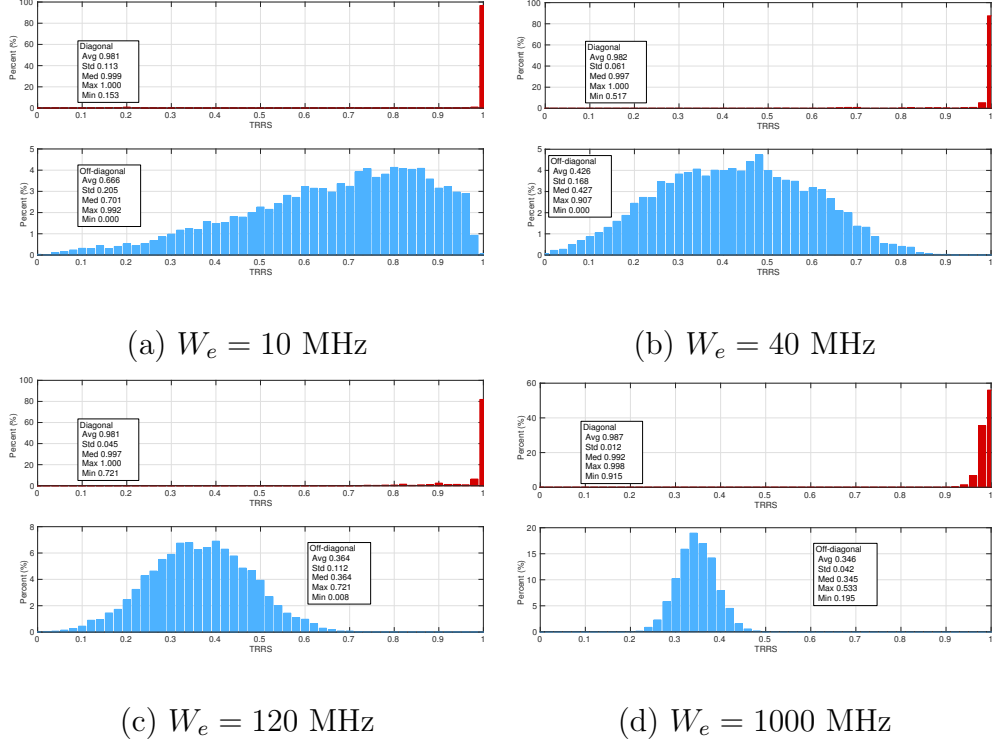
Figure 3.6: Histogram of diagonal and off-diagonal entries under different W_e.

furniture including chairs and computers, which are not shown in Fig. 3.4 for brevity.

3.3.1.2   Configurations

Two USRPs are used to obtain the CFRs with bandwidth configured as $W = 10$ MHz. The two USRPs coordinate with each other to perform synchronous frequency hopping using the mechanism discussed in Section 3.2. The step size of frequency hopping is fixed at $\Delta f = 8.28$ MHz*. The minimum number of CFRs per channel is set as $M_{\min} = 10$.

*Considering the null subcarriers at both edges of the WiFi channel spectrum, we adjust the frequency hopping step size such that the entire spectrum can be covered without spectrum holes. Notice that the proposed IPS does not require the measured frequency band to be contiguous.
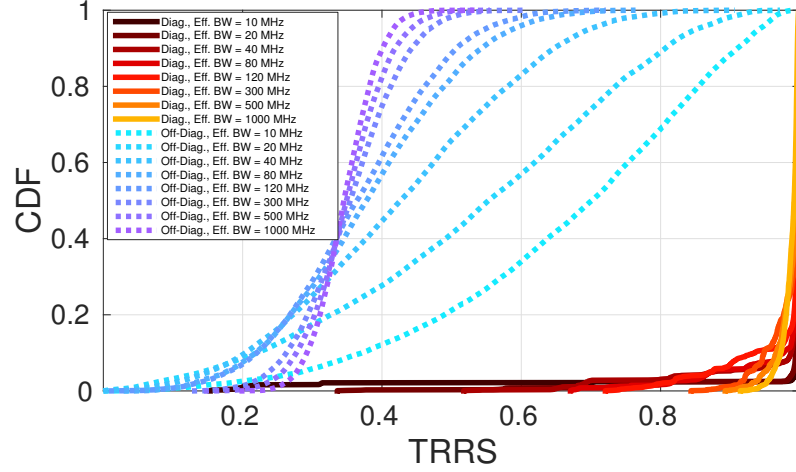
Figure 3.7: Cumulative density functions of diagonal and off-diagonal entries of the TRRS matrix under different W_e.
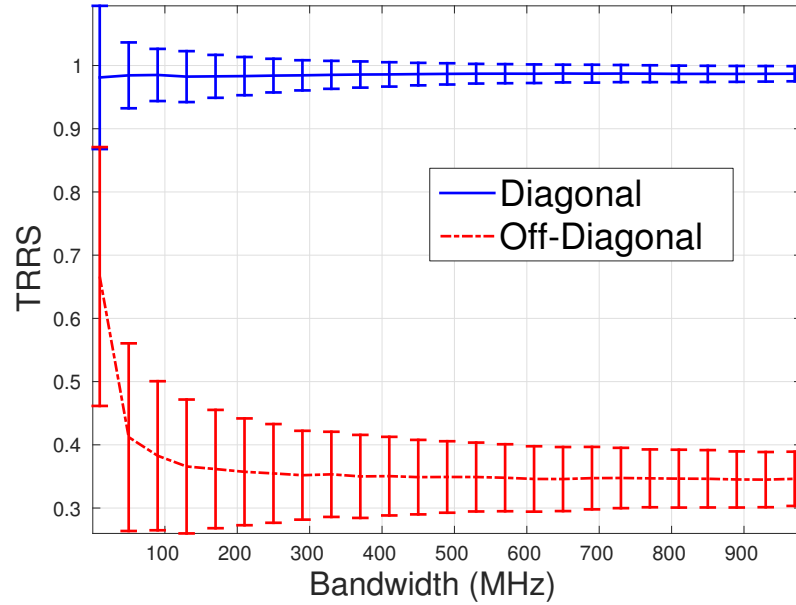
Figure 3.8: Mean and standard deviation of the diagonal and off-diagonal entries of the TRRS matrix under different W_e.
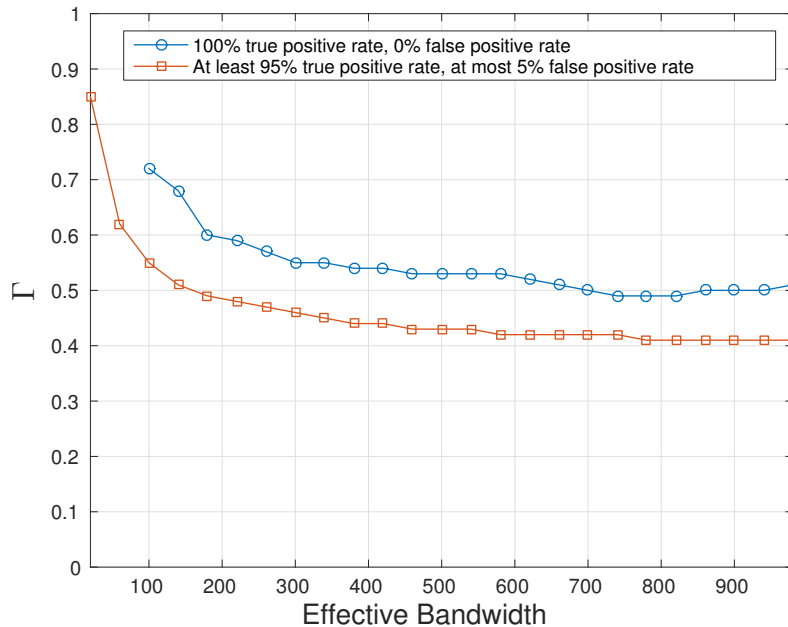
Figure 3.9: Threshold Γ under different W_e to achieve (i) $P_{\mathsf{TP}} = 100\%$ and $P_{\mathsf{FP}} = 0\%$ (ii) $P_{\mathsf{TP}} \geq 95\%$ and $P_{\mathsf{FP}} \leq 5\%$.

3.3.1.3 Details of Measurement

One USRP is placed on the grid points on a measurement platform in the small room as shown in Fig. 3.4. The center of the USRP is aligned with the grid point. The distance between two adjacent grid points is 5cm. The other USRP is placed on the table of the larger room. CFRs from $L = 75$ different grid points are measured within an area of 70cm×20cm. For each measurement, the two USRPs sweep the frequency band from 4.9 to 5.9 GHz, leading to a total of $F = 124$ measured WiFi channels with a step size of 8.28 MHz. The effective bandwidth W_e is thus 1 GHz. For each of the 75 locations, we formulate $M = 10$ location fingerprints.

3.3.2 Metrics for Performance Evaluation

For the $M = 10$ fingerprints collected at each location, we store the first $M_1 = 5$ CFRs into the fingerprint database in the offline phase, and consider the other $M_2 = 5$ fingerprints as samples collected in the online phase. Denote the m-th location fingerprint formulated at location ℓ as $\widehat{\mathbb{H}_\ell}$, we calculate the TRRS matrix $\mathbb{R}$ with the (i,j)-th entry of $\mathbb{R}$ given by $\mathcal{TR}[\widehat{\mathbb{H}_\ell}, \widehat{\mathbb{H}_{\ell'}}]$, where $m = \mathsf{Mod}(i, M_1) + 1$, $\ell = \frac{i-m-1}{M_1} + 1$, $n = \mathsf{Mod}(j, M_2) + 1$, and $\ell' = \frac{j-n-1}{M_2} + 1$. Here, Mod is the modulus operator, i is termed as the training index, and j is termed as the testing index.

We define the entries of $\mathbb{R}$ calculated from CFRs obtained at the same locations as the *diagonal entries*, while those calculated using CFRs obtained from different locations as the *off-diagonal entries*. We demonstrate the histograms and cumulative density functions for the diagonal and off-diagonal entries.

Based on $\mathbb{R}$, we evaluate the localization performances using the metrics of the true positive rate, denoted as P_{TP}, and the false positive rate, denoted as P_{FP}. P_{TP} is defined as the probability that the IPS localizes the device to its correct location, while P_{FP} captures the probability that the IPS localizes the device to a wrong location, or fails to localize the device.

In the performance evaluation, the CFR sifting parameter τ is set as 0.8.

3.3.3 Performance Evaluation

3.3.3.1 TRRS Matrix under Different W_e

Fig. 3.5 demonstrates $\mathbb{R}$ with $W_e \in [10, 40, 120, 1000]$ MHz. We observe that when $W_e = 10$ MHz, there exists many large off-diagonal entries in $\mathbb{R}$, indicating severe ambiguities among different locations. When the total bandwidth W_e increases, the ambiguities among different locations are significantly eliminated, while the TRRS within the same location are almost unchanged.

3.3.3.2 Distribution of Diagonal and Off-diagonal Entries under Different W_e

Fig. 3.6 visualizes the distribution of the diagonal and off-diagonal entries of $\mathbb{R}$ with different $W_e \in [10, 40, 120, 1000]$ MHz using histograms. Statistics of the diagonal and off-diagonal entries are shown as well. As we can see, the TRRS values at the same locations are identical with different W_e, implying high stationarity of the proposed IPS. On the other hand, the off-diagonal entries are more suppressed and approach a Gaussian-like distribution when W_e increases. We also observe an enlarged gap between the diagonal and off-diagonal entries when W_e increases, indicating a better separability among different locations. The increase of W_e also reduces the variations of diagonal and off-diagonal entries, as shown by the decreasing standard deviations. Moreover, a large W_e removes the outliers in the diagonal entries: when $W_e = 10$ MHz, the minimum value of diagonal entries is 0.153, while

the minimum value increases to 0.915 when $W_e = 1000$ MHz. Thus, a large W_e improves the robustness of the IPS against outliers.

3.3.3.3 Cumulative Density Functions of Diagonal and Off-diagonal Entries under Different W_e

In Fig. 3.7, we demonstrate the cumulative density functions of diagonal and off-diagonal entries with $W_e \in [10, 20, 40, 80, 120, 300, 500, 1000]$ MHz. As can be seen from the figure, a large W_e reduces the spread of both the diagonal and off-diagonal entries, which agrees with the results shown in Fig. 3.6.

3.3.3.4 Mean and Standard Deviation Performances under Different W_e

Fig. 3.8 depicts the impact of W_e on the mean and standard deviation performances for both diagonal and off-diagonal entries. The upper and lower bars indicate the $\pm\sigma$ bounds with respect to the average, where σ stands for the standard deviation. We conclude that: a large W_e improves the distinction among different locations, but also reduces the variation of the TRRS at the same locations as well as among different locations. In other words, a large W_e makes the IPS performance more stable and predictable.

3.3.3.5 Threshold Γ Settings under Different W_e

Fig. 3.9 depicts the smallest threshold Γ under $W_e = [20, 60, 100, \cdots, 1000]$ MHz to achieve (i) $P_{\mathsf{TP}} = 100\%$ and $P_{\mathsf{FP}} = 0\%$ (ii) $P_{\mathsf{TP}} \geq 95\%$ and $P_{\mathsf{FP}} \leq 5\%$. We observe a decreasing in Γ when W_e is larger, which can be justified by the fact that the gap between the diagonal and off-diagonal entries enlarges when W_e becomes larger. When $W_e = 20$ MHz, the IPS fails to achieve $P_{\mathsf{TP}} = 100\%$ and $P_{\mathsf{FP}} = 0\%$. Fig. 3.9 also implies that we can achieve a perfect 5cm localization if Γ is chosen appropriately.

Based on the experimental results, we conclude that a large W_e is imperative for the robustness, stability, and performance of the proposed IPS. By formulating the location fingerprint that concatenates multiple channels, the proposed IPS achieves a perfect centimeter localization accuracy in an NLOS environment with one pair of single-antenna WiFi devices.

3.4 Discussion

3.4.1 Achievable Localization Accuracy

In Section 3.3, we demonstrate the centimeter-level localization accuracy of the proposed IPS with a fine-grained measurement of 5cm resolution. In a recent experiment, we refine the measurement resolution to 0.5cm to study the accuracy. The TRRS near the intended location is shown in Fig. 3.10 with $W_e = 125$ MHz, which demonstrate that the localization accuracy can reach $1 \sim 2$cm in an NLOS
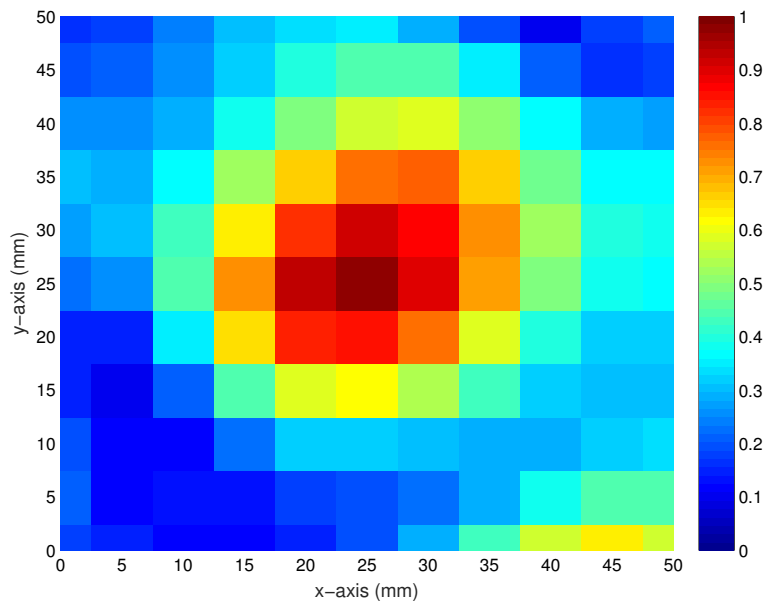
Figure 3.10: TRRS near the intended location with a measurement resolution of 0.5cm.

environment.

3.4.2   Complexity of Fingerprint Collecting

In this work, the CFRs are collected in a two-dimensional (2D) space. In practice, localization of an object requires CFR measurement from a three-dimensional (3D) space with a centimeter-level granularity. In this case, the complexity of CFR measurement can be too high to be practical, especially for a large indoor space.

The burden of measurement can be significantly reduced since we only need to obtain the fingerprints of a limited number of areas which are more critical than the others. For instance, in an office, the main entrance and exit of the office as well as the entrance to some office rooms are of higher importance than the other

49

areas, while in a museum, areas closer to the paintings could be more important. Fine-grained CFR measurements can be confined to these areas-of-interest. On the other hand, the efficiency of measurement can be boosted by automation techniques such as robotics.

3.4.3 Scalability

We notice that most of the calculations in the offline phase and online phase can be interpreted as linear operations. Thus, the computational complexity of the proposed IPS scales linearly with the number of location fingerprints stored in the database. As the offline phase can in general tolerate a large delay, the increase in the computational complexity of the offline phase is less significant. On the other hand, the increase of the complexity imposes a challenge to the online phase since the online phase is much more time-sensitive than the offline phase. This issue becomes more severe when a huge number of fingerprints are stored in the database.

To deal with this problem, other information such as the sensory information or the RSSI values can be retrieved to supplement the proposed IPS with a coarse position estimation. Then, the proposed IPS can choose a subset of the fingerprints from the database that are collected nearby the estimated location to formulate a refined estimation.

3.5 Summary

In this chapter, we have proposed a WiFi-based IPS that exploits the frequency diversity to achieve centimeter accuracy for indoor localization. The IPS fully harnesses the frequency diversity by CFR measurements on multiple channels via frequency hopping. Impacts of synchronization errors and interference are mitigated by CFR sanitization, sifting, and averaging. The averaged CFRs of different channels are then concatenated together into location fingerprints to augment the effective bandwidth. The location fingerprints are stored into a database in the offline phase and are used to calculate the TRRS in the online phase. Finally, the proposed IPS determines the location based on the TRRS. Extensive experiment results of measurements on a 1 GHz frequency band demonstrate the centimeter localization accuracy of the proposed IPS in a typical office environment with a large effective bandwidth.

Chapter 4

Time-Reversal Indoor Positioning with Spatial Diversity

As discussed in Chapter 3, a large effective bandwidth can be achieved on WiFi devices via frequency hopping to facilitate centimeter accuracy localization. A drawback with this approach lies in that frequency hopping is time-consuming and not power efficient. Moreover, as the proposed system co-exists with other WLAN networks, the dynamics of the WiFi traffic from the other WLAN networks could inject random interferences into the CFRs that undermines the indoor localization performance, especially in areas with a dense deployment of WiFi APs.

Realizing these potential issues of indoor localization using frequency diversity, in this chapter, we turn to the spatial diversity available in MIMO-OFDM systems. We demonstrate that a large effective bandwidth can also be formulated MIMO-OFDM devices via the exploitation of spatial diversity. Compared with the frequency-hopping approach, the multi-antenna-based approach chapter is more efficient both in time and power.

The proposed multi-antenna-based scheme optimally concatenates available bandwidths on antenna links to formulate a much larger effective bandwidth. Similar to the scheme shown in Chapter 3, the proposed scheme consists of an offline phase and an online phase. In the offline phase, the proposed IPS combines CFRs

from multiple locations-of-interest on several antenna links which are combined into location fingerprints, while in the online phase, the IPS obtains instantaneous CFRs from multiple antennas and calculates TRRS between the instantaneous CFRs and those in the online phase. The residual synchronization errors are mitigated in the computations of TRRS. Finally, the IPS determines the locations based on the TRRS.

We conduct extensive experiments in an office environment using a single pair of off-the-shelf WiFi devices to illustrate that the proposed IPS can achieve detection rates of 99.91% and 100%, while triggering negligible false alarm rates of 1.81% and 1.65% under line-of-sight (LOS) and non-line-of-sight (NLOS) scenarios respectively for locations with a unit distance of $5cm$. We also show that the proposed IPS is robust against environment dynamics. Moreover, experiment results with a unit distance of $0.5cm$ demonstrate that $1 \sim 2cm$ accuracy is achievable with the proposed IPS. To the best of our knowledge, this is the first work that achieves $1 \sim 2cm$ localization accuracy under NLOS scenarios using a single pair of off-the-shelf WiFi devices leveraging spatial diversity.

The rest of this chapter is organized as follows. In Section 4.1, we elaborate on the localization algorithm for the IPS. In Section 4.2, we demonstrate the experiment results. Finally, conclusions are drawn in Section 4.3.

4.1 Localization Algorithm

In this section, we introduce the indoor localization algorithm with multi-antenna WiFi devices.

4.1.1 Offline Phase

During the online phase, we collect R CFRs from each of the L locations-of-interest. The $L \times R$ CFRs are stored into the CFR database denoted as $\mathbf{D}_{\text{train}}$. The i-th column of $\mathbf{D}_{\text{train}}$ is given by $\widehat{\mathbb{H}}_i$ with $\widehat{\mathbb{H}}_i$, and i is the *training index*. Denote the realization index as r and the location index as ℓ, the training index i can be mapped from (r, ℓ) as $i = (\ell - 1)R + r$.

4.1.2 Online Phase

The problem of determining the device location can be cast into an multi-hypothesis testing problem. More specifically, assume that we collect an instantaneous CFR $\widehat{\mathbb{H}}'$ from a location ℓ' to be estimated. Then, we calculate the combined TRRS between each CFR in $\mathbf{D}_{\text{train}}$ and $\widehat{\mathbb{H}}'$ shown as (2.31), which leads to $\{\mathcal{TR}[\widehat{\mathbb{H}}_i, \widehat{\mathbb{H}}']\}_{i=1,2,\cdots,LR}$. After that, we take the maximum of the multiple combined TRRS evaluated at the same training location ℓ but with different realization index r, expressed by

$$\mathcal{TR}_\ell = \max_{\substack{i=(\ell-1)R+r \\ r=1,2,\cdots,R}} \mathcal{TR}[\widehat{\mathbb{H}}_i, \widehat{\mathbb{H}}'] , \tag{4.1}$$

Now, we define a total of $L+1$ hypothesis $\mathcal{H}_0, \mathcal{H}_1, \mathcal{H}_2, \cdots, \mathcal{H}_\ell, \cdots, \mathcal{H}_L$, where $\mathcal{H}_{\ell,\ell\neq0}$ stands for the hypothesis that the device is located at location ℓ in the training

phase, and $\mathcal{H}_0$ represents the hypothesis that the device is located at an unknown location excluded from the training phase. We determine that $\mathcal{H}_{\ell,\ell\neq0}$ is true, i.e., the device is located at the ℓ-th location in the training database, if the following two conditions are satisfied:

$$\mathcal{TR}_\ell \geq \Gamma, \ \mathcal{TR}_\ell = \max_{\ell'=1,2,\cdots,L} \mathcal{TR}_{\ell'} \ , \tag{4.2}$$

where Γ is a threshold in the range of $[0,1]$. On the other hand, if $\mathcal{TR}_\ell \leq \Gamma$, $\forall \ell = 1, 2, \cdots, L$, we determine that $\mathcal{H}_0$ is true, i.e., we are unable to localize the device since there is no match between the instantaneous CFRs and those in $\mathbf{D}_{\text{train}}$.

4.1.3   Configuration of Threshold

The IPS performance is significantly affected by Γ. A well-chosen Γ leads to a high detection rate and incurring negligible false alarm rate. The detection rate, denoted by $P_D(\Gamma)$, characterizes the probability that the IPS successfully determines the correct locations of the device under Γ, while the false alarm rate, denoted as $P_F(\Gamma)$, captures the possibility that the IPS makes incorrect decisions on the device location under Γ.

With a constraint imposed on the detection rate as $P_{D,0}$ and the false alarm rate as $P_{FA,0}$, the IPS learns Γ automatically from CFRs in $\mathbf{D}_{\text{train}}$ in the training phase. First of all, the IPS computes the TRRS matrix $\mathbf{R}$ based on all CFRs in the training database $\mathbf{D}_{\text{train}}$, with the (i,j)-th entry of $\mathbf{R}$ given by $\mathcal{TR}[\widehat{\mathbb{H}}_i, \widehat{\mathbb{H}}_j]$, where $\widehat{\mathbb{H}}_i$ and $\widehat{\mathbb{H}}_j$ are the i-th and j-th CFR captured in the training phase, respectively. Notice that $[\mathbf{R}]_{i,i} \triangleq 1$. Then, the IPS evaluates $(P_D(\Gamma), P_{FA}(\Gamma))$ for a variety for Γ,

until it finds a specific $\Gamma^\star$ such that $P_D(\Gamma^\star) \geq P_{D,0}$ and $P_{FA}(\Gamma^\star) \leq P_{FA,0}$. Finally, $\Gamma^\star$ is utilized as the threshold in the positioning phase shown in (4.2).

Figure 4.1: Setups for the experiments.
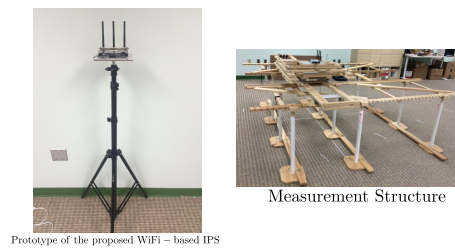
Figure 4.2: The WiFi prototype for the proposed IPS and the measurement structure used in the experiments.

4.2 Experimental Results

4.2.1 Experimental Settings

4.2.1.1 Environment

The experiments are conducted in a typical office in a multi-storey building. The indoor space is occupied by desks, computers, chairs, and shelves.

4.2.1.2 Devices

We build several prototypes equipped with off-the-shelf WiFi devices. Each WiFi device is equipped with 3 omnidirectional antennas to support 3×3 MIMO configuration. Based on functionalities, these WiFi devices can be further classified as APs and Stations (STAs). The center frequency of each AP is configured as 5.24 GHz. The prototype is shown in Fig. 4.2.

4.2.1.3 Details of Experiments

We conduct 7 experiments in total to assess the performance of the proposed IPS with settings illustrated in Fig. 4.1. Experiment (Exp.) $1 \sim 4$ are conducted under a measurement resolution of $5cm$ to analyze the performance under a static and a dynamic environment with details given below.

Exp. 1 investigates the localization performance of the proposed algorithm with a $5cm$ resolution. The WiFi devices are placed under the LOS setting, denoted as Exp. 1a, as well as the NLOS setting, denoted as Exp. 1b. For each

experiment, we measure the CFRs of 100 locations on a measurement structure as shown in Fig 4.2. The measurement resolution is $d = 5cm$. For each location, 10 CFRs are measured.

Exp. 2 sheds light on the impact of human activities. One participant is asked to walk randomly in the vicinity of the STA on the measurement structure with $d = 5cm$ as the unit distance. The distances between the participant and the STA range from 8 to 10 feet. The AP is placed at the same NLOS position as in Exp. 1b. CFRs from 40 different locations on the structure are collected, with 10 CFRs per location.

Exp. 3 analyzes the localization performance when we introduce environment dynamics via moving the furniture in the office. We measure a total of 5 locations on the measurement structure with a resolution of $5cm$. For each location, we first measure 10 CFRs without furniture movement, followed by another 10 CFRs measured after we move the position of a desk near the measurement structure. Then, we measure 10 CFRs after we move a chair in the conference room and the last 10 CFRs after we move another chair in the conference room.

Exp. 4 studies the impact of door opening/closing on the localization performance. The AP is placed in an office room, with STA located in a closet near the entrance of the office suite. The direct link between the AP and the STA is blocked by two concrete walls. Then, a participant is asked to open and close the door of a room in the middle between the AP and STA. CFRs from 4

positions in the closet are captured with 10 CFRs per location for each door status.

On the other hand, Exp. 5 $\sim$ 7 studies several important aspects of the proposed IPS, where

Exp. 5 studies the achievable accuracy of proposed IPS. The STA is placed at the same measurement structure with Exp. 1, but with a much finer resolution with $d = 0.5cm$. CFRs from a total of 400 locations on the grid points of a rectangular area are measured, with 5 CFRs per location.

Exp. 6 studies the effect of the variations in the synchronization parameters. The positions of the AP and the STA are fixed, and we turn on and off the power of the AP to enforce the reinitialization the phase locked loop at the AP. The power cycling is repeated 20 rounds with 10 CFRs for each round.

Exp. 7 analyzes the long-term behavior of the IPS. One AP and four STAs are deployed in the office with positions shown in Fig. 4.1(g). The CFRs are collected every 10 minutes from the four STAs. The IPS is kept running for 631 hours (26 days) continuously. For each measurement, we collect 5 CFRs from each STA. In the 26 days of measurement, the office is fully occupied by around ten people during weekdays and occasionally occupied during weekends. Also, the furniture is moved randomly every day.

The effective bandwidths W_e in the experiments is calculated from (2.34) with $N_u = 114$, $N = 128$, and $D = 1, 2, 3, \cdots, 9$, with the maximum W_e as 321 MHz obtained by exploiting all available links under the 3×3 MIMO configuration, e.g., $D = 9$.

4.2.2 Metrics for Performance Evaluation

For Exp. $1, 2, 3, 4$, we evaluate the detection rate $P_D(\Gamma^\star)$ and the false alarm rate $P_{FA}(\Gamma^\star)$ under threshold $\Gamma^\star$. More specifically, we choose 5 out of the 10 CFRs of each location randomly and consider them as the CFRs obtained in the training phase for each location-of-interest, which are assembled into the training database $\mathbf{D}_{\text{train}}$. The remaining 5 CFRs of each location are considered as the CFRs obtained in the positioning phase and are arranged into the testing database denoted by $\mathbf{D}_{\text{test}}$.

Using the scheme presented in Section 4.1, we calculate $P_D(\Gamma)$ and $P_{FA}(\Gamma)$ for $\Gamma \in [0, 1]$ based on the TRRS matrix $\mathbf{R}$ calculated from $\mathbf{D}_{\text{train}}$. By comparing $P_D(\Gamma)$ against $P_{FA}(\Gamma)$ under various Γ, we demonstrate the receiver operating characteristic (ROC) curve to highlight the trade-offs between detection and false alarm. Then, we choose the minimum $\Gamma^\star$ that satisfies the objective $P_D(\Gamma^\star) \geq 95\%$, $P_{FA}(\Gamma^\star) \leq 2\%$ as the threshold. Lastly, we calculate the TRRS matrix $\mathbf{R}'$ from $\mathbf{D}_{\text{test}}$ and evaluates $P_D'(\Gamma^\star)$ and $P_{FA}'(\Gamma^\star)$ based upon $\mathbf{R}'$ and $\Gamma^\star$. To fully utilize the collected CFRs, we repeat this process 5 times by randomizing the selections of CFRs for the training phase and positioning phase. Finally, we compute the average of $\Gamma^\star$, $P_D'(\Gamma^\star)$, and $P_{FA}'(\Gamma^\star)$, denoted as $\overline{\Gamma^\star}$, $\overline{P}_D'$, and $\overline{P}_{FA}'$, respectively.

In Exp. 5, we illustrate the distribution of the TRRS on the measurement structure. In particular, we assemble the CFRs obtained from the middle point of the $10cm \times 10cm$ rectangular grid into $\mathbf{D}_{\text{train}}$, and keep the CFRs of all locations into $\mathbf{D}_{\text{test}}$. Then, we compute the TRRS matrix $\mathbf{R}$ based on $\mathbf{D}_{\text{train}}$ and $\mathbf{D}_{\text{test}}$.

In Exp. 6, we build $\mathbf{D}_{\text{train}}$ with all CFRs, with $\mathbf{D}_{\text{test}}$ the same as $\mathbf{D}_{\text{train}}$. Thus,

the TRRS matrix $\mathbf{R}$ encapsulates the impact of time-varying synchronization parameters on the localization performance.

In Exp. 7, for each STA, we construct $\mathbf{D}_{\mathsf{train}}$ using the 5 CFRs collected in the first measurement, and keeps all CFRs measured at different time into $\mathbf{D}_{\mathsf{test}}$. After calculating the TRRS matrix $\mathbf{R}$, we take the column average of $\mathbf{R}$, denoted as $\overline{\mathbf{R}}$, which represents the average TRRS between the CFR in $\mathbf{D}_{\mathsf{train}}$ and those in $\mathbf{D}_{\mathsf{test}}$ of every 10 minutes. Using $\overline{\mathbf{R}}$, we evaluate the detection rate and false alarm rate.

4.2.3 Performance Evaluation

(a) $W_e = 36$ MHz

(b) $W_e = 178$ MHz

(c) $W_e = 321$ MHz

(d) ROC curve
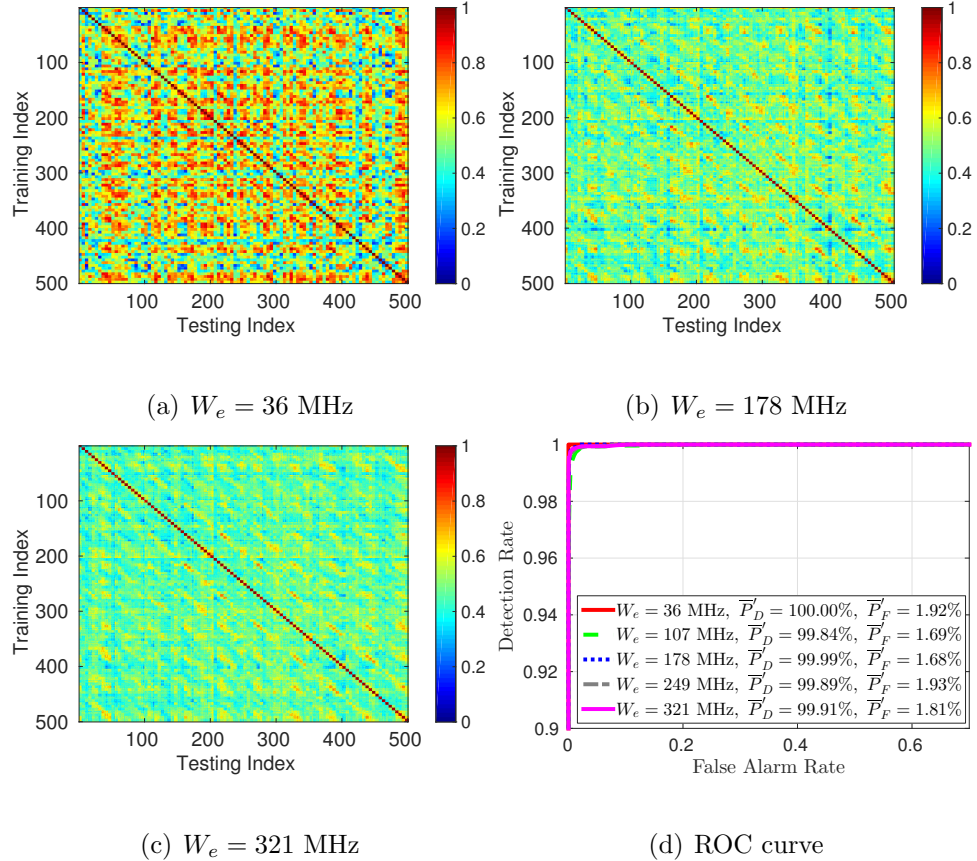
Figure 4.3: Results of Exp. 1a under LOS.

Exp. 1a: LOS with $5cm$ Resolution

In Fig. 4.3(a), (b), (c), we demonstrate the TRRS matrix $\mathbf{R}$ with different W_e under the LOS scenario. As we can see, increasing W_e shrinks the off-diagonal components of $\mathbf{R}$. In other words, a larger W_e alleviates the ambiguity among different locations. On the other hand, the TRRS values measured at the same location only degrades slightly and are still close to 1 with a large W_e. The net effect of using a large W_e is a larger margin between the TRRS calculated at the same location and among different locations, evidencing an enhanced location distinction. The ROC curve in Fig. 4.3(d) demonstrates that the IPS achieves nearly perfect localization performance with $\overline{P}'_D \geq 99.84\%$ and $\overline{P}'_{FA} \leq 1.93\%$ under different W_e. When $W_e = 36$ MHz, we can achieve $\overline{P}'_D = 100\%$ and $\overline{P}'_{FA} = 1.92\%$, which implies that even there exists ambiguity among locations as shown in Fig. 4.3(a) when $W_e = 36$ MHz, we are able to find a good $\overline{\Gamma^\star}$ to distinguish different locations.

However, in general, the threshold $\overline{\Gamma^\star}$ is large when W_e is small. Therefore, under a small W_e, the IPS is highly sensitive to noise and deterioration of CFRs associated with different locations, e.g., when there exists significant environment dynamics due to human or object movement. On the other hand, $\overline{\Gamma^\star}$ is much smaller when W_e is large, which leaves a larger margin for noise and dynamics and thus improves the robustness of the proposed IPS. This is justified by Fig. 4.4, where we demonstrate $\overline{\Gamma^\star}$ under different W_e for Exp. 1a. It can be seen that a threshold as large as 0.86 is required when $W_e = 36$ MHz, which decreases as W_e increases. When $W_e = 321$ MHz, the threshold drops to 0.63.
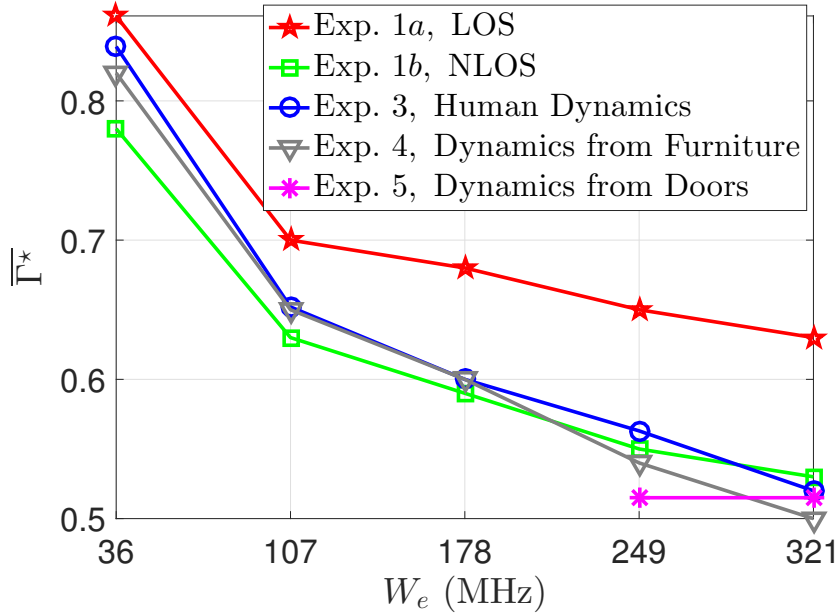
Figure 4.4: $\overline{\Gamma^\star}$ under different W_e.

Exp. 1b: NLOS with $5cm$ Resolution

In Fig. 4.5(a), (b), (c), we show the TRRS matrix $\mathbf{R}$ with different W_e under the NLOS scenario. Comparing with Fig. 4.3(a), (b), (c), we see that the location ambiguity is lower for the NLOS scenario than the LOS scenario, indicating by the smaller TRRS values measured between different locations. This can be justified by that the channel energy spreads over more multipath components under NLOS than LOS and provides richer information of the environment. Similar to the results of Exp. 1a, we find that a larger W_e mitigates the location ambiguity and enhances the overall IPS performance, with $\overline{P}'_D = 100\%$ and $\overline{P}'_{FA} = 1.65\%$ when $W_e = 321$ MHz. Additionally, from Fig. 4.4, we observe that $\overline{\Gamma^\star}$ decreases more rapidly when W_e enlarges than the LOS case, reducing $\overline{\Gamma^\star}$ from 0.78 under $W_e = 36$ MHz to 0.53 when $W_e = 321$ MHz.

(a) $W_e = 36$ MHz

(b) $W_e = 178$ MHz

(c) $W_e = 321$ MHz

(d) ROC curve
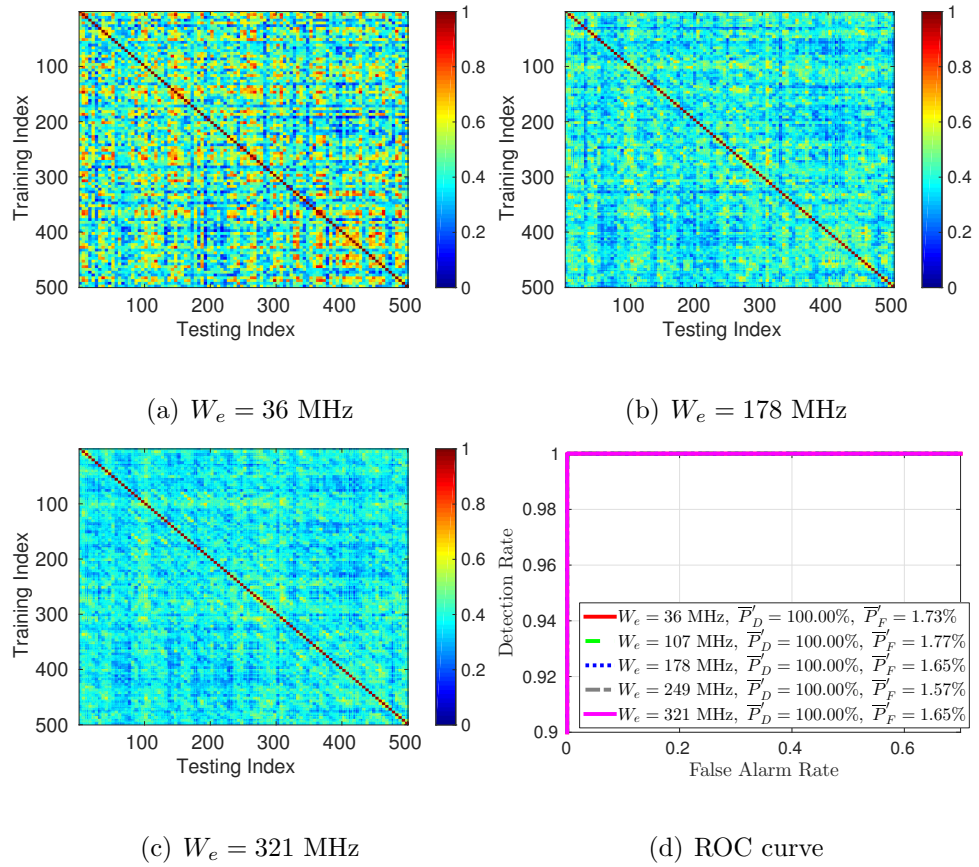
Figure 4.5: Results of Exp. 1b under NLOS.

The negligible false alarm rates in Exp. 1 also imply that the localization error is $0cm$ under most cases. In fact, the false alarm rates can be further reduced by increasing $\overline{\Gamma^{\star}}$, leading to a false alarm rate of 0.06% and a detection rate of 99.48% under $\overline{\Gamma^{\star}} = 0.74$ for the LOS case, and 0% false alarm rate and a detection rate of 99.45% under $\overline{\Gamma^{\star}} = 0.71$.

Exp. 2: Effect of Human Activities

(a) $W_e = 36$ MHz

(b) $W_e = 178$ MHz

(c) $W_e = 321$ MHz

(d) ROC curve
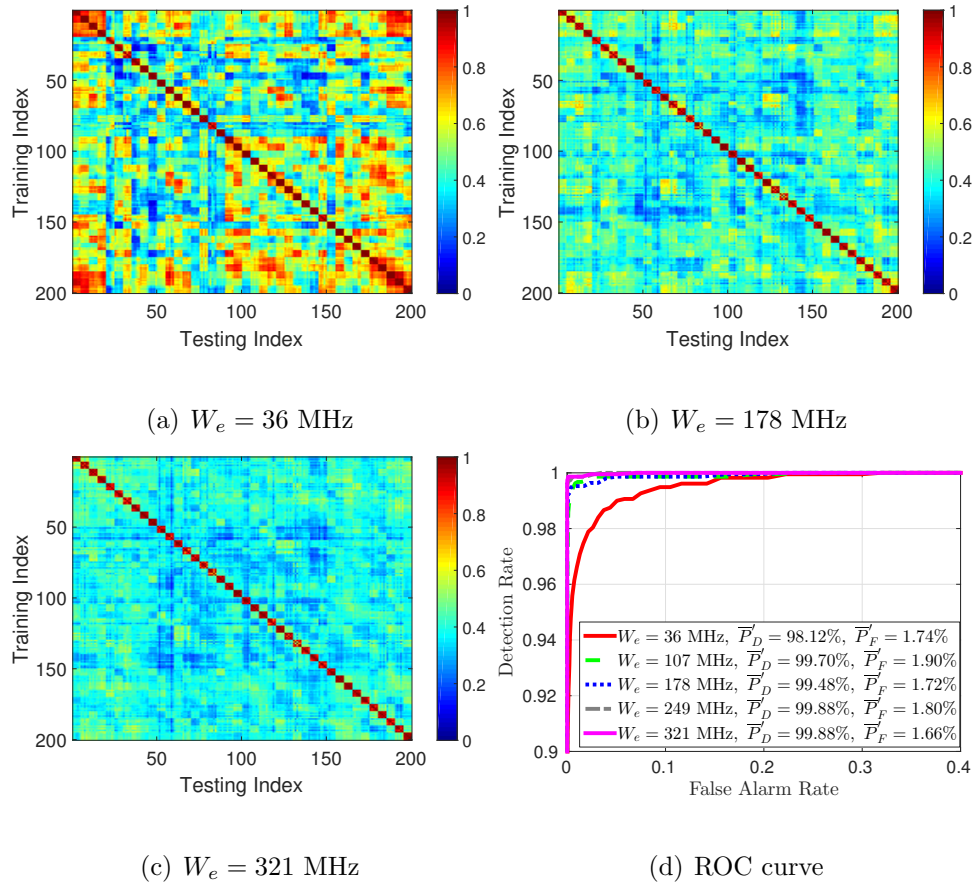
Figure 4.6: Results of Exp. 2 with human dynamics.

Fig. 4.6 shows the impact of human activities on the performance of the proposed IPS. From Fig. 4.6(a), (b), (c), we find that a large W_e improves the robustness

against environment dynamics. Fig. 4.6(d) illustrates the ROC curve using different W_e and further verifies that a large W_e can enhance the localization performance, leading to $\overline{P}'_D = 99.88\%$ and $\overline{P}'_{FA} = 1.66\%$ when $W_e = 321$ MHz. As shown in Fig. 4.4, when $W_e = 321$ MHz, a threshold of 0.52 suffices to achieve a good performance.

(a) $W_e = 36$ MHz

(b) $W_e = 178$ MHz

(c) $W_e = 321$ MHz

(d) ROC curve
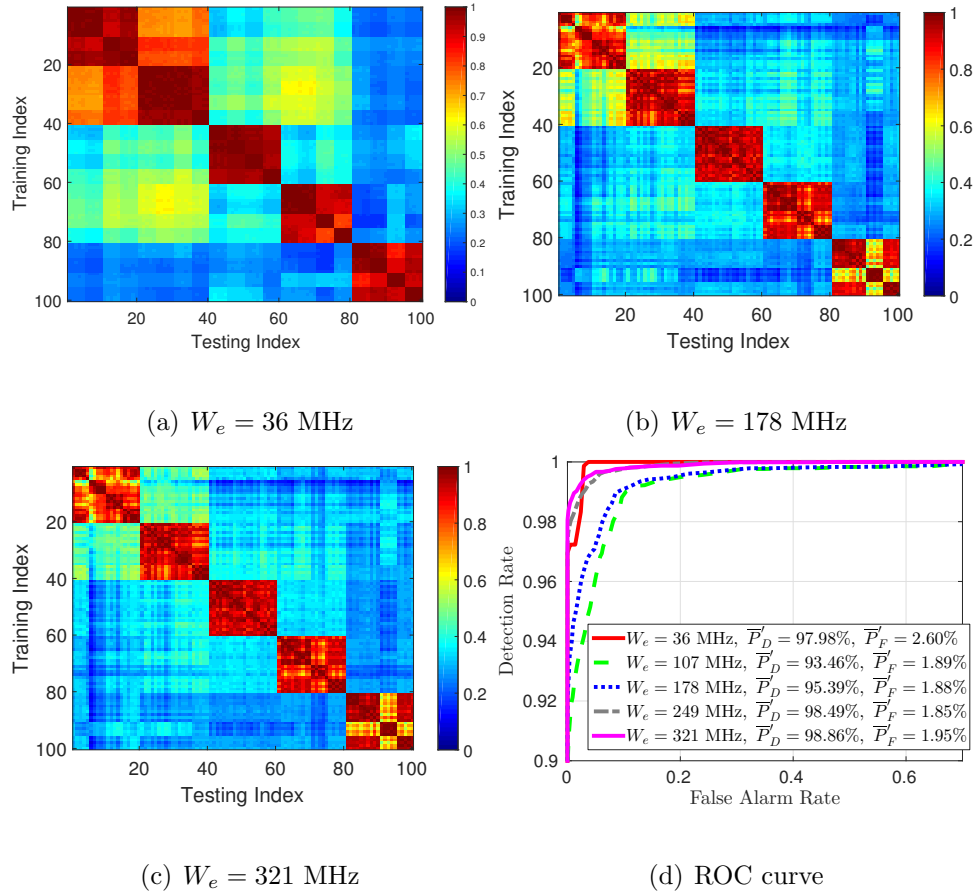
Figure 4.7: Results of Exp. 3 with furniture movement.

Exp. 3: Impact of Furniture Movement

In Fig. 4.7, we show the performance in the presence of furniture movement. Simi-

lar to the observations in Exp. 1 and Exp. 2, a larger W_e enhances the robustness against the dynamics from furniture movement and reduces ambiguity among locations. As can be seen from Fig. 4.7, location 1 and location 2 are highly correlated implied by a large TRRS value, and the ambiguity between location 1 and 2 is alleviated when W_e increases to 178 MHz and 321 MHz, leading to an improved detection rate and false alarm rate. When $W_e = 321$ MHz, we achieve $\overline{P}'_D = 98.86\%$ and $\overline{P}'_{FA} = 1.95\%$ under a threshold of 0.50 as shown in Fig. 4.4.

Also, we notice that the performance does not improve monotonically with W_e. This is because the quality of different links in the multi-antenna WiFi system differs due to the discrepancy in their noise and interference levels. Thus, combining multiple links based on the channel energies might not be optimal in this case. This can be solved by calculating the TRRS using criterion robust against noise and interference on different WiFi links.

Exp. 4: Impact of Door

The impact of door status on localization is more severe than the human activities when the door acts as a major reflector in the propagation of electromagnetic waves and thus its status greatly affects the CFRs.

In Fig. 4.8, we illustrate the results under different W_e. Obviously, a large W_e is indispensable in this case, since the TRRS values measured at location 1 and 2 degrade to 0.42 and 0.17 under different door status with $W_e = 36$ MHz, and the IPS fails to find a $\Gamma^\star$ to achieve at least 95% detection rate and at most 2% false

(a) $W_e = 36$ MHz

(b) $W_e = 178$ MHz

(c) $W_e = 321$ MHz

(d) ROC curve
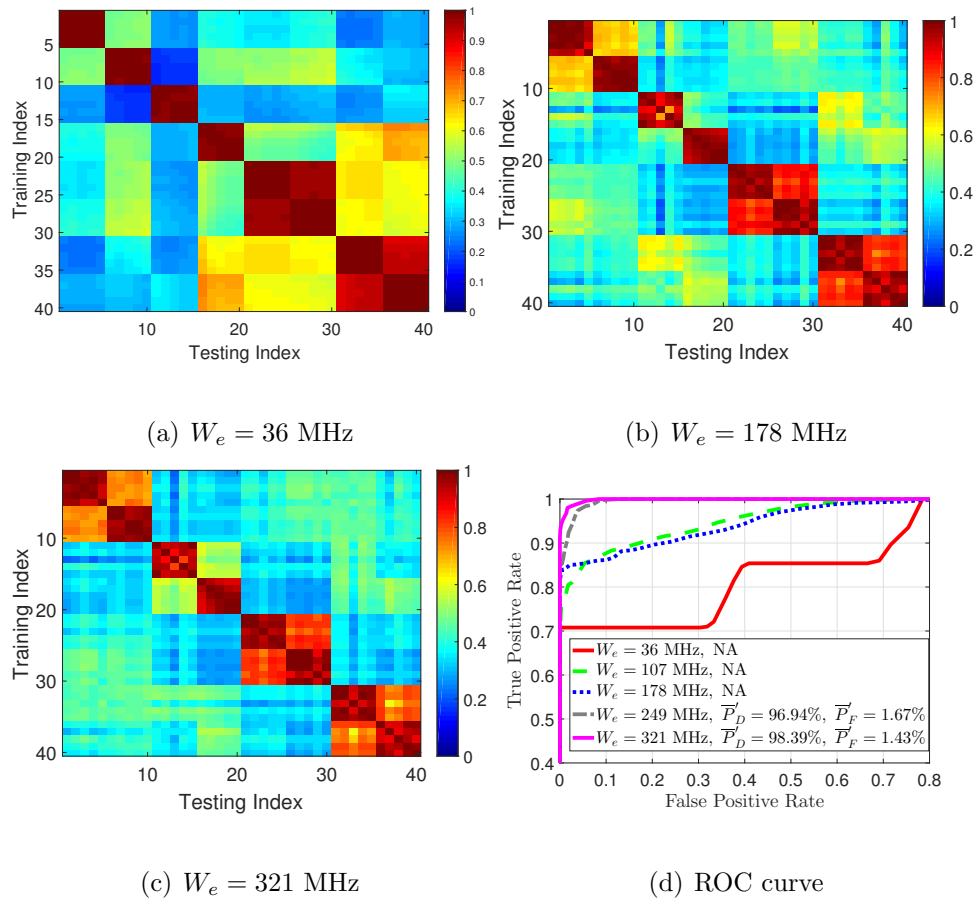
Figure 4.8: Results of Exp. 4 with door effect.

alarm rate. On the other hand, increasing W_e increases to 321 MHz partially recovers the similarities of the CFRs collected at the same location with different door status, and we achieve $\overline{P}'_D = 98.39\%$ and $\overline{P}'_{FA} = 1.43\%$. This could be justified by the inherent spatial diversity naturally existing in multi-antenna WiFi systems since different links can be considered uncorrelated and thus sense the environment from different perspectives. Therefore, even the door affects a majority of the multipath components on some WiFi links, its impact on other WiFi links is much less pronounced. Fig. 4.4 shows that the target of more than 95% detection rate and less than 2% false alarm rate is achievable when $W_e \geq 249$ MHz. In conclusion, a large W_e is paramount for the proposed IPS when there exists strong environmental dynamics.
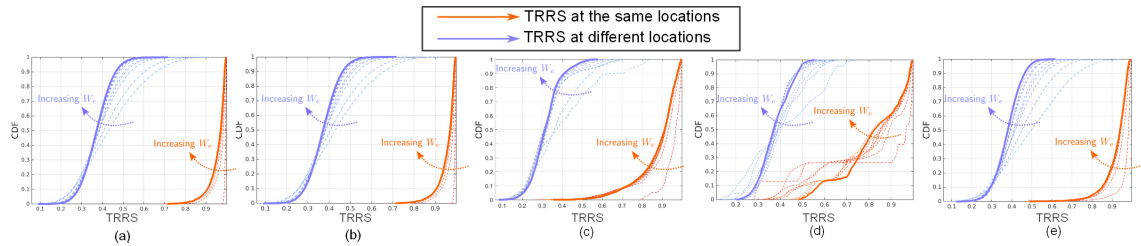
Figure 4.9: Impact of W_e on the TRRS. (a) Exp. 1a, LOS under static environment (b) Exp. 1b, NLOS under static environment (c) Exp. 2, dynamic environment with human activities (d) Exp. 3, dynamic environment with furniture movement (e) Exp. 4, dynamic environment with door opening and closing.

Impact of Effective Bandwidth on the CDF of TRRS

We observe from the analysis on the results of Exp. 1, 2, 3, and 4 that the gap between the TRRS measured at the same locations and among different locations enlarges with respect to an increased W_e. To further validate the observation, we draw the cumulative density functions (CDFs) of the TRRS values in Fig. 4.9 under various W_e, where the solid lines represent the CDFs with $W_e = 321$ MHz. It shows that the TRRS values among different locations are more concentrated in a region with a small average of TRRS when W_e is large, while the TRRS values measured at the same locations are still highly concentrated in a region with an average TRRS close to 1 for Exp. 1a and Exp. 1b. The decrease of the TRRS at the same location is more significant for Exp. 2, 3, and 4. Yet, the degradation is still within the tolerance level as implied by the $\overline{P}'_D$ and $\overline{P}'_{FA}$ performances. Therefore, it is crucial to use a large W_e to enhance both performance and robustness.
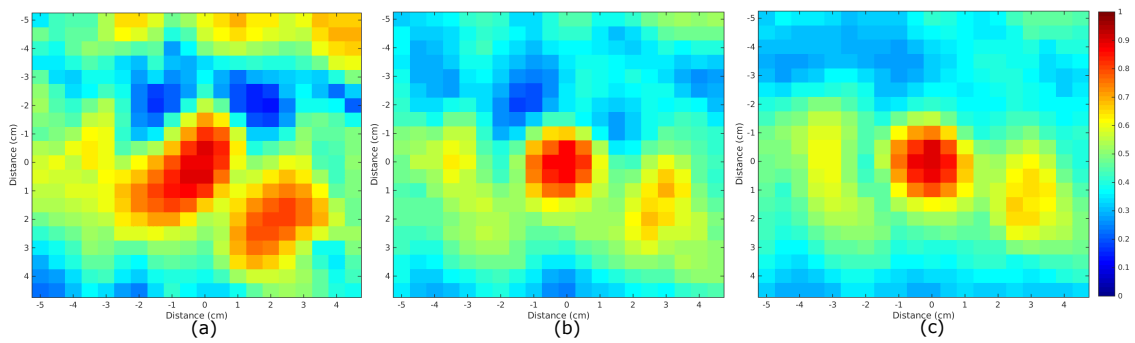
Figure 4.10: Results of Exp. 5 under a measurement resolution of $0.5cm$. (a) $W_e = 36$ MHz (b) $W_e = 178$ MHz (c) $W_e = 321$ MHz.

Exp. 5: Results under $0.5cm$ Measurement Resolution

Fig. 4.10(a), (b), (c) visualize the TRRS matrix $\mathbf{R}$ calculated under different W_e. We observe that large TRRS values are highly concentrated within a small and uniform circular area with a radius of $1 \sim 2cm$ surrounding the middle point when $W_e \geq 178$ MHz, while the TRRS are more decentralized when $W_e = 36$ MHz.
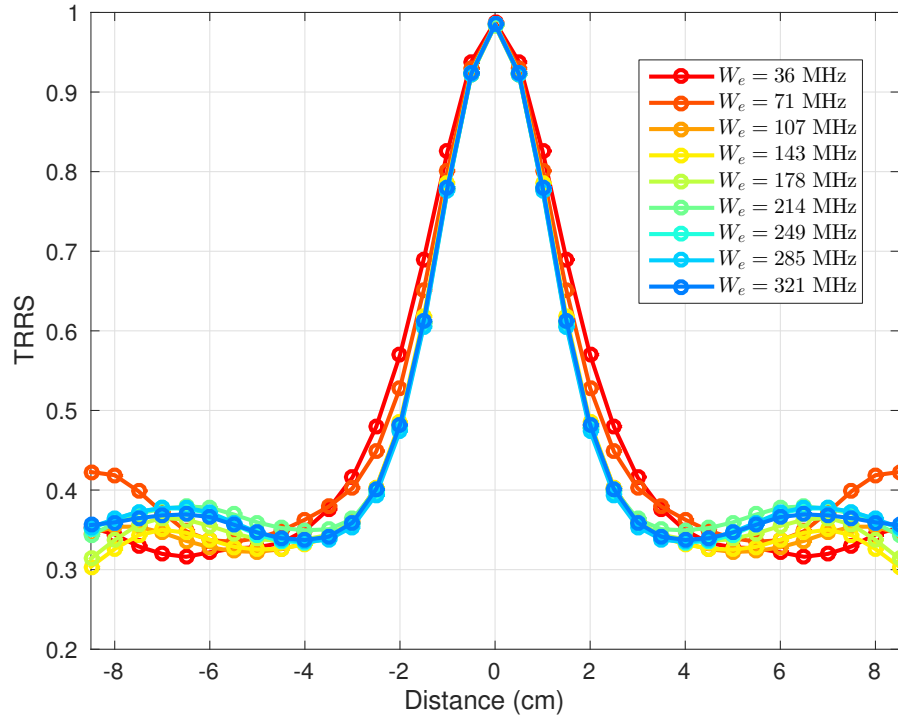
Figure 4.11: Decaying of TRRS with distance in Exp. 5.

Fig. 4.11 shows the average TRRS decay along different directions calculated using $\mathbf{R}$. A larger W_e accelerates the decay of the TRRS values and improves the location distinction. With a distance larger than $1cm$, the TRRS drops below 0.75. Therefore, with an appropriate threshold, the proposed IPS can achieve an accuracy of $1 \sim 2cm$.

Exp. 6: Impact of Power Cycling on Localization Performance
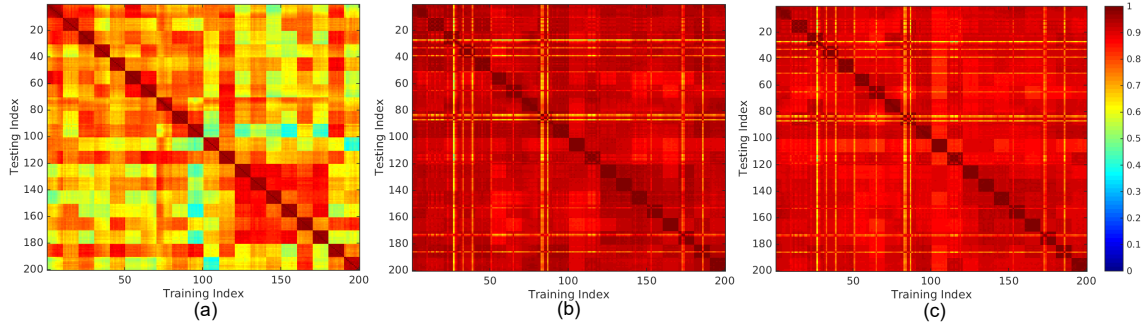
Figure 4.12: Results of Exp. 6. (a) $W_e = 36$ MHz (b) $W_e = 178$ MHz (c) $W_e = 321$ MHz.

Fig. 4.12 shows $\mathbf{R}$ with different W_e for Exp. 7. Clearly, when $W_e = 36$ MHz, there exists large fluctuation in the TRRS and the localization performance is deteriorated. The performance loss can be remedied by using $W_e \geq 178$ MHz, which again demonstrates the importance of a large W_e.

Exp. 7: Localization Performance over 26 Days

In Fig. 4.13, we sketch the time evolution of the TRRS evaluated at the same STA locations and among different STA locations for different STAs in the 26 days of measurement. We observe that the TRRS changes with time due to the environment variations. We also find that when $W_e = 321$ MHz, the decay in TRRS is less severe than the case with $W_e = 36$ MHz.

In Fig. 4.13(e),(j),(o), we display the ROC curves for the 4 STAs under different W_e. Obviously, in comparison with the results of $W_e = 36$ MHz, using a W_e as large as 178 MHz and 321 MHz combats the degradation incurred by inevitable environment changes and improves the IPS performance by a large margin. There-
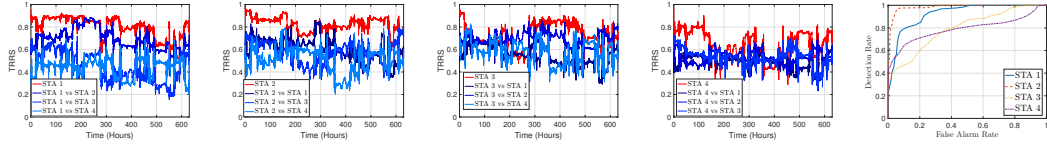
(a) STA 1,W_e = 36 MHz

(b) STA 2,W_e = 36 MHz

(c) STA 3,W_e = 36 MHz

(d) STA 4,W_e = 36 MHz

(e) W_e = 36 MHz, ROC
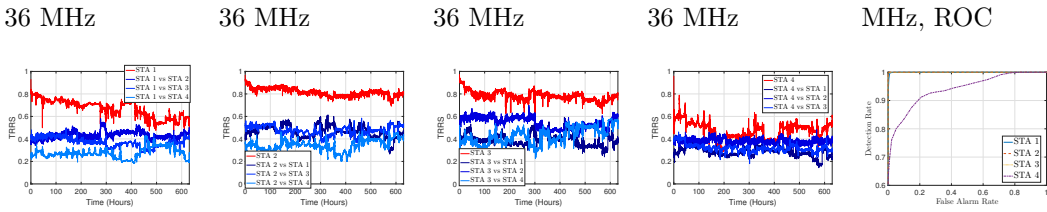
(f) STA 1,W_e = 178 MHz

(g) STA 2,W_e = 178 MHz

(h) STA 3,W_e = 178 MHz

(i) STA 4,W_e = 178 MHz

(j) W_e = 178 MHz, ROC
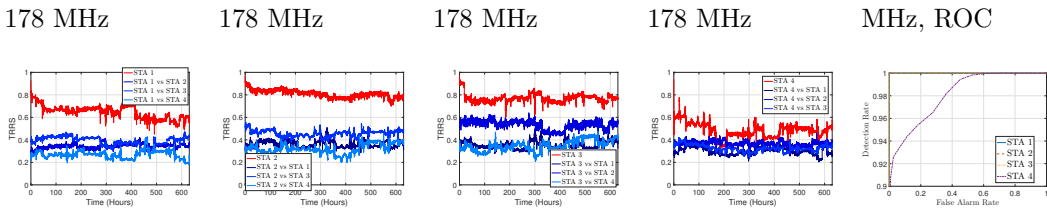
(k) STA 1,W_e = 321 MHz

(l) STA 2,W_e = 321 MHz

(m) STA 3,W_e = 321 MHz

(n) STA 4,W_e = 321 MHz

(o) W_e = 321 MHz, ROC

Figure 4.13: Results of Exp. 7 over 26 days of measurement.

fore, using a large W_e can greatly reduce the overhead introduced by the training phase since it becomes unnecessary to update $\mathbf{D}_{\text{train}}$ frequently.

Although the distances between the STAs in this experiment exceed $5cm$, the results would be very similar if these STAs are placed closer at a centimeter level with a large W_e. This is because the TRRS values calculated between two locations are identical as long as the distance between them exceeds $5cm$ as shown in Fig. 4.3 and Fig. 4.5.

Results under a Universal $\Gamma^\star$

In Exp. 1, 2, 3, 4, we assume that the proposed IPS learns a specific $\Gamma^\star$ from $\mathbf{D}_{\text{train}}$ to achieve $\overline{P}'_D \geq 95\%$ and $\overline{P}'_{FA} \leq 2\%$. In practice, due to the randomness of the environment, we might only be able to roughly find a fixed $\Gamma^\star$ based on a very limited training database without much dynamics and the performance might degrade consequently. To investigate the performance loss under a fixed $\Gamma^\star$, we configure $\Gamma^\star$ as 0.6 and W_e as 321 MHz.

The performances are summarized into Table 4.1, which shows that except Exp. 4, the proposed IPS still achieves a detection rate higher than 96.61% with a false alarm rate smaller than 3.96%. The performance of Exp. 4 degrades but still maintains a detection rate of 85% and a false alarm rate of 0.

In practice, we perform a large number of experiments in a variety of environment. The results reveal that the $1 \sim 2$cm accuracy is universal instead of limited only to a small area, given that the number of multipath components is sufficient.

	Exp. 1 LOS	Exp. 1 NLOS	Exp. 2 Human Activities	Exp. 3 Furniture Movement	Exp. 4 Door Effect
Detection Rate (%)	99.94	100	99.72	96.61	85.00
False Alarm Rate (%)	3.96	0.14	0.01	0	0

Table 4.1: Performances with $\Gamma = 0.60$ and $W_e = 321$ MHz.

4.3 Summary

In this chapter, we have proposed a WiFi-based IPS leveraging the TR focusing effect that achieves centimeter-level accuracy for indoor localization. The proposed IPS fully utilize the spatial diversity in MIMO-OFDM WiFi systems to formulate a large effective bandwidth. Extensive experimental results show that with a measurement resolution of $5cm$, the proposed IPS achieves true positive rates of 99.91% and 100%, and incurs false positive rates of 1.81% and 1.65% under the LOS and NLOS scenarios, respectively. Meanwhile, the IPS is robust against the environment dynamics caused by human activities and object movements. Experiment results with a measurement resolution of $0.5cm$ demonstrate a localization accuracy of $1 \sim 2cm$ achieved by the proposed IPS.

Chapter 5

High Accuracy Vital Sign Monitoring

In addition to centimeter accuracy indoor localization presented in Chapter 3
and Chapter 4, vital sign monitoring is another very important functionality in the
IoT ecosystem. In this chapter, we show the feasibility of using CFRs and time-
reversal technique for vital sign monitoring by proposing TR-BREATH, a WiFi-
based contact-free breathing monitoring system that detects and monitors multi-
person breathing.

Conventional breathing monitoring schemes are invasive in that physical con-
tact with human bodies is a must. Contact-free breathing monitoring schemes are
developed to overcome the drawbacks of conventional schemes for in-home breathing
monitoring. Among them, schemes driven by RF techniques are the most promising
candidates due to their abilities to sense breathing in a highly complicated indoor
environment by leveraging the propagation of EM waves. In terms of techniques,
these schemes can be classified into radar-based and WiFi-based. Among the radar-
based schemes, Doppler radar is commonly used which measures the frequency shift
of the signals caused by the periodic variations of the EM waves reflected from
human bodies [47]. Recently, Adib *et al.* present a vital sign monitoring system
that uses USRP as the RF front-end to emulate a frequency modulated continuous

radar (FMCW) [11]. However, the requirement of specialized hardware hinders the deployment of these schemes.

On the other hand, WiFi-based schemes are infrastructure-free since they are built upon the existing WiFi networks available indoor. RSSI is often used due to its availability on most WiFi devices. In [9], Abdelnasser *et al.* present UbiBreathe that harnesses RSSI on WiFi devices for breathing estimation. However, UbiBreathe is accurate only when users hold the WiFi devices close to their chests. Another exploitable information on WiFi devices is CFR, a fine-grained information that portraits the EM wave propagation. The scheme proposed by Liu *et al.* in [40] is one of the first few CFR-based breathing monitoring approaches. Nevertheless, they assume the number of people to be known. Moreover, periodogram is used for spectral analysis that needs a relatively long time for accurate breathing monitoring.

TR-BREATH characterizes the CFR temporal variations via TRRS. The TRRS values are further analyzed by the Root-MUSIC algorithm to produce breathing rate candidates. Key statistics are derived based on these candidates to facilitate breathing detection. In detection of breathing, TR-BREATH estimates the multi-person breathing rates via affinity propagation [32], likelihood assignment, and cluster merging. Based on the resultant cluster likelihoods, TR-BREATH formulates an estimation on the number of people. Also, TR-BREATH makes full use of the sequence numbers in WiFi packets to enhance its robustness against packet loss, which is very common in areas with a dense deployment of WiFi devices.

Extensive experiments in an office environment demonstrate a perfect detection rate for breathing within 63 seconds of measurements. Moreover, with only

10 seconds of measurements, TR-BREATH achieves 99% accuracy for single-person breathing rate estimation under NLOS scenarios. For multi-person breathing monitoring, TR-BREATH achieves a mean accuracy of 98.65% for a dozen people under LOS and 98.07% for 9 people under NLOS, both with 63 seconds of measurement. With the knowledge of the maximum number of people, TR-BREATH can count the people number with an error around 1. Moreover, TR-BREATH is robust against packet loss which is very common in indoor spaces.

The rest of this chapter is organized as follows. Section 5.1 elaborates on the algorithm of TR-BREATH. Section 5.2 demonstrates the experimental results for both single-person and multi-person LOS and NLOS scenarios. Section 5.3 demonstrates the performances of TR-BREATH in the presence of a few practical issues. Finally, Section 5.4 concludes this chapter.

5.1 Algorithm

In this section, we first explain how to extract breathing information from the TRRS matrix. Then, we present the details of different modules of TR-BREATH in details.

Remark 1 *In TR-BREATH, CFRs are collected from multiple links on a specific WiFi channel, i.e., $F = 1$. The total number of links is given as $D = N_{tx} \times N_{rx}$.*

Remark 2 *In TR-BREATH, we calculate the complex-valued TRRS $\mathcal{TR}_\phi[\widehat{\mathbf{H}}, \widehat{\mathbf{H}'}]$ instead of the real-valued TRRS $\mathcal{TR}[\widehat{\mathbf{H}}, \widehat{\mathbf{H}'}]$. This is mainly because that the phase information embedded in the CFR is also very important for breathing monitoring*

in addition to the amplitude.

5.1.1   Extracting Breathing Rates using Root-MUSIC

Root-MUSIC is a variant to the well-known MUltiple SIgnal Classification (MUSIC) algorithm [51]. It is a super-resolution subspace-based spectral analysis algorithm widely used in signal processing applications [49]. Assume a total of N CFRs sampled uniformly with an interval of T_s, we can calculate the $N \times N$ TRRS matrix $\mathbf{R}$ based on (2.31); the (i,j)-th element of $\mathbf{R}$ given as $\mathcal{TR}_\phi \left[\widehat{\mathbb{H}}[i], \widehat{\mathbb{H}}[j] \right]$ where $\widehat{\mathbb{H}}[i]$ stands for the i-th sampled multi-link CFR.

After calculating $\mathbf{R}$, we perform an eigenvalue decomposition (EVD) on $\mathbf{R}$ to produce

$$\mathbf{R} = \mathbf{U}\boldsymbol{\Lambda}\mathbf{U}^\dagger \, , \tag{5.1}$$

where $\dagger$ is the transpose and conjugate operator, $\mathbf{U}$ is a $N \times N$ orthogonal matrix such that $\mathbf{U}^\dagger\mathbf{U} = \mathbf{I}$ where $\mathbf{I}$ is a $N \times N$ identity matrix, and $\boldsymbol{\Lambda}$ is a $N \times N$ diagonal matrix with descending real-valued diagonal entries equivalent to the eigenvalues of $\mathbf{R}$.

Secondly, the orthogonal matrix $\mathbf{U}$ is decomposed into a signal subspace and a noise subspace. The signal subspace, denoted by $\mathbf{U}_s$, consists of the first p columns of $\mathbf{U}$, where $p \leq N - 1$ is the signal subspace dimension. On the other hand, the noise subspace, denoted by $\mathbf{U}_n$, consists of the last $N - p$ columns of $\mathbf{U}$.

Next, we calculate the matrix $\mathbf{Q} = \mathbf{U}_n\mathbf{U}_n^\dagger$ where $\mathbf{X}^\dagger$ stands for the Hermitian

or conjugate transpose of matrix $\mathbf{X}$. Then, we formulate the polynomial $f(z)$ as

$$f(z) = \sum_{m=0}^{N-1} \sum_{n=0}^{N-1} [\mathbf{Q}]_{m,n} \, z^{g_{m,n}} \,, \qquad (5.2)$$

where $[\mathbf{Q}]_{m,n}$ is the (m,n)-th element of $\mathbf{Q}$, $z = e^{-j\frac{2\pi b T_s}{60}}$, and $g_{m,n}$ is the *discrete difference function* highlighting the time difference between two CFRs normalized to T_s which is given as

$$g_{m,n} = \begin{cases} s_m - s_n, & \text{Considering Packet Loss} \\[2ex] m - n, & \text{Otherwise .} \end{cases} \qquad (5.3)$$

By using $g_{m,n} = s_m - s_n$, the Root-MUSIC algorithm is more robust against WiFi packet loss. Yet, when the ambient WiFi traffic is not severe, setting $g_{m,n}$ as $m - n$ suffices.

Solving $f(z) = 0$ in (5.2) results in $2N - 2$ complex roots denoted by $\hat{\mathbf{z}} = \{\hat{z}_1, \hat{z}_2, \hat{z}_3, \cdots, \hat{z}_{2N-2}\}$. Since $\mathbf{Q}$ is Hermitian, if $\hat{z}$ is a complex root of $f(z) = 0$, then $1/\hat{z}^*$ is also a complex root of $f(z) = 0$. In other words, the roots of $f(z) = 0$ come in pairs. Considering that only the phase of the complex roots carry the information about the breathing rates, we keep the $N - 1$ complex roots inside the unit circle. Then, we choose p out of the $N - 1$ complex roots closest to the unit circle where p is the signal subspace dimension. The breathing rate estimation can be formulated as

$$\hat{b}_i = 60 \times \frac{\angle \hat{z}_i}{2\pi T_s}, \quad i = 1, 2, \cdots, p \qquad (5.4)$$

where $\angle(x)$ takes the angle of the complex variable x.

Remark 3 *When there exists interference from other moving objects nearby, some*

of these complex roots might be associated with the motion interference. In partic-

ular, under some circumstances, the power of the motion interference can be even

stronger than the breathing signal. Fortunately, as shown in Section 5.3, as long as

the WiFi devices are far away from the motions, the impact of motion can be largely

neglected, and most of the complex roots of $f(z)$ in (5.2) are still associated with

breathing.

Moreover, we realize that the breathing rates are limited to a finite range $[b_{\min}, b_{\max}]$ since people cannot breathe either too fast or too slow, and we sift the breathing rate estimations $\hat{\mathbf{b}} = [\hat{b}_1, \hat{b}_2, \cdots, \hat{b}_p]$ by discarding those outside the range of $[b_{\min}, b_{\max}]$. This leads to a reduced number of breathing rate candidates denoted by $\tilde{\mathbf{b}} = [\hat{b}_{r_1}, \hat{b}_{r_2}, \cdots, \hat{b}_{r_{p'}}]$, where p' is the number of the remaining complex roots and r_i is the index of the i-th remaining estimation.

5.1.2 Architecture of TR-BREATH

The architecture of TR-BREATH is illustrated in Fig. 5.1. We assume the availability of CFRs on a total of $D = N_{tx} \times N_{rx}$ links in a MIMO-OFDM WiFi system.

5.1.3 CFR Sanitization

Due to the synchronization errors as introduced in Chapter 2, the CFRs must be sanitized before they can be used. Different from the explicit sanitization proposed in [52], the CFRs are sanitized implicitly when calculating the TRRS as shown
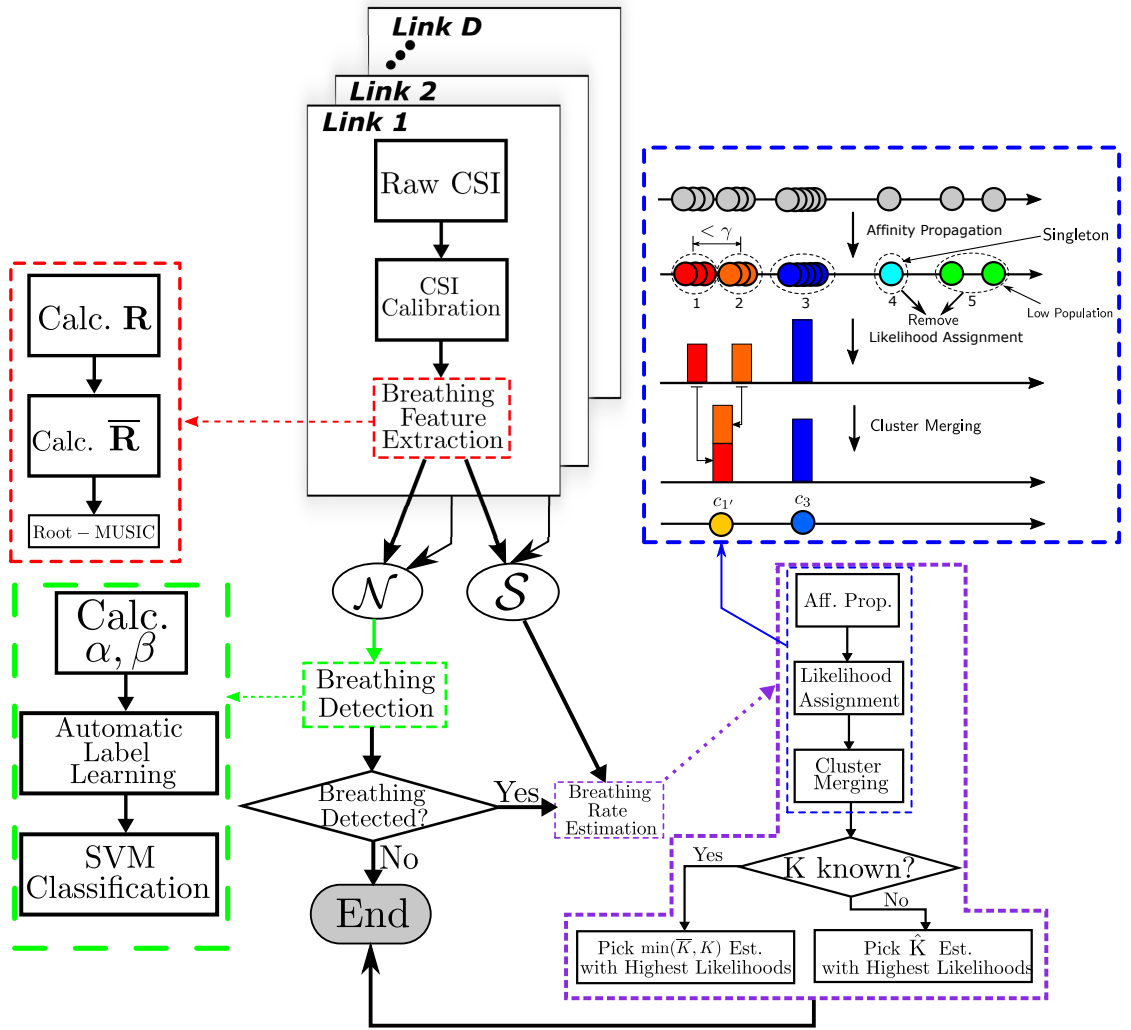
Figure 5.1: Overview of the architecture of TR-BREATH

in (2.31).

5.1.4 Breathing Feature Extraction

5.1.4.1 Calculating the TRRS Matrix

Assume that we obtain N CFRs for each link. Since breathing is not strictly stationary in the long run, calculating the $N \times N$ TRRS matrix $\mathbf{R}$ using the sanitized

CFRs using (2.31) is not optimal. Instead, TR-BREATH operates with multiple time window blocks, where each block consists of M CFRs where $M \leq N$. Assume that two adjacent time window blocks overlap by P CFRs, TR-BREATH can obtain a total of $B = \lfloor \frac{N-P}{M} \rfloor + 1$ blocks.

For each block, TR-BREATH further partitions the block duration into several overlapping time windows with W CFRs for each, with the CFRs associated with the i-th time window given by $\{\widehat{\mathbb{H}[i]}, \widehat{\mathbb{H}}[i+1], \cdots, \widehat{\mathbb{H}}[i+W-1]\}$. Two adjacent time windows overlap by 1 CFRs. Here, $\widehat{\mathbb{H}[i]}$ stands for the i-th CFR vector that contains multi-link CFRs as shown in (2.33).

5.1.4.2 Temporal Smoothing of the TRRS Matrix

To suppress the spurious estimations due to interference, TR-BREATH performs temporal smoothing on the TRRS matrix for each block. It also takes the packet loss into consideration. Firstly, for link d, block b, TR-BREATH parses the sequence numbers for the M CFRs inside that block, denoted by

$$s_{b(N-P)+1}, s_{b(N-P)+2}, \cdots, s_{b(N-P)+M}$$

Then, TR-BREATH calculates the difference M' between the maximum sequence number $s_{\max} = s_{b(N-P)+M}$ and the minimum sequence number $s_{\min} = s_{b(N-P)+1}$. If $M' = s_{\max} - s_{\min} > M$, we infer that $M' - M$ WiFi packets are missing due to ambient WiFi traffic.

Secondly, TR-BREATH calculates the $M \times M$ TRRS matrix for link d and block b according to (2.31), denoted as $\mathbf{R}_{b,d}$. Then, TR-BREATH forms an extended

TRRS matrix $\mathbf{R}'_{b,d}$ with dimension $M' \times M'$. The entries of $\mathbf{R}'_{b,d}$ are initialized with zeros. TR-BREATH fills the (s_i, s_j)-th entry of $\mathbf{R}'_{b,d}$ with the (i,j)-th element of $\mathbf{R}_{b,d}$. Equivalently speaking, $\mathbf{R}'_{b,d}$ is an interpolated version of $\mathbf{R}_{b,d}$, with entries of zero standing for the index of the missing packets *. With a time window size W, TR-BREATH could formulate $Z = M' - W + 1$ time windows in total. Meanwhile, TR-BREATH forms a counting matrix $\mathbf{C}'_{b,d}$ for link d and block b such that

$$[\mathbf{C}'_{b,d}]_{i,j} = \begin{cases} 1, & \text{If } [\mathbf{R}'_{b,d}]_{i,j} > 0 \\ 0, & \text{Otherwise .} \end{cases} \tag{5.5}$$

Next, TR-BREATH partitions $\mathbf{R}'_{b,d}$ into Z square submatrix, with the z-th submatrix given by $\mathbf{R}'_{b,d,z}$ composed by the entries of $\mathbf{R}_{b,d}$ from row z to row $z + W - 1$ and column z to column $z + W - 1$. The same operation is performed on $\mathbf{C}'_{b,d}$, leading to Z square submatrix $\{\mathbf{C}'_{b,d,z}\}_{z=1,2,\cdots,Z}$. $\{\mathbf{R}'_{b,d,z}\}_{z=1,2,\cdots,Z}$ and $\{\mathbf{C}'_{b,d,z}\}_{z=1,2,\cdots,Z}$ are accumulated as $\overline{\mathbf{R}'_{b,d}} = \sum_{z=1}^{Z} \mathbf{R}'_{b,d,z}$ and $\overline{\mathbf{C}'_{b,d}} = \sum_{z=1}^{Z} \mathbf{C}'_{b,d,z}$. Also, we replace the sequence numbers with $[1, 2, \cdots, W]$.

Then, we locate and delete the rows and columns of $\overline{\mathbf{R}'_{b,d}}$ and $\overline{\mathbf{C}'_{b,d}}$ with at least one zero, resulting in the matrix $\overline{\mathbf{R}''_{b,d}}$ and $\overline{\mathbf{C}''_{b,d}}$, both with dimension $W' \times W'$ where $W' \leq W$. The deleted index are also removed from the updated sequence numbers in the previous step, leading to the updated sequence numbers $s''_1, s''_2, \cdots, s''_{W'}$.

Finally, we calculate the temporal smoothed matrix $\overline{\mathbf{R}_{b,d}}$ with its (i,j)-th ele-

---

*For example, $\mathbf{R}_{b,d} = \begin{bmatrix} 1 & 0.95 \\ 0.95 & 1 \end{bmatrix}$ and $s_1 = 1, s_2 = 3$. Then, $\mathbf{R}'_{b,d} = \begin{bmatrix} 1 & 0 & 0.95 \\ 0 & 0 & 0 \\ 0.95 & 0 & 1 \end{bmatrix}$.

ment given by $[\overline{\mathbf{R}''_{b,d}}]_{i,j}/[\overline{\mathbf{C}''_{b,d}}]_{i,j}$ for further processing. Fig. 5.2 shows an example of generating $\overline{\mathbf{R}_{b,d}}$ under $N = 5, M = 4, M' = 5, W = 4, W' = 2, P = 1$, and $B = 2$. Notice that the parameters indicate the lost of one WiFi packet since $M' - M = 1$.
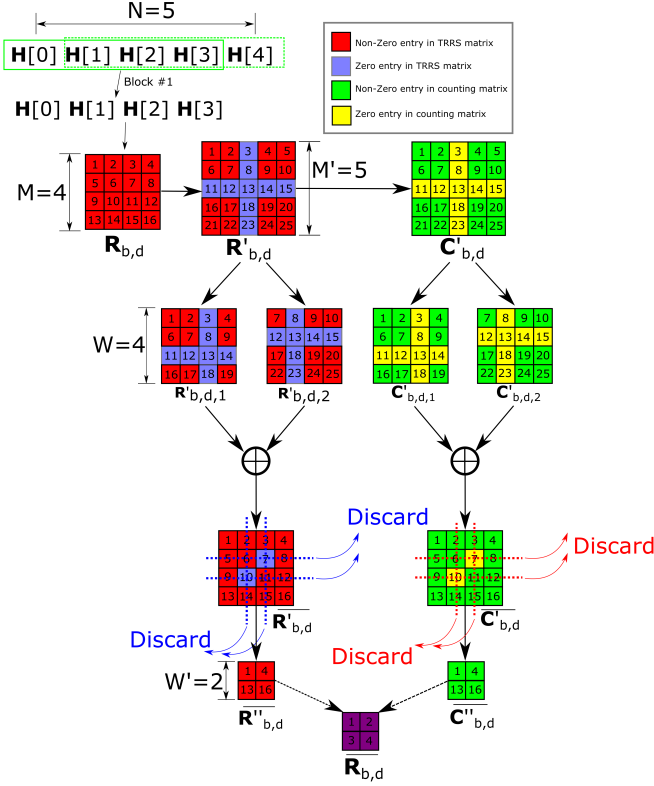
Figure 5.2: Procedure of TRRS matrix smoothing

5.1.4.3 Analysis via Root-MUSIC

The smoothed $W' \times W'$ TRRS matrix $\overline{\mathbf{R}_{b,d}}$ is analyzed via the Root-MUSIC algorithm. An eigenvalue decomposition (EVD) is invoked on $\overline{\mathbf{R}_{b,d}}$, leading to a $W' \times (W' - p)$ noise subspace matrix $\mathbf{U}'_n$ and thus $\mathbf{Q}' = \mathbf{U}'_n(\mathbf{U}'_n)^\dagger$. The polynomial is modified as

$$f(z) = \sum_{m=0}^{W'-1} \sum_{n=0}^{W'-1} [\mathbf{Q}']_{m,n} z^{g_{m,n}} \ . \tag{5.6}$$

where $g_{m,n} = m - n$ if packet loss is not considered, and $g_{m,n} = s''_m - s''_n$ otherwise. Here, p should be set to the maximum possible number of people, e.g., the capacity of a room. When the polynomial in (5.6) cannot produce results in the range $[b_{\min}, b_{\max}]$, we call $f(z) = 0$ insolvable and put an empty solution into a set $\mathcal{N}_{b,d}$. Otherwise, we save the breathing rate candidates $\{\hat{b}_1, \hat{b}_2, \cdots, \hat{b}_{p'}\}$ into a set denoted as $\mathcal{S}_{b,d}$, where p' is the number of candidates after filtering. After processing all D links, the sets $\{\mathcal{S}_{b,d}\}_{b=1,2,\cdots,B}^{d=1,2,\cdots,D}$ are combined together into $\mathcal{S}$ as $\cup_{d=1}^{D} \cup_{b=1}^{B} \mathcal{S}_{b,d}$ and $\mathcal{N}$ as $\cup_{d=1}^{D} \cup_{b=1}^{B} \mathcal{N}_{b,d}$, where $\cup$ denotes the *set union* operator.

5.1.5 Breathing Detection

Some of the breathing rate candidates generated by the breathing feature extraction might still be noisy estimations caused by interference and/or thermal noise in the CFRs. Therefore, we need to assess how likely these candidates are caused by interference and noise. If with high probability, these candidates have no correlation with human breathing, we determine that there is no people breathing. Otherwise, we conclude that breathing is present.

We observe from extensive experiments that: the statistics of the set $\mathcal{S}$ and set $\mathcal{N}$ are indicator functions of the presence of breathing. In the absence of breathing, it is more likely that the polynomial in (5.6) is insolvable, which yields a large $\mathcal{N}$ and a small $\mathcal{S}$ in terms of their cardinalities, i.e., number of unique set elements. On the contrary, when breathing exists, solving the polynomial in (5.6) would produce many breathing rate candidates, giving rise to a small $\mathcal{N}$ and a large $\mathcal{S}$. We leverage

this observation for breathing detection.

5.1.5.1 Calculating α and β

Firstly, we formulate two statistics α and β expressed as

$$\alpha = \frac{\#(\mathcal{N})}{\#(\mathcal{S}) + \#(\mathcal{N})} \ , \beta = \frac{\#(\mathcal{S})}{BDp} \ , \qquad (5.7)$$

where the denominator of β stands for the total number of possible breathing rate candidates with B blocks, D links, and p estimations per link per time window. $\#(\cdot)$ denotes the cardinality of a set. α indicates the *insolvability* of (5.6), while β indicates the *diversity* of (5.6). The correlation between (α, β) and the presence of breathing motivates us to develop a detection scheme based on the observed (α, β) values.

5.1.5.2 Automatic Label Learning

TR-BREATH can learn the labels y associated with each (α, β) obtained in the training phase automatically. Write $\boldsymbol{\theta} = (\alpha, \beta)$ for convenience, and by convention, y equals to $+1$ if the associated $\boldsymbol{\theta}$ is measured in the presence of breathing, and y equals to -1 otherwise.

During the training phase, TR-BREATH makes T observations of $\boldsymbol{\theta}$, written as $\{\boldsymbol{\theta}_i\}_{i=1,2,\cdots,T}$. Based on the observations, TR-BREATH extracts the labels $\{\hat{y}_i\}_{i=1,2,\cdots,T}$ using unsupervised label learning consisting of two phases:

1. Partition $\{\boldsymbol{\theta}_i\}_{i=1,2,\cdots,T}$ into 2 classes by invoking k-means clustering [41] with

$k = 2$. Denote the centroids of cluster 1 and 2 as $(\hat{\alpha}_1, \hat{\beta}_1)$ and $(\hat{\alpha}_2, \hat{\beta}_2)$, respectively.

2. If $\hat{\alpha}_1 > \hat{\alpha}_2$, label all members of cluster 1 with $\hat{y} = -1$ to indicate that they are observed in the absence of breathing. Then, label the members of cluster 2 with $\hat{y} = +1$. Similar procedure applies to the case of $\hat{\alpha}_1 < \hat{\alpha}_2$. In the rare case that $\hat{\alpha}_1 = \hat{\alpha}_2$, label the elements within the cluster with a larger $\hat{\beta}$ with $\hat{y} = +1$.

5.1.5.3   SVM Classification

Based on $\{\boldsymbol{\theta}_i\}_{i=1,2,\cdots,T}$ and $\{\hat{y}_i\}_{i=1,2,\cdots,T}$, we train a support vector machine (SVM) [17], a widely used classifier. Training of the SVM generates two weight factors denoted as ω_α and ω_β signifying the importance of α and β in breathing detection. Additionally, the training produces a bias term ω_b. ω_α and ω_β. After training of the SVM, given any $\boldsymbol{\theta} = (\alpha, \beta)$, TR-BREATH determines the existence of breathing when $\omega_\alpha \alpha + \omega_\beta \beta + \omega_b > 0$ and non-existent otherwise.

5.1.6   Breathing Rate Estimation

If breathing is detected, TR-BREATH proceeds by formulating multi-person breathing rate estimations.

5.1.6.1 Clustering by Affinity Propagation

The breathing rate candidates in $\mathcal{S}$ are fed into the affinity propagation algorithm [32]. It works by passing the responsibility message to decide which estimations are exemplars, and the availability message to determine the membership of an estimation to one of the clusters. Different from k-means [41], affinity propagation does not require the knowledge of the cluster number. Here, we assume that affinity propagation partitions the elements of $\mathcal{S}$ into U clusters.

5.1.6.2 Likelihood Assignment

For each cluster, TR-BREATH evaluates its population, variance, and centroid, expressed as p_i, v_i, and c_i. Then, p_i and v_i are normalized as $\bar{p}_i = p_i / \sum_{i=1}^{U} p_i$ and $\bar{v}_i = v_i / \sum_{i=1}^{U} v_i$. The likelihood of cluster i, denoted by l_i, is calculated as

$$
l_i = \begin{cases} 0, & (v_i = 0, p_i = 1), \text{or } \bar{p}_i < 2\% \\ \frac{e^{\omega_p \bar{p}_i - \omega_v \bar{v}_i - \omega_c c_i}}{\sum_{i=1}^{U} e^{\omega_p \bar{p}_i - \omega_v \bar{v}_i - \omega_c c_i}}, & \text{Otherwise} \end{cases}, \tag{5.8}
$$

where ω_p, ω_v, and ω_c are positive weighting factors to account for different scales of the corresponding terms. The likelihood assignment in (5.8) incorporates a term related to the cluster centroid c_i. The insight is that a high breathing rate is less likely than a low breathing rate in real life. Meanwhile, high breathing rate candidates are more likely to be caused by the harmonics of breathing rates. Also, (5.8) implies that singletons, i.e., clusters with a single element ($v_i = 0$ and $p_i = 1$), should be assigned with zero likelihoods. Clusters with $\bar{p}_i < 2\%$ are also considered as outliers and are eliminated.

5.1.6.3 Cluster Merging

Since the breathing rates are evaluated for each time window and for each link independently, it is likely that breathing rate estimations for the same person differ slightly in a small range. This results in several closely-spaced clusters, which should be merged to improve the performance.

To identify the clusters to be merged, we calculate the inter-cluster distances by calculating the differences in their centroids. Then, we merge clusters with inter-cluster distance falling below a threshold, known as the merging radius denoted by γ. For example, if $|c_i - c_{i+1}| < \gamma$, then, cluster i and $i+1$ would be merged. Denote the new cluster index as i', the normalized population of cluster i' is given by $\overline{p}_{i'} = \overline{p}_i + \overline{p}_{i+1}$ and the normalized variance $\overline{v}_{i'}$ is recalculated. The centroid of cluster i' is expressed as the weighted average of the merged two clusters, given by $c_{i'} = \frac{\bar{l}_i c_i + \bar{l}_{i+1} c_{i+1}}{\bar{l}_i + \bar{l}_{i+1}}$.

Finally, the likelihood of cluster i' is updated using (5.8). Merging of more than two clusters can be generalized from the aforementioned steps and is omitted here for brevity. The procedures for likelihood assignment and cluster merging are highlighted in Fig. 5.1.

Assuming a total of $\overline{K}$ clusters after merging and that the number of people K is known, TR-BREATH directly outputs $K_o = \min(\overline{K}, K)$ centroids with the highest likelihoods as the multi-person breathing rate estimations, i.e., $\hat{b}_i = c_{\text{idx}_i}$, $i = 1, 2, \cdots, K_o$ where idx_i stands for the index of the i-th largest likelihood.

5.1.7 Estimating the Number of People

Denote the set $\mathcal{J}$ as $\mathcal{J} = \{j \mid \sum_{i=1}^{\min(\overline{K},j)} \bar{l}_{\text{idx}_i} \geq \lambda\}$ where λ is a threshold. In other words, the set $\mathcal{J}$ contains the number of clusters with an accumulated likelihood exceeding λ. When the exact people number is unknown, given the knowledge of the maximum possible number of people, TR-BREATH formulates an estimation $\hat{K}(\lambda)$ given by the minimum element of $\mathcal{J}$ denoted as $\hat{K}(\lambda) = \min(\mathcal{J})$, i.e., the smallest j that satisfies $\sum_{i=1}^{\min(\overline{K},j)} \bar{l}_{\text{idx}_i} \geq \lambda$.
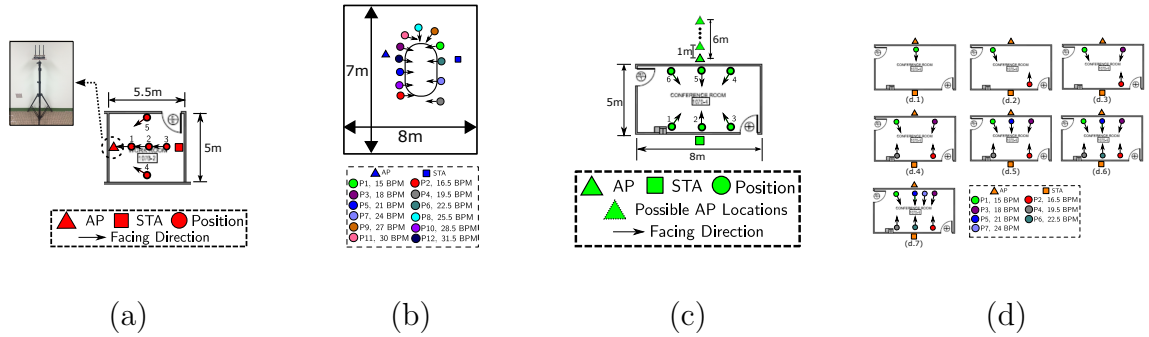

(a) (b) (c) (d)

Figure 5.3: Experiment settings: (a) single-person, LOS (b) multi-person, LOS (c) single-person, NLOS (d) multi-person, NLOS.

5.2 Experimental Results

In this section, we present the experimental results of TR-BREATH in different indoor environment.

5.2.1 Experimental Setups

5.2.1.1 Environment

We conduct extensive experiments to evaluate the performance of TR-BREATH. The experiments are conducted in three different rooms in an office suite with dimensions 5.5m×5m, 8m×7m, and 8m×5m, respectively.

5.2.1.2 Devices

We build one pair of prototypes equipped with off-the-shelf WiFi cards. Each prototype has 3 omni-directional antennas. Thus, the total number of links D is 9. One of the prototypes works as AP while the other works as the STA. The center frequency is configured as 5.765 GHz with a bandwidth of 40 MHz. The transmission power is 20 dBm or 100 milli-Watts. The set of usable subcarriers is given as $\{-58, -57, -56, \cdots, -2, 2, 3, \cdots, 56, 57, 58\}$ with $K = 114$.

5.2.1.3 Placement of WiFi devices

The performance is evaluated in both LOS and NLOS scenarios. For the LOS scenarios, the AP and STA are placed in the same room with people, while for the NLOS scenarios, they are placed outside the room blocked by two walls and have no direct line-of-sight path to the subject under monitoring. The locations of both WiFi devices are marked in Fig. 5.3.

5.2.1.4 Participants

A total of 17 different participants were invited for experiments. During the experiments, slight movements, e.g., head or limb movements, were allowed.

5.2.1.5 Parameter Settings

The following parameters are used unless otherwise stated:

- Each experiment lasts for 2 minutes.

- The signal subspace dimension p is configured as 10.

- The merging radius γ is set as 0.5 BPM.

- The range of interest of the breathing rate is from $b_{\min} = 10$ BPM to $b_{\max} = 50$ BPM. This covers the adult breathing rate at rest $(10 - 14$ BPM), infant breathing rate $(37$ BPM), and the breathing rate after workout [39, 43].

- The packet rate of WiFi transmission is 10 Hz[†].

- The sampling interval T_s is 0.1s where s stands for second. For notation convenience, we write the time duration of each block measured in seconds as $M_t = MT_s$ and the window size measured in seconds as $W_t = WT_s$. The overlap in terms of seconds between different blocks is $P_t = PT_s$. As default

---

[†]The 10Hz packet rate agrees with the *beaconing rate* of a commercial WiFi AP, and the packet size containing one CFR measurement is 2.5KB, resulting in a data rate of 25KB/s during CFR acquisition. Therefore, the proposed system only introduces minor interference to the co-existing WiFi networks on the same WiFi channel.

values, we adopt the parameters $M_t = 45\text{s}$, $W_t = 40.5\text{s}$, $P_t = 4.5\text{s}$, and $B = 5$ unless otherwise stated. The total time of CFR measurements T_{tot} is thus $M_t + (B - 1) \times P_t$ which equals to 63s.

During the experiments, we only observe $2 \sim 3$ WiFi networks sharing the same WiFi channel with the experimental devices. The packet loss rate is merely 1% for all experiments. The impact of packet loss can be safely ignored in this case. Therefore, (5.6) reduces to (5.2), and we use $g_{m,n} = m - n$ in (5.3). Also, M equals to M' as shown in Fig. 5.2.

5.2.1.6 Ground-Truths

The performance of TR-BREATH is evaluated by comparing the breathing rate estimations against the ground-truths. To obtain the ground-truths, we ask each participant to synchronize his/her breathing according to a metronome. After the controlled breathing experiments, we conduct experiments under a less controlled and thus more practical setting, where the participants are asked to breathe naturally and count their own breathing rates manually as baselines.

5.2.2 Metrics for Performance Evaluation

5.2.2.1 Breathing Detection Rate

The detection performance of the proposed system is directly linked to the SVM classification accuracy, which is evaluated by performing K-fold cross-validation on the trained SVM classifier.

5.2.2.2 Breathing Rate Estimation Accuracy

Assume that the people number P is known in advance with ground-truths given by $\mathbf{b} = [b_1, b_2, \cdots, b_P]$, and the proposed system outputs $K_o = \min(\overline{P}, P)$ estimations denoted as $\hat{\mathbf{b}} = [\hat{b}_1, \hat{b}_2, \cdots, \hat{b}_{\overline{P}}]$, the accuracy of estimation is calculated as

$$\text{Acc}[\mathbf{b}, \hat{\mathbf{b}}] = \left(1 - \frac{1}{K_o} \sum_{i=1}^{K_o} \left| \frac{\hat{b}_i - b_i}{b_i} \right| \right) \times 100\% . \tag{5.9}$$

For instance, the accuracy calculated from $\hat{\mathbf{b}} = [25.1, 29.8]$ BPM and $\mathbf{b} = [25, 30]$ BPM is 99.5%.

5.2.2.3 Average K_o

Still assuming that P is known and the monitoring system outputs $K_o = \min(\overline{P}, P)$ estimations. In this case, there is no penalty if $\overline{P} \geq P$ since the breathing rates estimations are given by the first K estimations with the highest likelihoods. On the other hand, when $\overline{P} < P$, the breathing rates associated with $P - \overline{P}$ people are missing in the estimations. Therefore, the average of K_o, denoted as $\overline{K_o}$, is also an important metric, as $\overline{K_o}$ closer to P indicates that most of the human breathing rates can be resolved by TR-BREATH.

5.2.2.4 Estimation Error of Number of People

When P is unknown, we formulate an estimation on the number of people P via $\hat{P}(\lambda)$, with the performance evaluated by the function $P(\lambda) = \text{E}(|P - \hat{P}(\lambda)|)$ and E stands for the expectation operator.
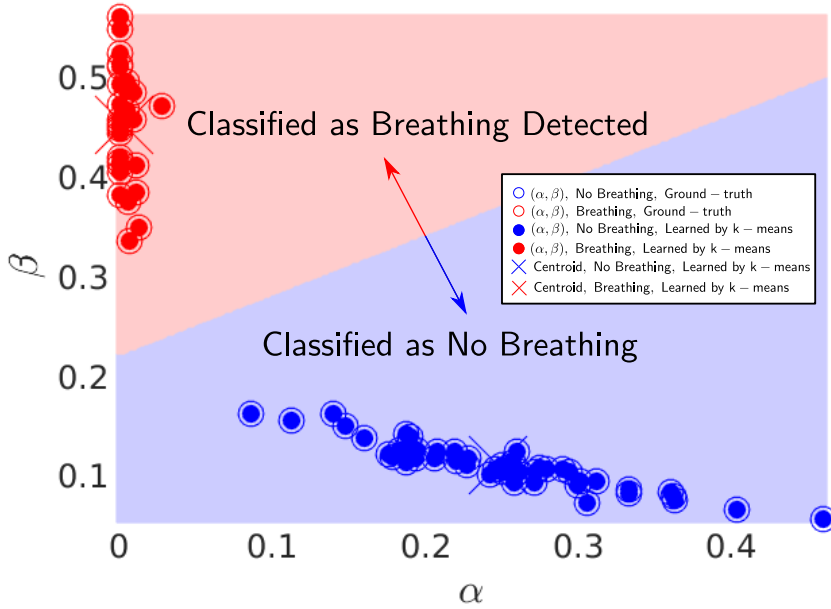
Figure 5.4: Classification performance for breathing detection.

5.2.3 Breathing Detection Performance

The proposed breathing detection scheme determines the existence of breathing based on the output of the SVM algorithm. We use 84 CFR measurements for evaluation, where 32 of them are collected in the presence of at least one person breathing, and 52 measurements are obtained without people breathing in the room. The devices are placed according to the NLOS setting shown in Fig. 3.4(c).

In Fig. 5.4, we demonstrate the breathing detection performance of the proposed system. First of all, we observe that the labels $\hat{y}$ can be inferred from (α, β) without errors. Secondly, we observe that SVM returns a hyperplane that partitions (α, β) perfectly, implying a 100% detection rate. This is further validated by performing K-fold cross-validation on the results, leading to a 100% accuracy for each cross-validation.

5.2.4 Performance of Breathing Rate Estimation

In this part, we evaluate the performance of the proposed system based on the ground-truth breathing rates using metronomes.

Figure 5.5: Accuracy with single-person breathing under the LOS scenario. $M_t = 45$s, $W_t = 40.5$s, $P_t = 4.5$s, $B = 5$, and $T_{tot} = 63$s.

5.2.4.1 Accuracy under Single-Person LOS Scenario

We ask one participant to sit at 5 positions as shown in Fig. 3.4(a) under the LOS scenario. For each position, the participant breathes at 15 BPM in synchronization to the metronome. After that, the participant switches the breathing rate to 17.5 BPM and later 20 BPM. The accuracy performances at the 5 positions with various breathing rates are depicted in Fig. 5.5. For comparison purpose, Fig. 5.5 also demonstrates the ground-truths. As can be seen from the figure, the proposed system can estimate the breathing rate with an accuracy of 99.56% averaging over

all cases. The worst case is when the participant sits at position 4 and breathes at 17.5 BPM with an accuracy of 98.58%, equivalent to an estimation error of ± 0.249 BPM.
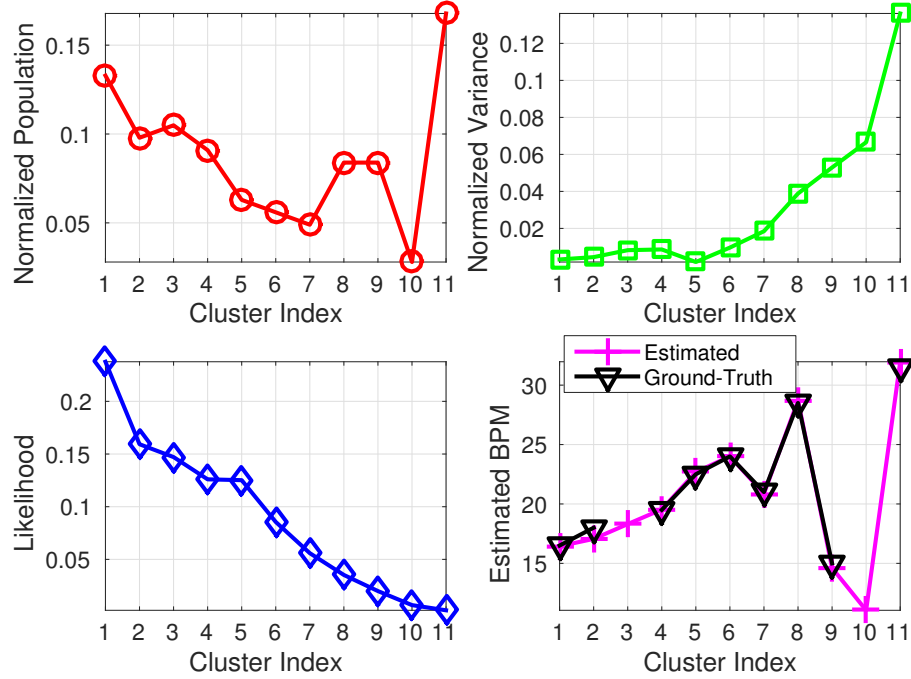
Figure 5.6: Performance of estimating breathing rates of a dozen people under the LOS scenario. $M_t = 45$s, $W_t = 40.5$s, $P_t = 4.5$s, $B = 5$, and $T_{tot} = 63$s.

5.2.4.2   Accuracy under Multi-Person LOS Scenario

A total of 12 people were invited into the conference room as shown in Fig. 3.4(b) under the LOS scenario. The details of the position and breathing rate for each participant are displayed in Fig. 3.4(b). The normalized population, variance, likelihood, and centroid for each cluster are presented in Fig. 5.6. It can be seen that the proposed system resolves the breathing rates of 9 out of a dozen people with an accuracy of 98.65%.
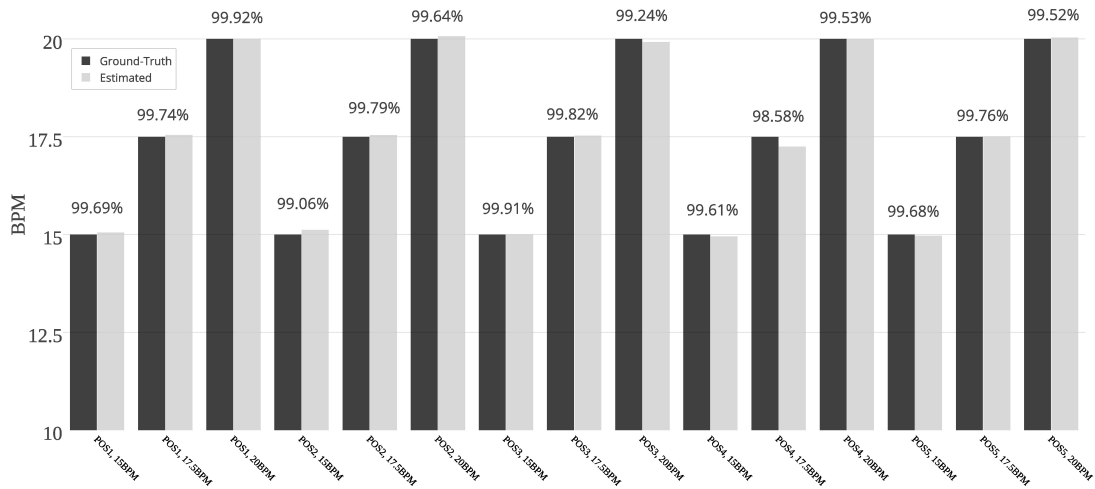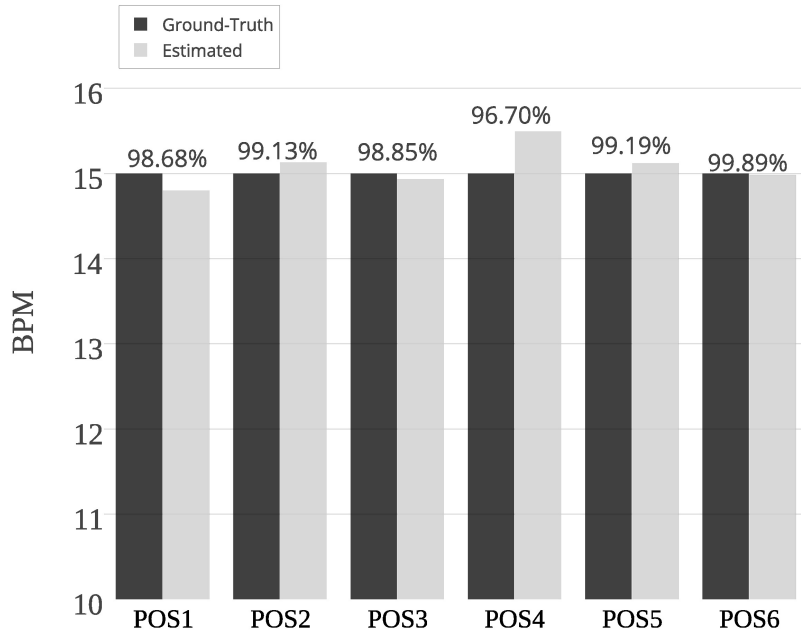
Figure 5.7: Accuracy with single-person breathing under the NLOS scenario. $M_t = 45$s, $W_t = 40.5$s, $P_t = 4.5$s, $B = 5$, and $T_{tot} = 63$s.
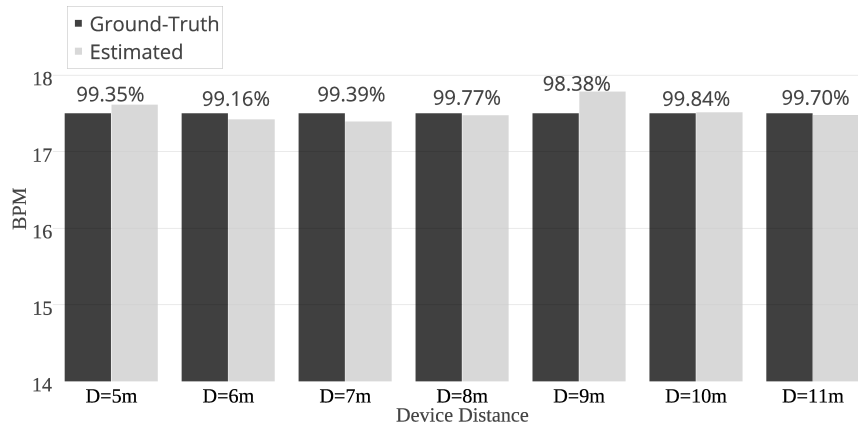
Figure 5.8: Accuracy of breathing rate estimation with various distances. $M_t = 45$s, $W_t = 40.5$s, $P_t = 4.5$s, $B = 5$, and $T_{tot} = 63$s.
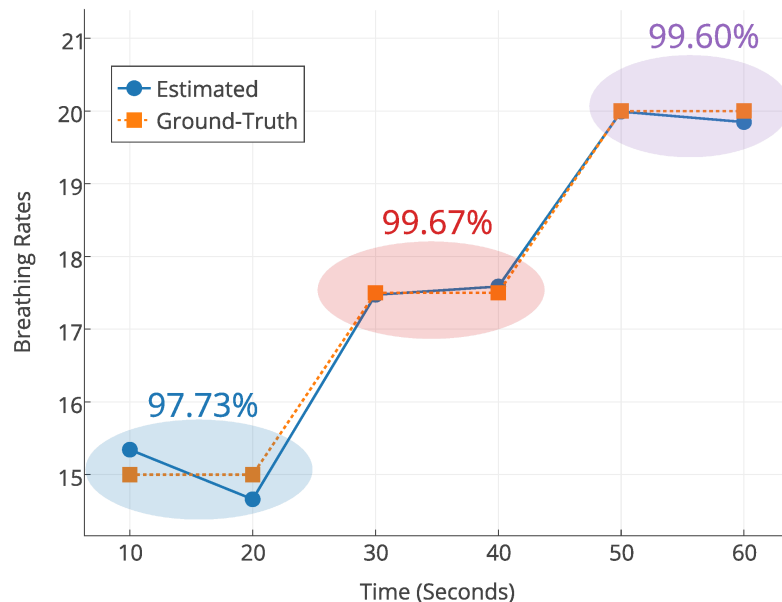
Figure 5.9: Accuracy of breathing rate estimation with 10 seconds of CFR measurement. $M_t = 10$s, $W_t = 9$s, $P_t = 0.5$s, $B = 1$, and $T_{tot} = 10$s.

5.2.4.3 Accuracy under Single-Person NLOS Scenario

One participant was invited into the conference room to breathe with 15 BPM at 6 different positions, with details shown in Fig. 3.4(c). Both WiFi devices are placed outside the conference room. Fig. 5.7 shows that a mean accuracy of 98.74% averaging over the 6 positions is achieved even when the two devices are blocked by two concrete walls of the conference room, which validates the high accuracy under the through-the-wall scenario.

To evaluate the impact of distances between WiFi devices on the performance, we place the AP at 6 different locations with 1 meter resolution. The participant breathes at 15 BPM in this experiment. The distance between the AP and the STA ranges from 5 meters to 11 meters. As shown in Fig. 5.8, the proposed scheme

achieves more than 98.38% in accuracy, with a mean accuracy of 99.37% averaging over the results of various distances. Even when the device distance reaches 11 meters, the accuracy is maintained at 99.70%, demonstrating the robustness of the proposed system under different device distances.

We further evaluate TR-BREATH by reducing M_t to 10s. Besides, we set $W_t = 9$s, $P_t = 0.5$s, and $T_{tot} = 10$s. The packet rate is increased to 30 Hz. One participant sits at position 1 of Fig. 3.4(c) and breathe at $15, 17.5, 20$ BPM, with each breathing rate lasting for 20 seconds. The total measurement time is 60 seconds. Fig. 5.9 shows that TR-BREATH could track the breathing rate accurately with a mean accuracy of 99%. Therefore, TR-BREATH can provide accurate breathing rates every 10 second for single-person breathing monitoring that fits well to the patient monitoring scenarios.

Figure 5.10: Accuracy with multiple people under the NLOS scenario. $M_t = 45$s, $W_t = 40.5$s, $P_t = 4.5$s, $B = 5$, and $T_{tot} = 63$s.

### 5.2.4.4 Accuracy under Multi-Person NLOS Scenario

We invite up to 7 people into one conference room with two devices placed under the NLOS scenario. The positions and breathing rates associated with each person are depicted in Fig. 3.4(d). Fig. 5.10 summarizes the accuracy performances, which shows that an accuracy of 99.1% when $K = 7$ and a mean accuracy of 97.3% averaging over all 7 cases can be achieved.

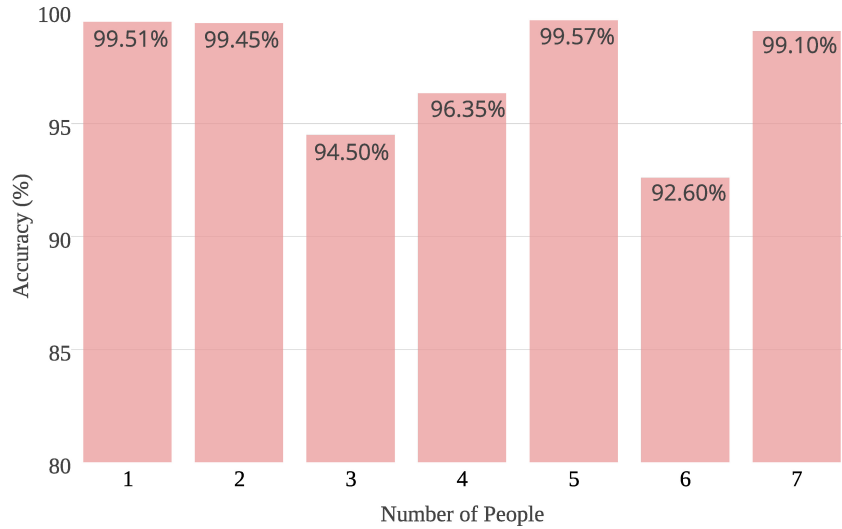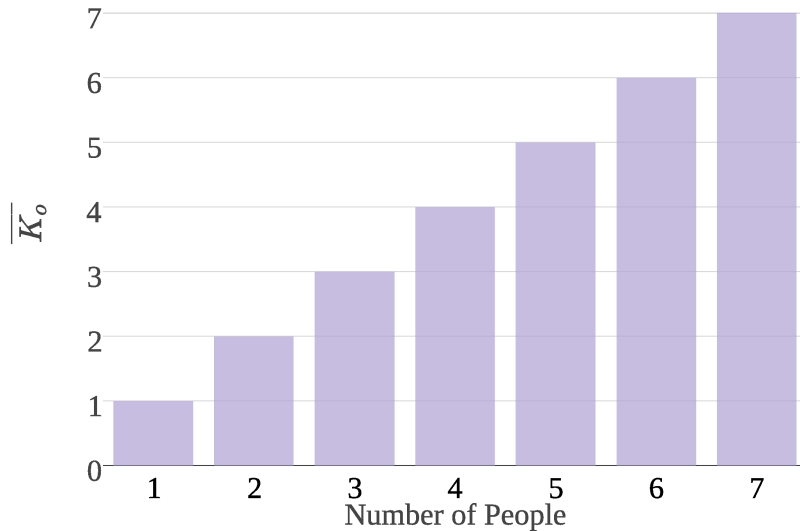Figure 5.11: $\overline{K_o}$ with multiple people under the NLOS scenario. $M_t = 45$s, $W_t = 40.5$s, $P_t = 4.5$s, $B = 5$, and $T_{tot} = 63$s.

5.2.4.5 $\overline{K_o}$ under Multi-Person NLOS Scenario

Fig. 5.11 demonstrates the $\overline{K_o}$ performance for the multi-person NLOS scenario. As we can see, with a various number of people P, $\overline{K_o}$ equals to P, which

shows that the proposed system could resolve the breathing rates of all people. Combining the results in Fig. 5.10, we conclude that given P people, the proposed system resolves the breathing rates of P people with high accuracy.

Figure 5.12: Performance of estimating the natural breathing rates of one person under the NLOS scenario. $M_t = 45s$, $W_t = 40.5$s, $P_t = 4.5$s, $T_{tot} = 63$s.

5.2.5   Performance of Natural Breathing Rate Estimation

In this part, we investigate the performance of the proposed system in a more practical setting by asking the participants to breathe naturally. Instead of using the metronomes, the participants were asked to memorize how many breaths they took in a minute.

5.2.5.1   Accuracy under Single-Person NLOS Scenario

One participant is asked to breathe naturally at 4 different positions in the same conference room as in Fig. 3.4(c). Then, the participant lies on the ground and breathe. Fig. 5.12 shows that a mean accuracy of 97.0% can be achieved. Moreover,
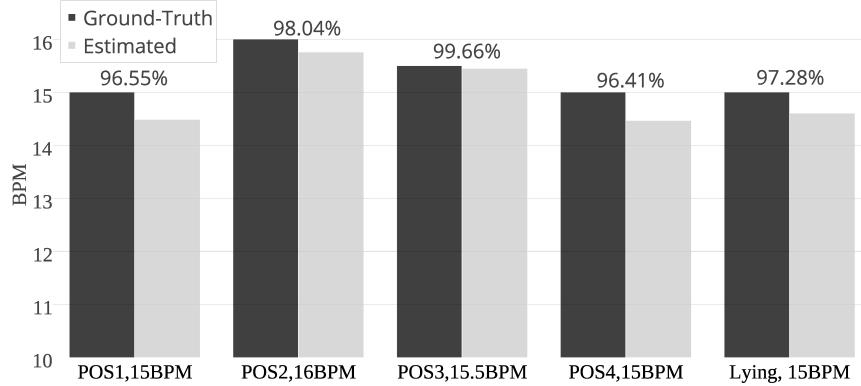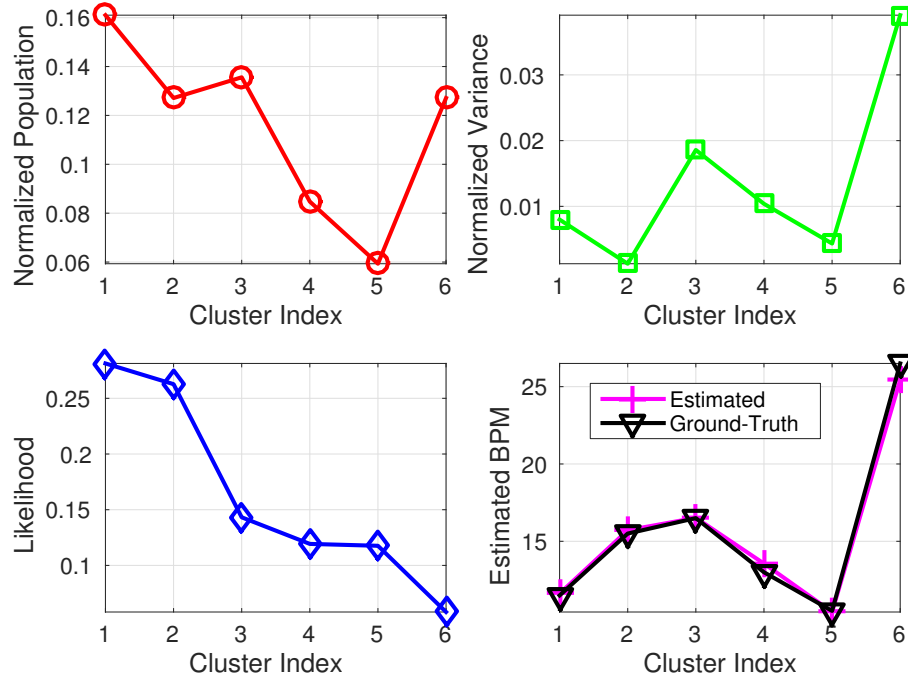
Figure 5.13: Performance of estimating the natural breathing rates of 9 people under the NLOS scenario. $M_t = 45s$, $W_t = 40.5$s, $P_t = 4.5$s, $T_{tot} = 63$s.

the breathing rate of a person lying on the ground can be estimated accurately, which shows the viability of the proposed scheme in monitoring the breathing rate of a sleeping person.

5.2.5.2 Accuracy under Multi-Person NLOS Scenario

Nine participants breathe naturally in the conference room shown in Fig. 3.4(c). The breathing rates are given as $[16, 11.5, 10.5, 12, 13, 15.5, 16.5, 26.5, 12]$ BPM, where two participants coincide in their breathing rates. Fig. 5.13 shows that 6 out of the 8 resolvable breathing rates are obtained with an accuracy of 98.07%.
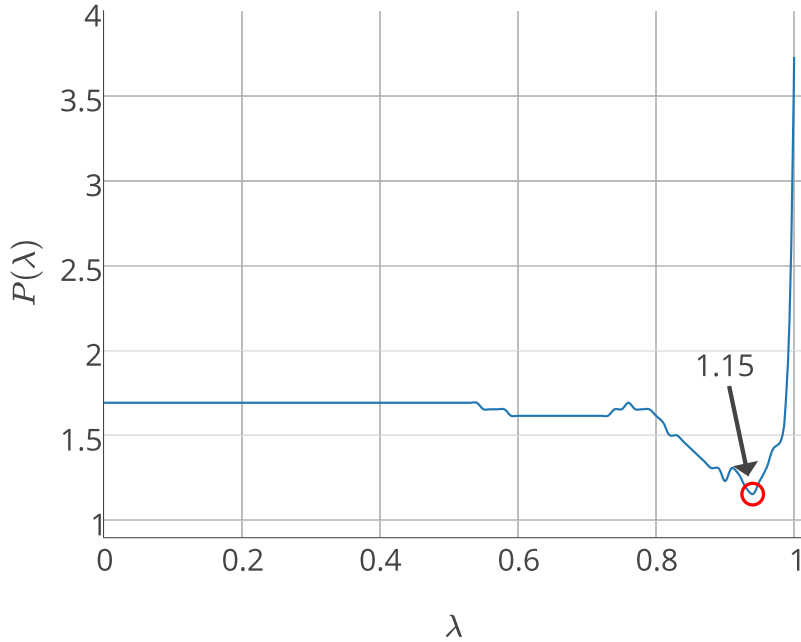
Figure 5.14: Performance of people number estimation. $M_t = 45$s, $W_t = 40.5$s, $P_t = 4.5$s, $B = 5$, and $T_{tot} = 63$s.

5.2.6 Estimating the Number of People P

Fig. 5.14 illustrates that the optimal $P(\lambda)$ is 1.15 when $\lambda = 0.88$. Thus, the proposed system can estimate the number of people with an error around 1.

5.3 Impact of Various Factors

In this section, we further investigate the performance of TR-BREATH in a more practical application scenario. First of all, we study the performance under the influence of packet loss with various severity. Then, we discuss the effects of motions on TR-BREATH. Finally, we demonstrate the significant improvement of TR-BREATH using both amplitude and phase information compared to the ap-

proach using amplitude only in [40]. The parameters are configured to be the same as Section 5.2.1.5 unless otherwise stated.

5.3.1 Impact of Packet Loss

We present the accuracy under the NLOS single-person at position 1 shown in Fig. 5.3(c) with different packet loss rate. We consider two packet loss mechanism, i.e., burst packet loss and random packet loss. The burst packet loss is mainly caused by the continuous data transmission among few WiFi devices which fully jams the medium for a long time. On the other hand, the random packet loss is due to the random access of a large number of nearby WiFi devices which occupy the medium occasionally.

To emulate packet loss, we intentionally discard collected CFR samples in the experiments. More specifically, for the burst packet loss, we discard CFR samples within a certain time period, while for the random packet loss, we discard CFR samples with index following a uniform distribution. When the packet loss compensation is enabled, $g_{m,n} = s''_m - s''_n$ is used, otherwise $g_{m,n} = m - n$.

The results with different packet loss rate with the aforementioned two mechanisms are shown in Fig. 5.15. We observe that the consequence of random packet loss is much more severe than the burst packet loss when the packet loss compensation is not enabled. With 10% random packet loss, the accuracy drops to 88.35% from 99.35%. The accuracy further deteriorates to 74.13% and 62.83% with 20% and 30% packet loss, respectively. The advantage of packet loss compensation is

obvious since TR-BREATH maintains an accuracy of 99.70% even with 30% packet loss. On the contrary, burst packet loss does not degrade the accuracy greatly. It can be justified by the fact that most CFRs are still sampled uniformly under this scenario.
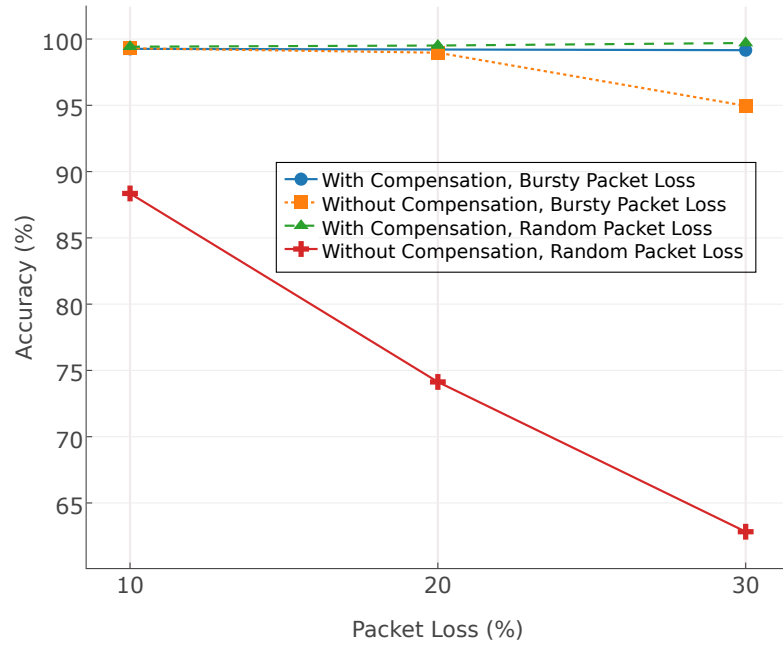
Figure 5.15: Impact of packet loss on accuracy

5.3.2 Impact of Motion

To study the effect of motion, we perform additional experiments involving ambient motions and subject motions. The experiment settings are shown in Fig. 5.16. The participant breathes at 20 BPM.
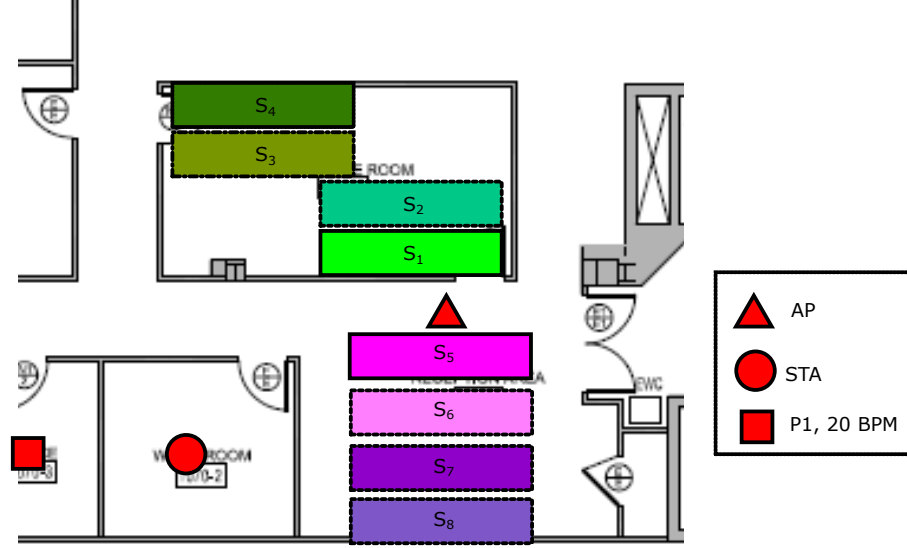
Figure 5.16: Experiment settings for investigation of ambient motions and subject motions

5.3.2.1 Impact of Ambient Motion

Besides the participant under breathing monitoring, we ask another participant to walk randomly in the eight highlighted areas in Fig. 5.16, where S_1 to S_4 stands for the ambient motions in the conference room and S_5 to S_8 in the foyer. We further classify these areas in terms of their distances to the WiFi AP as very close, close, far, and very far. For instance, S_1 is considered to be very close from the WiFi AP, while S_4 is regarded as very far away from the WiFi AP. Despite that the impact of motion is location-dependent, in general, we find that the motions introduce severe interference into TR-BREATH when they occur within 1m radius to either the AP or the STA.

The results are depicted in Fig. 5.17. Clearly, when the ambient motion occurs very close to the WiFi AP, the accuracy degrades significantly, especially for the case

of ambient motions in the foyer area indicated by S_5. When the distance between the motion to the WiFi AP increases, the accuracy is improved. We observe similar results when the ambient motion occurs close to the WiFi device. Thus, we conclude that TR-BREATH can tolerate ambient motions as long as both WiFi devices of TR-BREATH are far from these motions.
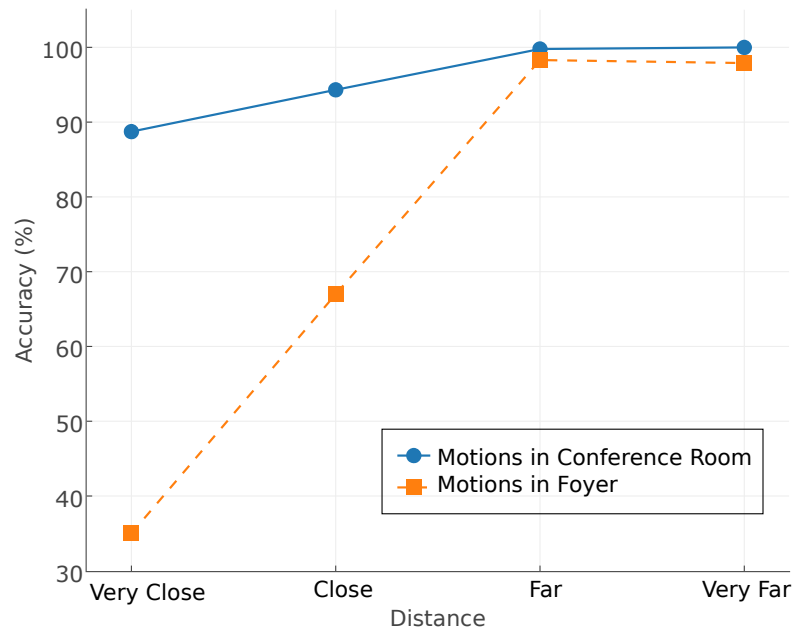
Figure 5.17: Impact of ambient motion on accuracy

5.3.2.2 Impact of Subject Motion

In this experiment, we ask the participant under monitoring to move randomly for a certain period of time, and then sit back to the original position as shown in Fig. 5.16 to continue breathing. The results are shown in Fig. 5.18. We observe that when the participant only moves for 10 seconds, the accuracy can be maintained at

95.96%. The accuracy drops to 87.61% when the participant moves for 40 seconds, corresponding to an error of ± 2.48 BPM. This demonstrates that TR-BREATH can tolerate the subject motions given that the participant stays still during most of the time.
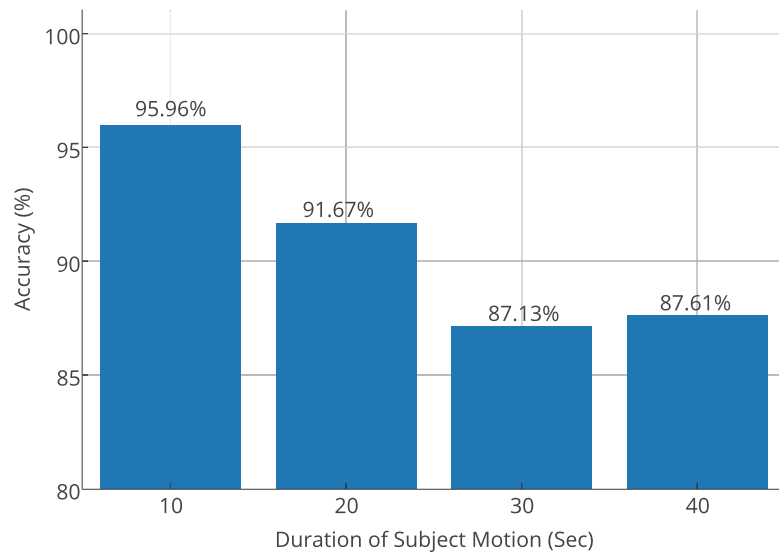
Figure 5.18: Impact of subject motion on accuracy

5.4 Summary

In this chapter, we have presented TR-BREATH, a contact-free and highly accurate breathing monitoring system leveraging TR for breathing detection and multi-person breathing rate estimations using commercial WiFi devices. The TR resonating strengths are analyzed by the Root-MUSIC algorithm to extract features for breathing detection and breathing rate estimation. Experiment results in a typical indoor environment demonstrate that, with 63 seconds of measurements,

a perfect detection rate can be obtained. Meanwhile, the proposed system can estimate the single-person breathing rate in the NLOS scenario with an accuracy of 99% with only 10 seconds of measurement. With 63 seconds of measurement, the proposed system achieves a mean accuracy of 98.65% for a dozen people under the LOS scenario and 98.07% for 9 people under the NLOS scenario even when the two WiFi devices are blocked by two walls. The proposed system can also estimate the number of people with an average error around 1. We also show that TR-BREATH is robust against packet loss and motions in the environment. With the ubiquity of WiFi-enabled mobile devices, TR-BREATH can provide real-time, in-home, and non-invasive breathing monitoring in future medical applications.

Chapter 6

Robust Vital Sign Tracking

In Chapter 5, we have presented a highly accurate scheme utilizing the TR technique to characterize the periodic changes of breathing. It uses Root-MUSIC as the spectral analysis tool and machine learning techniques to resolve the breathing rates of multiple people. Two issues with the high accuracy method proposed in Chapter 5 are

- Root-MUSIC is a high computational complexity algorithm that requires the calculation of EVD in each time window. The addition of machine learning techniques further increases the burden of computations and limits the scalability of TR-BREATH.

- Since Root-MUSIC requires prior knowledge of the signal subspace dimension, it is not robust against random environmental perturbations caused by the subjects under monitoring and people moving near the subjects; these motions could change the signal subspace dimension.

Due to the aforementioned issues, Root-MUSIC-based scheme is computational intensive and is more suitable for circumstances requiring highly accurate breathing monitoring in a relatively static environment. In light of this, in this chapter, we consider the algorithmic complexity and robustness as first class citizens. More

specifically, we present a robust scheme that utilizes FFT for spectral analysis using CFRs obtained from off-the-shelf WiFi devices. The proposed scheme leverages finite state machine (FSM) to counteract the motion of the subject or from other subjects to facilitate breathing tracking. The integration of FFT and FSM lead to a scalable, low-complexity, and very robust scheme for breathing tracking *.

6.1 Algorithm

The proposed breathing tracking scheme starts by collecting CFRs on off-the-shelf WiFi devices. Considering the phase distortions as introduced in Chapter 2, the proposed system cleans the CFR phases by employing the linear regression presented in [52]. Realizing that the energy of breathing signals are concentrated on the first few CIR taps, we then transform the CFR from frequency domain to the time domain CIR by a inverse fast Fourier Transform (IFFT), leading to K' CIR taps. Realizing that the human breathing rates are confined in a finite range, say, f_1 to f_2, we design a bandpass filter with passband from f_1 to f_2 and apply the bandpass filter onto the CIRs for each CIR tap. In Fig. 6.1, we show the magnitude and phase response of the proposed bandpass filter with $f_1 = 0.133$ Hz and $f_2 = 0.7$ Hz corresponding to the breathing rates of 8 BPM to 42 BPM.

After that, we perform spectral analysis on each CIR tap with FFT. Here, we write the spectrum on CIR tap k and frequency component u as $F_k[u]$, where

---

*Given N CFRs, the complexity of Root-MUSIC-based scheme is on the order of N^3, while the complexity of FFT-based scheme is on the order of $N \log_2 N$. For instance, when $N = 512$, the FFT-based scheme is $29,127$ times faster than the Root-MUSIC based scheme.
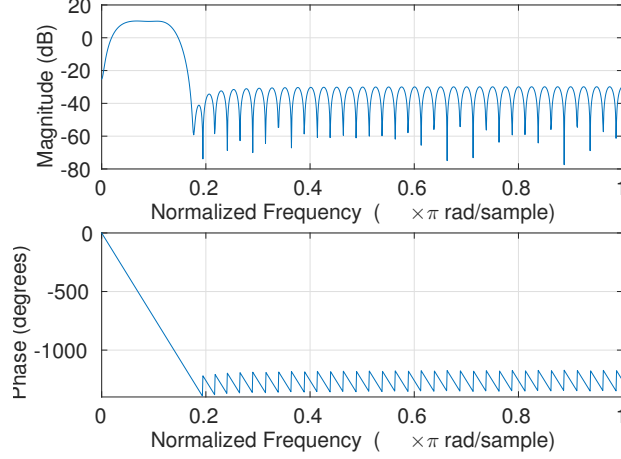
Figure 6.1: Filter coefficients for the passband 0.133 Hz to 0.7 Hz with 10 Hz CFR sampling rate. Filter length is 81.

$u \in [-N''/2, N''/2]$ where N'' is the size of FFT for spectral analysis. We sample the spectrum components from u_1 to u_2 and calculate the energy of each frequency bin written as $\{F_k[u]\}_{u=u_1,u_1+\Delta f,\cdots,u_2}$ where Δf is the frequency resolution and $u_1 = \lceil \frac{f_1}{\Delta f} \rceil$ and $u_2 = \lceil \frac{f_2}{\Delta f} \rceil$.

Assembling the spectrum on all CIR taps together leads to the matrix $\mathbf{F}$ such that

$$\mathbf{F} = \begin{bmatrix} \overline{F}_{-K'/2}[u_1] & \overline{F}_{-K'/2}[u_1 + \Delta f] & \cdots & \overline{F}_{-K'/2}[u_2] \\ \overline{F}_{-K'/2+1}[u_1] & \overline{F}_{-K'/2+1}[u_1 + \Delta f] & \cdots & \overline{F}_{-K'/2+1}[u_2] \\ \ldots & \ldots & \ldots & \ldots \\ \overline{F}_{K'/2-1}[u_1] & \overline{F}_{K'/2-1}[u_1 + \Delta f] & \cdots & \overline{F}_{K'/2-1}[u_2] \\ \overline{F}_{K'/2}[u_1] & \overline{F}_{K'/2}[u_1 + \Delta f] & \cdots & \overline{F}_{K'/2}[u_2] \end{bmatrix} \tag{6.1}$$

In Fig. 6.2, we show an example of matrix $\mathbf{F}$ on a specific link in linear scale, with the ground-truth breathing rate as 12.5 BPM. We can observe strong spectral components around 12.5 BPM on multiple CIR taps, especially the CIR taps with

114

index -5 to 5. This is intuitive since the energy of the breathing signal concentrates in the first few CIR taps.

Realizing that the breathing signal energy concentrates in the first few CIR taps as indicated by Fig. 6.2, we then take average over the spectrum for $k = 0, 2, \cdots, S - 1$ where $S \leq K'$ is the stripe width. The resultant averaged spectrum is then given as

$$\overline{F}[u] = \frac{1}{S} \sum_{k=0}^{S-1} F_k[u], \ u \in [u_1, u_2] \tag{6.2}$$
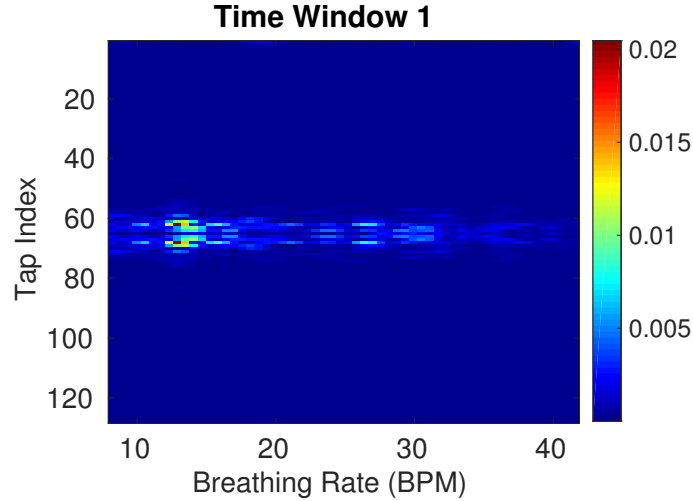
Figure 6.2: 2-D spectrum of the breathing signal over all CIR taps on one antenna link in one time window.

In a MIMO system, there are multiple antennas on either or both ends of the transmitter and receiver which gives rise to diversity in wireless communication. In the proposed scheme, we also harness the CFRs from multiple antenna links to improve the overall performance of breathing tracking. For each antenna link m out of a total of M links, we calculate the energy spectrum denoted by $\overline{F}_m[u]$, followed by computing the averaged energy spectrum over the available antenna links given

as

$$\dot{F}[u] = \frac{1}{M} \sum_{m=1}^{M} \overline{F}_m[u], \ u \in \{u_1, u_2\} \ . \qquad (6.3)$$

For the convenience of further processing, we transform the linear scale energy spectrum into its dB scale counterpart as

$$\dot{F}_{dB}[u] = 10 \log_{10} \dot{F}[u] \qquad (6.4)$$

In Fig. 6.3, we show several snapshots of the link averaged spectrum obtained from the same dataset that produces Fig. 6.2. Despite the temporal variations of the spectrum, we can always observe a strong spectral peak around the ground-truth breathing rate 12.5 BPM.

Figure 6.3: Spectrum after performing link average.

The peaks in the energy spectrum $\dot{F}_{dB}[u]$ lead to the breathing rate estimations. To extract these peaks, we leverage the persistence-based approach presented in [3] to obtain multiple pairs of local maxim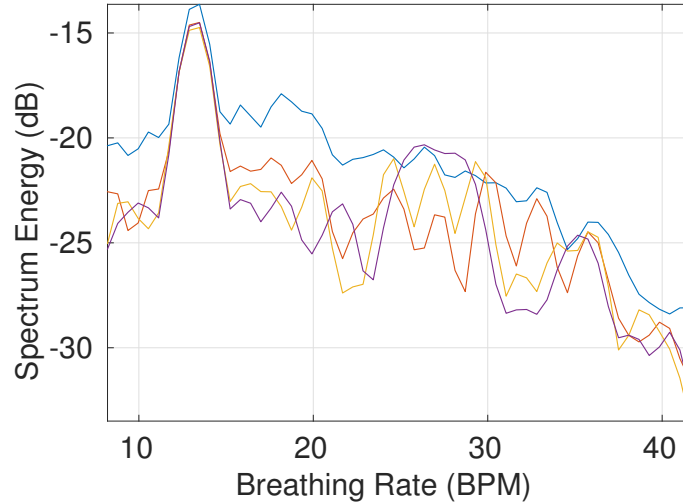als and local minimals. For the i-th pair of local maximum $p_{\max}[i]$ and minimum $p_{\min}[i]$, we evaluate their difference as

$v_i = p_{\max}[i] - p_{\min}[i]$, which translates into the signal-to-noise ratio (SNR) for the i-th peak.

Assuming a total of U' peaks remaining after the previous step and P breathing rates to be detected, we pick the top P out of U' peaks and use the corresponding peak locations $\{\hat{f}_i\}_{i=1,2,\cdots,U'}$ measured in Hz as the breathing rate estimations for P people. The breathing rate estimations with BPM as the unit are then given as $\{\hat{b}_i\}_{i=1,2,\cdots,U'}$ with $\hat{b}_i = 60\hat{f}_i$.

The proposed tracking system keeps updating the breathing rate estimations from time to time. Here, we define another two parameters: window size C_{window} and shift size C_{shift}, both measured in number of samples. The first set of breathing rate estimations are generated by performing spectral analysis on CFRs with sample index $[0, C_{window} - 1]$, and the second set of breathing rate estimations are generated by the same procedure on CFRs with sample index $[C_{shift}, C_{window} + C_{shift} - 1]$; the overlap between the two adjacent windows is then given as $C_{window} - C_{shift}$. A smaller C_{shift} leads to a more prompt real-time updating rate.

6.2 Enhancing Breathing Monitoring using Finite-State-Machine to Combat Motion Interferences

In a realistic environmental setting, there always exists motions from other people and/or objects, which introduces motion interference to the breathing tracking system. At the same time, motions of the subject under monitoring also inject interference. Both types of interference would significantly deteriorate the perfor-

mance of breathing tracking.

In light of this issue, we supplement the proposed system with a finite-state-machine (FSM) composed of several states into the proposed system so that the proposed system could automatically tune its parameters such as peak detection thresholds under different states. In this work, there are four different states in the FSM which are illustrated below, namely, Initialization, Verification, PeakFound, and Motion. For convenience, we show the transitions under the single-person breathing tracking case. Details of each state are given as follows.

1. The Initialization state is the default state. In this state, the breathing tracking system keeps searching for a peak in the range $[u_1, u_2]$. In detection of motion, it switches to the motion state. On the other hand, when it detects a significant peak, it switches to the Verification state. It would also tune the frequency of interest from $[u_1, u_2]$ to $[u'_1, u'_2]$.

2. The Verification state indicates that a peak has been detected and needs to be verified for the next few time slots. In case that the same peak has been detected for a number of times, the FSM switches to the PeakFound state. Otherwise, it stays in the Verification state. Meanwhile, it switches back to the Initialization state in case that no peak can be detected, and to the Motion state if motion is detected.

3. The PeakFound state stands for the state in which the breathing tracking system can detect a very stable breathing rate. In case that motion is detected, it switches to the Motion state. When the peak is no longer detectable, it

118

switches to the Initialization state. Otherwise, the FSM stays at the Peak-Found state.

4. The Motion state indicates that major motions have been detected and no credible breathing rate estimation can be made so far.

An illustration of these four states are presented in Fig. 6.4.

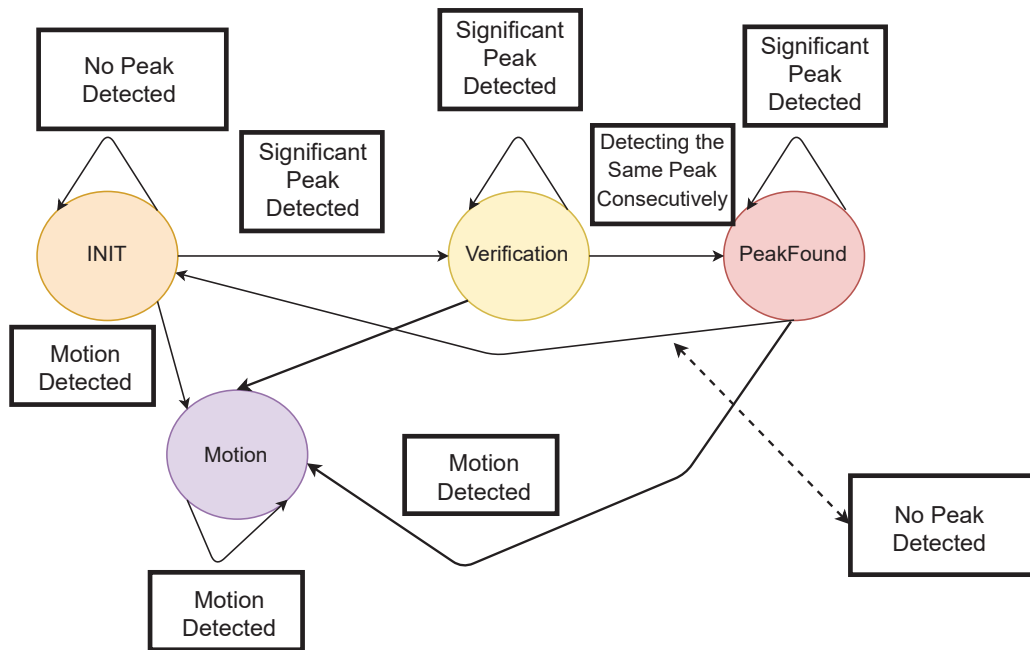

Figure 6.4: Illustration of FSM for single-person breathing tracking.

6.3 Multi-person Finite-State-Machine for Breathing Monitoring

In Section 6.2, we introduce the idea of FSM to overcome the motion inter-ference issue under single-person case, which can be extended to the multi-person case by running multiple FSMs in parallel, with each FSM captures the status of one specific person.

The FSMs associated with different people interact with each other, i.e., they are not independent. To make the FSMs more predictable, we define the following rules:

1. FSMs operating first would always select the strongest peak in its frequency range. For example, the i-th FSM, denoted as $FSM(i)$, selects the strongest peak in its search range $[u'_{1,i}, u'_{2,i}]$, where $[u'_{1,i}, u'_{2,i}]$ is the breathing range of interest for the i-th FSM.

2. To avoid duplication of breathing rate estimations, no two FSMs can pick the same peak in each time window. For example, if $FSM(i)$ selects peak at location $\hat{f}_i$, then $FSM(j)$, $j > i$ would look for other peaks not located at $\hat{f}_i$.

6.4 Experimental Results

To show the performance of the proposed scheme, we collect extensive experimental data in an office environment.

6.4.1 Parameter Settings

The experimental settings are demonstrated in Fig. 6.5. The adopted parameters are given in Table 6.1.

6.4.2 Environment

We perform the experiments in the same indoor environment as shown in Section 5.2 of Chapter 5. The experimental settings are shown in Fig. 6.5.

Table 6.1: Parameter settings for FFT-based breathing tracking with FSM

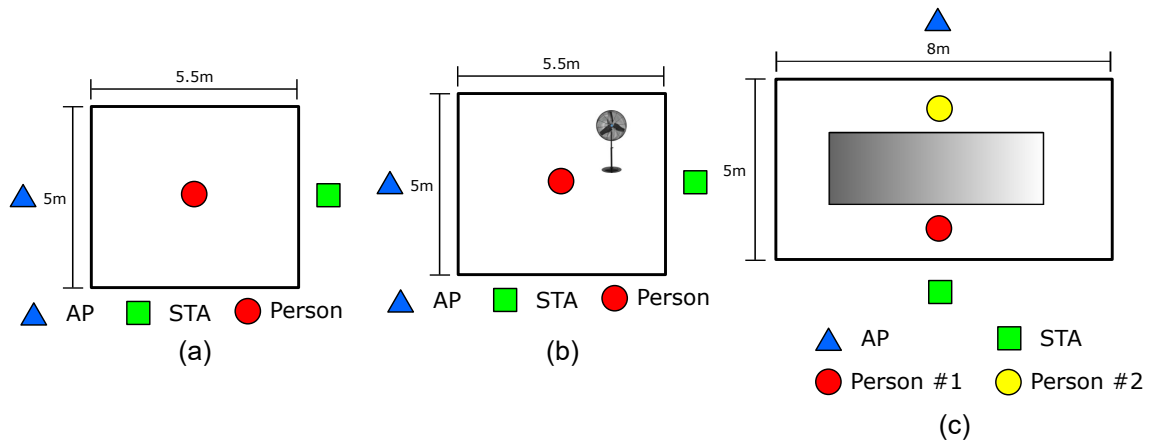| Parameter	Notation	Value
CFR Sampling Interval	T_s	100ms
Usable subcarrier size	K	114
IFFT size	K'	128
FFT size	N''	512
Bandpass filter length	H	81
Spectrum range of interest	$[f_1, f_2]$	$[0.133\text{Hz}, 0.7\text{Hz}]$
CFR window size	C_{window}	300 samples
CFR shift size	C_{shift}	50 samples

Figure 6.5: Floorplan of experiments (a) single-person, NLOS (b) single-person, NLOS, with a fan running (c) two-person, NLOS (d) three-person, NLOS.

6.4.3 Device

We use the same set of commercial WiFi devices shown in Section 5.2 of Chapter 5.

6.4.4 Results

6.4.4.1 Single-Person NLOS

We evaluate the performance of the proposed scheme for single-person NLOS breathing tracking. A total of 5 experiments have been conducted, with each experiment lasting for 2 minutes. The experimental setting is shown in Fig. 6.5(a). The ground-truths are given as $[12.5, 15, 17.5, 20, 22.5]$ BPM with an increment of 2.5 BPM. The results are shown in Fig. 6.6. As we can see, when the ground-truths are $[12.5, 15, 17.5]$ BPM, the differences between schemes with FSM and without FSM are negligible. However, when the breathing rates increase to 20 and 22.5 BPM, the FSM-based scheme outperforms the sheme without FSM. This is mainly due to the fact that when a person breathes faster, his/her breathing rate is not as stable as when he/she breathes slower, which introduces variations into the breathing signal strength and can be dealt with using FSM. The accuracy performances with FSM are given as $[97.65\%, 94.53\%, 92.86\%, 94.53\%, 93.88\%]$ respectively.

6.4.4.2 Single-Person NLOS with an Operating Fan

In this experiment, we turn on a electronic fan inside the same room with the subject under monitoring. Since the fan is an electronic device with metal cover,
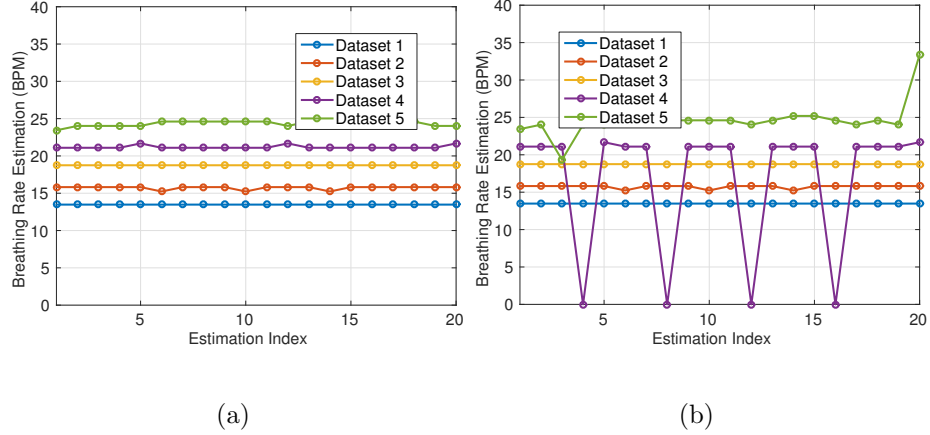
Figure 6.6: Results of breathing tracking for single-person NLOS scenario (a) with FSM (b) without FSM.

it would reflect some EM waves and thus introduce interference to the CFRs and degrde the breathing tracking performance. The setting is shown in Fig. 6.5(b). Fig. 6.7 compares the scheme with and without FSM. A breathing rate estimation of 0 indicates that the system is unable to obtain a reliable breathing rate. Although using FSM does not fully recover the ground-truth breathing rate (15 BPM), the utilization of FSM still enhances the overall performance. The accuracy with FSM is 94.48%.

In Fig. 6.8, we compare the CDFs of the breathing rate as defined in (5.9). Again, it shows the advantages of using FSM, implying by that the CDF with FSM is more steep than the one without FSM.

In Fig. 6.9, we demonstrate the state transition of the FSM-based scheme in this experiment. Different states shown in Fig. 6.4 are encoded as follows: Initialization $\rightarrow$ 0, Verification $\rightarrow$ 1, PeakFound $\rightarrow$ 2, Motion $\rightarrow$ 3. Fig. 6.9 shows that the FSM correctly reacts to the fan moving by switching to the Motion state from
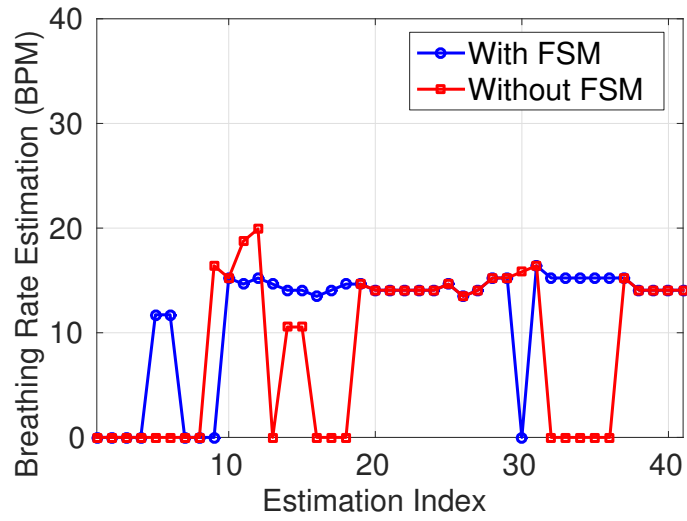
Figure 6.7: Comparison between the schemes with / without FSM with a fan running.
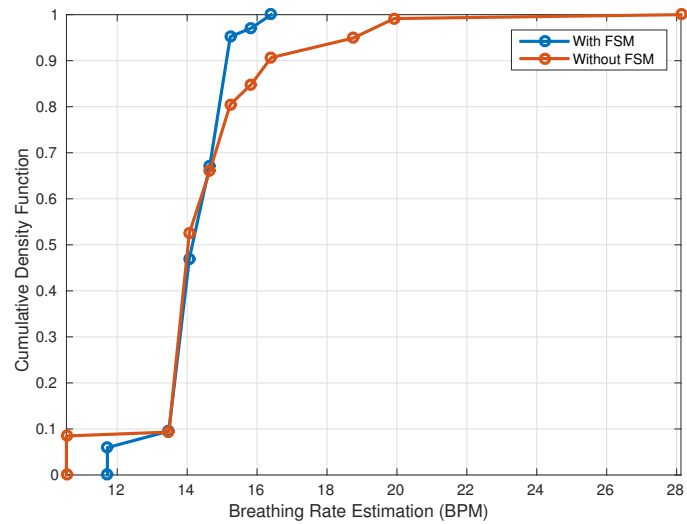
Figure 6.8: CDF performance with operating fan under single-person NLOS scenario with 18 BPM breathing rate.

time to time.
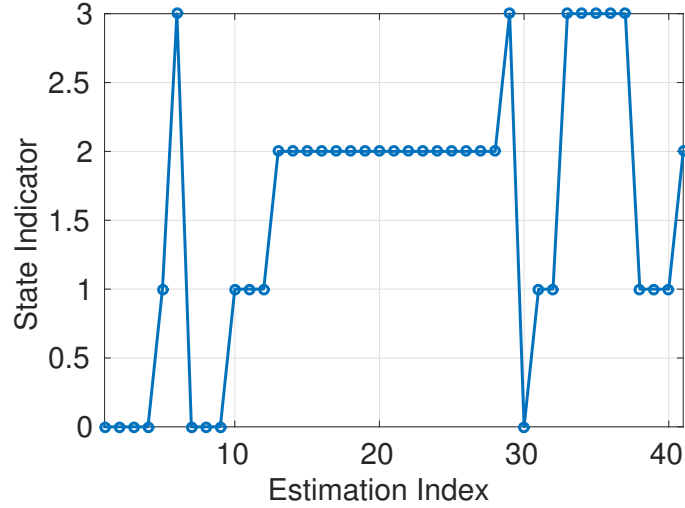
Figure 6.9: State transition of the FSM scheme with operating fan.

We conduct another experiment under the same setting except a breathing rate of 20 BPM with results shown in Fig. 6.10. Again, using FSM enhances the performance indicated by the more concentrated breathing rate estimations. The accuracy is given as 94.53%.

6.4.4.3 Multi-person Breathing Monitoring Performance

We use the settings shown in Fig. 6.5(c) and Fig. 6.5(d) for performance evaluation of multi-person breathing tracking.

Firstly, we study the performances of two-person breathing. The ground-truths are given as [15, 16.5] BPM. The breathing rate estimations with $C_{window} = 300$, $C_{window} = 450$, and $C_{window} = 600$ with FSM are shown in Fig. 6.11(a), Fig. 6.11(b), and Fig. 6.11(c), respectively. As can be seen from the figures, a time window size of 300 samples insuffices to resolve the two different breathing
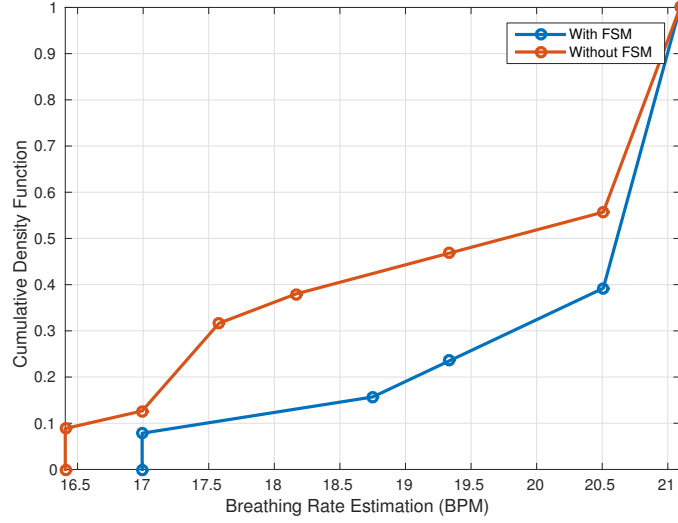
Figure 6.10: CDF performance with operating fan under single-person NLOS scenario with 20 BPM breathing rate.

rates. The resolvability improves when the window size enlarges to 450 samples and 600 samples, with respect to a duration of 45 seconds and 60 seconds. The accuracies of breathing rate estimations under the three window sizes are $[75.52\%, 96.54\%]$, $[90.33\%, 96.70\%]$, and $[99.61\%, 99.43\%]$, respectively.
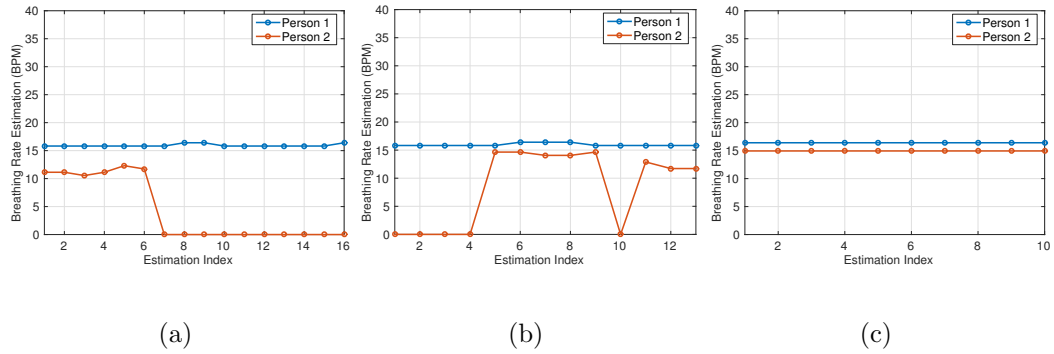
Figure 6.11: Two-person breathing rate estimation with FSM under (a) $C_{window} = 300$ (b) $C_{window} = 450$ (c) $C_{window} = 600$.

The breathing rate estimation results without FSM with $C_{window} = 300$,

$C_{window} = 450$, and $C_{window} = 600$ are demonstrated in Fig. 6.12(a), Fig. 6.12(b), and Fig. 6.12(c), respectively. In comparison with the results utilizing FSM, the performance degradation is very severe. In particular, when $C_{window} = 600$, the breathing rate of the second person cannot be recovered.

(a)   (b)   (c)
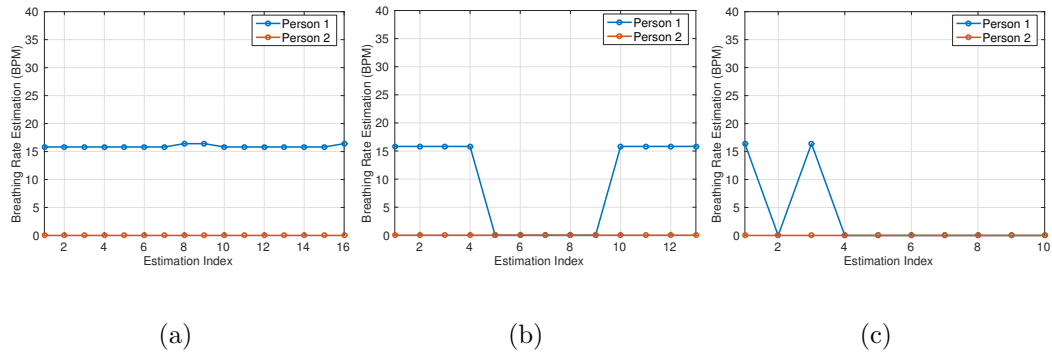
Figure 6.12: Two-person breathing rate estimation without FSM under (a) $C_{window} = 300$ (b) $C_{window} = 450$ (c) $C_{window} = 600$.
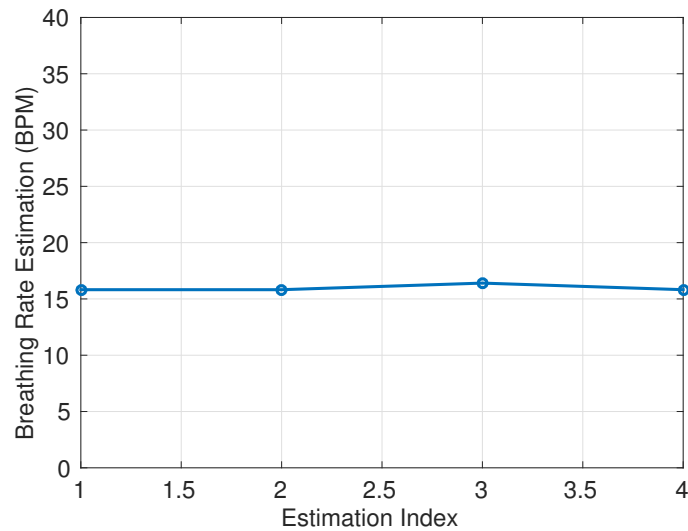
Figure 6.13: Breathing estimation with subject standing up for five seconds.

6.4.4.4 Impact of Large Motions

In Fig. 6.13, we demonstrate the performance of the proposed breathing tracking scheme when the subject stands up for five seconds and sits down during the measurement. Clearly, the proposed breathing tracking scheme overcomes the impact of such large motions and produce stable breathing rate estimations over time.

6.5 Summary

In this chapter, we have proposed a robust vital sign tracking scheme that analyzes the tiny temporal variations in the CFRs. On each antenna link, the proposed scheme transforms CFRs into CIRs and performs spectral analysis on the CIRs via FFT. The spectrum on different antenna links are then fused into one averaged spectrum. Then, persistence-based peak detection is performed on the spectrum which finally leads to the breathing rate estimation. Furthermore, we introduce FSM into the presented system such that the vital sign tracking system would adopt different thresholds in different states, and it significantly improves the robustness of vital sign trcking. Extensive experimental results validate that the proposed scheme could perform well for single-person as well as multi–person breathing tracking.

Chapter 7

Conclusions and Future Work

In this dissertation, we have presented two WiFi-based IPSs and two WiFi-based vital sign monitoring systems. The IPSs achieve $1 \sim 2$ centimeter level localization accuracy by exploiting the frequency and spatial diversity, which also leads to much improved robustness against environmental dynamics. On the other hand, the vital sign monitoring systems could perform multi-person breathing monitoring with very high accuracy and are also very robust against motion interference. The proposed systems utilize off-the-shelf WiFi and are infrastructure-free. Due to the excellent performances of the proposed schemes in real indoor environment, we strongly believe that they could be the solutions to the most crucial IoT applications.

7.1 Conclusions

In the first part of this dissertation, we introduce the CFR model for indoor localization and vital sign monitoring as well as the TR technique. Then, we present the method to calculate TRRS in SISO-OFDM and MIMO-OFDM systems to quantitatively evaluate the TR focusing effect and thus the similarity among CFRs. Based upon the scheme of TRRS calculation, we propose a WiFi-based IPS that could achieve $1 \sim 2$ centimeter localization accuracy under a strong NLOS

condition by exploiting the frequency diversity via frequency hopping, followed by a similar IPS which exploits the spatial diversity in MIMO-OFDM systems to achieve the same localization accuracy. In the second part of this dissertation, we present a vital sign monitoring system capable of monitoring the breathing rates of multiple people simultaneously with high accuracy with off-the-shelf WiFi devices. We then devise a robust breathing monitoring scheme which is also less computational intensive.

In Chapter 3, we propose a WiFi-based indoor localization scheme with $1 \sim 2$ centimeter accuracy utilizing the frequency diversity. With the help of the frequency hopping mechanism, the proposed scheme swipes a total bandwidth exceeding 1 GHz and collects CFRs from a large multitude of WiFi channels. During the offline phase, CFRs at locations-of-interest are collected and concatenated into location-specific fingerprints, while in the online phase, the TRRS values among the instantaneous CFR and those obtained in the offline phase are calculated which finally leads to the location estimation. The performance is evaluated by extensive experiments in a typical office environment that demonstrates the centimeter-level accuracy within an area of 20cm $\times$ 70 cm even under strong NLOS conditions.

In Chapter 4, a WiFi-based indoor localization system that exploits spatial diversity is proposed. Different from the IPS presented in Chapter 3, the proposed scheme collects CFRs from multiple antenna links available on MIMO-OFDM WiFi devices to obtain a much larger effective bandwidth. In comparison with the frequency hopping method, the proposed IPS is more efficient in terms of fingerprint acquisition. We conduct extensive experiments indoor which verify the centimeter-

level accuracy as well as robustness against environmental dynamics of the proposed IPS.

In Chapter 5, we present TR-BREATH, a WiFi-based vital sign monitoring scheme capable of high accuracy breathing rate estimation, breathing detection, and people counting. It leverages the highly accurate spectral analysis method, i.e., Root-MUSIC algorithm, to extract breathing rate candidates from the TRRS matrix calculated from CFRs in a period of time. Then, TR-BREATH performs affinity propagation on these candidates for clustering. The statistics of the clustering are used for breathing detection and people counting. Extensive experimental results demonstrate that the proposed scheme achieves a perfect breathing detection performance, an error of 1 people for people counting, and higher than 95% breathing rate estimation performance.

Lastly, in Chapter 6, we propose a robust vital sign tracking scheme with a much reduced computational complexity. The proposed scheme replaces the highly complicated Root-MUSIC algorithm in the architecture shown in Chapter 5 with FFT. To mitigate the impact of motions from the subject under monitoring as well as from other people nearby, we incorporate an FSM into the system such that the system could adjust the parameters automatically under different circumstances. We conduct extensive experiments with and without motion interferences which demonstrate the superiority of using FSM.

7.2   Future Work

There are several open problems and challenges to be explored and investigated before successful deployment of the proposed indoor localization system and vital sign monitoring system. The exploration of these issues could make the proposed IoT applications more versatile and useful in real life scenarios.

Firstly, the hardware consistency across different WiFi devices needs to be thoroughly studied. In particular, the hardware consistency must be guaranteed for the proposed IPS systems. This is because that a minor difference of the RF components might lead to a significantly reduced TR focusing effect and thus TRRS value. Since the proposed IPS compares CFRs via TRRS, the hardware inconsistency could lead to degraded localization performance. In this sense, we need to develop a metric to quantify the hardware consistency as well as devise an algorithm to compensate for the hardware inconsistency.

Secondly, the impact of RF interference on the proposed systems needs to be investigated. In this dissertation, we only take the co-existing WiFi devices into consideration. In fact, the environment could be much more hostile filled with many non-WiFi RF devices. They could inject a significant amount of interference into the operational frequency band of the proposed systems and thus affect their performances. Therefore, we need to investigate this issue and propose methods to counteract it.

Lastly, the proposed vital sign monitoring systems can be augmented with passive localization of the subjects under monitoring. This is important since dif-

ferent people with identical breathing rates cannot be resolved by the proposed systems due to the fact that the proposed systems separate different subjects by their breathing rates. This can be solved by incorporating geographical information of the subjects under monitoring.

Bibliography

[1] Bluetooth Technology. [Online]. Available: https://www.bluetooth.com/.

[2] Ettus Research LLC. [Online]. Available: http://www.ettus.com/.

[3] Extracting and Filtering Minima and Maxima of 1D Functions. [Online]. Available: https://people.mpi-inf.mpg.de/w̃einkauf/notes/persistence1d.html.

[4] GNU Radio. [Online]. Available: http://gnuradio.org/.

[5] Ubisense. [Online]. Available: http://ubisense.net/.

[6] Wi-Fi Alliance. [Online]. Available: https://www.wi-fi.org/.

[7] Z-wave. [Online]. Available: http://www.z-wave.com/.

[8] Zigbee Alliance. [Online]. Available: http://www.zigbee.org/.

[9] Heba Abdelnasser, Khaled A. Harras, and Moustafa Youssef. Ubibreathe: A ubiquitous non-invasive WiFi-based breathing estimator. In *Proceedings of the 16th ACM International Symposium on Mobile Ad Hoc Networking and Computing*, MobiHoc '15, pages 277–286, New York, NY, USA, 2015. ACM.

[10] Milton Abramowitz. *Handbook of Mathematical Functions, With Formulas, Graphs, and Mathematical Tables,*. Dover Publications, Incorporated, 1974.

[11] Fadel Adib, Hongzi Mao, Zachary Kabelac, Dina Katabi, and Robert C. Miller. Smart homes that monitor breathing and heart rate. In *Proceedings of the 33rd Annual ACM Conference on Human Factors in Computing Systems*, CHI '15, pages 837–846, New York, NY, USA, 2015. ACM.

[12] Frank Amoroso. Optimum realizable transmitter waveforms for high-speed data transmission. *IEEE Trans. Commun. Technol.*, 14(1):8–13, Feb 1966.

[13] Luigi Atzori, Antonio Iera, and Giacomo Morabito. The internet of things: A survey. *Computer Networks*, 54(15):2787 − 2805, 2010.

[14] P. Bahl and V.N. Padmanabhan. RADAR: an in-building RF-based user location and tracking system. In *Proc. IEEE INFOCOM*, volume 2, pages 775–784 vol.2, 2000.

[15] Bastian Bloessl, Michele Segata, Christoph Sommer, and Falko Dressler. Decoding IEEE 802.11a/g/p OFDM in Software using GNU Radio. In *19th ACM International Conference on Mobile Computing and Networking (MobiCom 2013), Demo Session*, pages 159–161, Miami, FL, October 2013. ACM.

[16] B.P. Bogert. Demonstration of delay distortion correction by time-reversal techniques. *Communications Systems, IRE Transactions on*, 5(3):2–7, December 1957.

[17] Christopher J. C. Burges. A tutorial on support vector machines for pattern recognition. *Data Min. Knowl. Discov.*, 2(2):121–167, June 1998.

[18] Bradford Campbell, Prabal Dutta, Benjamin Kempke, Ye-Sheng Kuo, and Pat Pannuto. Decawave: Exploring state of the art commercial localization. *Ann Arbor*, 1001:48109.

[19] Y. Chapre, A. Ignjatovic, A. Seneviratne, and S. Jha. CSI-MIMO: Indoor Wi-Fi fingerprinting system. In *Local Computer Networks (LCN), 2014 IEEE 39th Conference on*, pages 202–209, Sept 2014.

[20] C. Chen, Y. Han, Y. Chen, H. Q. Lai, F. Zhang, B. Wang, and K. J. R. Liu. Tr-breath: Time-reversal breathing rate estimation and detection. *IEEE Trans. Biomed. Eng.*, PP(99):1–1, 2017.

[21] Chen Chen, Yi Han, Yan Chen, and K. J. Ray Liu. Multi-person breathing rate estimation using time-reversal on WiFi platforms. In *2016 IEEE Global Conference on Signal and Information Processing (GlobalSIP)*, December 2016. To appear.

[22] Y. Chen, B. Wang, Y. Han, H. Q. Lai, Z. Safar, and K. J. R. Liu. Why Time Reversal for Future 5G Wireless? [Perspectives]. *IEEE Signal Processing Mag.*, 33(2):17–26, March 2016.

[23] Yan Chen, Feng Han, Yu-Han Yang, Hang Ma, Yi Han, Chunxiao Jiang, Hung-Quoc Lai, D. Claffey, Z. Safar, and K .J. R. Liu. Time-reversal wireless paradigm for green Internet of Things: An overview. *IEEE Internet Things J.*, 1(1):81–98, Feb 2014.

[24] Tzi-Dar Chiueh and Pei-Yun Tsai. *OFDM Baseband Receiver Design for Wireless Communications*. John Wiley and Sons (Asia) Pte Ltd, 2007.

[25] D. Ciuonzo, G. Romano, and R. Solimene. Performance analysis of time-reversal music. *IEEE Trans. Signal Processing*, 63(10):2650–2662, May 2015.

[26] D. Ciuonzo and P. S. Rossi. Noncolocated Time-Reversal MUSIC: High-SNR Distribution of Null Spectrum. *IEEE Signal Processing Lett.*, 24(4):397–401, April 2017.

[27] A. J. Devaney. Time reversal imaging of obscured targets from multistatic data. *IEEE Trans. Antennas Propagat.*, 53(5):1600–1610, May 2005.

[28] C. Dorme, M. Fink, and C. Prada. Focusing in transmit-receive mode through inhomogeneous media: The matched filter approach. In *Ultrasonics Symposium, 1992. Proceedings., IEEE 1992*, pages 629–634 vol.1, Oct 1992.

[29] M. Fink, C. Prada, F. Wu, and D. Cassereau. Self focusing in inhomogeneous media with time reversal acoustic mirrors. In *Ultrasonics Symposium, 1989. Proceedings., IEEE 1989*, pages 681–686 vol.2, Oct 1989.

[30] Mathias Fink. Acoustic time-reversal mirrors. In Mathias Fink, WilliamA. Kuperman, Jean-Paul Montagner, and Arnaud Tourin, editors, *Imaging of Complex Media with Acoustic and Seismic Waves*, volume 84 of *Topics in Applied Physics*. Springer Berlin Heidelberg, 2002.

[31] Strategic Business Insights (Firm) and National Intelligence Council (U.S.). *Disruptive Civil Technologies: Six Technologies with Potential Impacts on US Interests Out to 2025 : Biogerontechnology, Energy Storage Materials, Biofuels and Bio-based Chemicals, Clean Coal Technologies, Service Robotics, the Internet of Things*. National Intelligence Council, 2008.

[32] Brendan J. Frey and Delbert Dueck. Clustering by passing messages between data points. *Science*, 315:2007, 2007.

[33] Jon Gjengset, Jie Xiong, Graeme McPhillips, and Kyle Jamieson. Phaser: Enabling Phased Array Signal Processing on Commodity WiFi Access Points. In *Proceedings of the 20th Annual International Conference on Mobile Computing and Networking*, MobiCom '14, pages 153–164, New York, NY, USA, 2014. ACM.

[34] Andrea Goldsmith. *Wireless Communications*. Cambridge University Press, New York, NY, USA, 2005.

[35] Feng Han, Yu-Han Yang, Beibei Wang, Yongle Wu, and K .J. R. Liu. Time-reversal division multiple access over multi-path channels. *IEEE Trans. Commun.*, 60(7):1953–1965, July 2012.

[36] Y. Han, Y. Chen, B. Wang, and K. J. Ray Liu. Enabling heterogeneous connectivity in internet of things: A time-reversal approach. *IEEE Internet of Things Journal*, 3(6):1036–1047, Dec 2016.

[37] Jeffrey Hightower, Roy Want, and Gaetano Borriello. SpotON: An indoor 3D location sensing technology based on RF signal strength. UW CSE 00-02-02, University of Washington, Department of Computer Science and Engineering, Seattle, WA, February 2000.

[38] Y. Jin and J. M. F. Moura. Time-reversal detection using antenna arrays. *IEEE Trans. Signal Processing*, 57(4):1396–1414, April 2009.

[39] MC Kearon, E Summers, NL Jones, EJ Campbell, and KJ Killian. Breathing during prolonged exercise in humans. *The Journal of physiology*, 442:477, 1991.

[40] Jian Liu, Yan Wang, Yingying Chen, Jie Yang, Xu Chen, and Jerry Cheng. Tracking vital signs during sleep leveraging off-the-shelf WiFi. In *Proceedings*

of the 16th ACM International Symposium on Mobile Ad Hoc Networking and Computing, MobiHoc '15, pages 267–276, 2015.

[41] J. MacQueen. Some methods for classification and analysis of multivariate observations. In *Proceedings of the Fifth Berkeley Symposium on Mathematical Statistics and Probability, Volume 1: Statistics*, pages 281–297, Berkeley, Calif., 1967. University of California Press.

[42] J.M.F. Moura and Yuanwei Jin. Detection by time reversal: Single antenna. *IEEE Trans. Signal Processing*, 55(1):187–201, Jan 2007.

[43] John F. Murray. *The normal lung : the basis for diagnosis and treatment of pulmonary disease / John F. Murray.* Saunders Philadelphia, 1976.

[44] L.M. Ni, Yunhao Liu, Yiu Cho Lau, and A.P. Patil. LANDMARC: indoor location sensing using active RFID. In *Pervasive Computing and Communications, 2003. (PerCom 2003). Proceedings of the First IEEE International Conference on*, pages 407–415, March 2003.

[45] Shahriar Nirjon, Jie Liu, Gerald DeJean, Bodhi Priyantha, Yuzhe Jin, and Ted Hart. Coin-GPS: indoor localization from direct GPS receiving. In *Proceedings of the 12th annual international conference on Mobile systems, applications, and services*, pages 301–314. ACM, 2014.

[46] F. Pancaldi, G. M. Vitetta, R. Kalbasi, N. Al-Dhahir, M. Uysal, and H. Mheidat. Single-carrier frequency domain equalization. *IEEE Signal Processing Magazine*, 25(5):37–56, September 2008.

[47] Byung-Kwon Park, S. Yamada, O. Boric-Lubecke, and V. Lubecke. Single-channel receiver limitations in doppler radar measurements of periodic motion. In *Radio and Wireless Symposium, 2006 IEEE*, pages 99–102, Jan 2006.

[48] P. Prasithsangaree, P. Krishnamurthy, and P.K. Chrysanthis. On indoor position location with wireless LANs. In *Personal, Indoor and Mobile Radio Communications, 2002. The 13th IEEE International Symposium on*, volume 2, pages 720–724 vol.2, Sept 2002.

[49] B. D. Rao and K. V. S. Hari. Performance analysis of root-music. *IEEE Trans. Acoust., Speech, Signal Processing*, 37(12):1939–1949, Dec 1989.

[50] S. Savazzi, S. Sigg, M. Nicoli, V. Rampa, S. Kianoush, and U. Spagnolini. Device-free radio vision for assisted living: Leveraging wireless channel quality information for human sensing. *IEEE Signal Processing Magazine*, 33(2):45–58, March 2016.

[51] R. Schmidt. Multiple emitter location and signal parameter estimation. *IEEE Trans. Antennas Propagat.*, 34(3):276–280, Mar 1986.

[52] Souvik Sen, Božidar Radunovic, Romit Roy Choudhury, and Tom Minka. You are facing the Mona Lisa: Spot localization using PHY layer information. In *Proceedings of the 10th International Conference on Mobile Systems, Applications, and Services*, MobiSys '12, pages 183–196, New York, NY, USA, 2012. ACM.

[53] M. Speth, S. Fechtel, G. Fock, and H. Meyr. Optimum receiver design for OFDM-based broadband transmission II: A case study. *IEEE Trans. Commun.*, 49(4):571 –578, apr 2001.

[54] M. Speth, S.A. Fechtel, G. Fock, and H. Meyr. Optimum receiver design for wireless broad-band systems using OFDM—Part I. *IEEE Trans. Commun.*, 47(11):1668 –1677, nov 1999.

[55] G.L. Stuber, J.R. Barry, S.W. McLaughlin, Ye Li, M.A. Ingram, and T.G. Pratt. Broadband MIMO-OFDM wireless communications. *Proceedings of the IEEE*, 92(2):271–294, Feb 2004.

[56] J. J. van de Beek, O. Edfors, M. Sandell, S. K. Wilson, and P. O. Borjesson. On channel estimation in ofdm systems. In *1995 IEEE 45th Vehicular Technology Conference. Countdown to the Wireless Twenty-First Century*, volume 2, pages 815–819 vol.2, Jul 1995.

[57] J.J. van de Beek, M. Sandell, and P.O. Borjesson. ML estimation of time and frequency offset in OFDM systems. *IEEE Trans. Signal Processing*, 45(7):1800 –1805, jul 1997.

[58] Deepak Vasisht, Swarun Kumar, and Dina Katabi. Decimeter-level localization with a single wifi access point. In *13th USENIX Symposium on Networked Systems Design and Implementation (NSDI 16)*, pages 165–178, Santa Clara, CA, March 2016. USENIX Association.

[59] B. Wang, Y. Wu, F. Han, Y.H Yang, and K. J. R. Liu. Green wireless communications: A time-reversal paradigm. *IEEE J. Select. Areas Commun.*, 29(8):1698–1710, September 2011.

[60] C. Wu, Z. Yang, and Y. Liu. Smartphones based crowdsourcing for indoor localization. *IEEE Transactions on Mobile Computing*, 14(2):444–457, Feb 2015.

[61] Z. Wu, Y. Han, Y. Chen, and K. J. R. Liu. A time-reversal paradigm for indoor positioning system. *IEEE Trans. Veh. Commun.*, 64(4):1331–1339, April 2015.

[62] J. Xiao, Wu K.S., Y. Yi, and L.M. Ni. FIFS: Fine-grained indoor fingerprinting system. In *Computer Communications and Networks (ICCCN), 2012 21st International Conference on*, pages 1–7, July 2012.

[63] Jie Xiong and Kyle Jamieson. Arraytrack: A fine-grained indoor location system. In *Proceedings of the 10th USENIX Conference on Networked Systems*

Design and Implementation, NSDI'13, pages 71–84, Berkeley, CA, USA, 2013. USENIX Association.

[64] Q. Xu, Y. Chen, B. Wang, and K. J. R. Liu. Radio biometrics: Human recognition through a wall. *IEEE Transactions on Information Forensics and Security*, 12(5):1141–1155, May 2017.

[65] Q. Xu, Y. Chen, B. Wang, and K. J. R. Liu. Trieds: Wireless events detection through the wall. *IEEE Internet of Things Journal*, 4(3):723–735, June 2017.

[66] Z. Yang, Z. Zhou, and Y. Liu. From RSSI to CSI: Indoor localization via channel response. *ACM Computing Surveys (CSUR)*, 46(2):25–1, 2013.

[67] M. Youssef and A. Agrawala. The Horus WLAN location determination system. In *Proceedings of the 3rd International Conference on Mobile Systems, Applications, and Services*, MobiSys '05, pages 205–218, New York, NY, USA, 2005. ACM.

[68] F. Zhang, C. Chen, B. Wang, H. Q. Lai, and K. J. R. Liu. A time-reversal spatial hardening effect for indoor speed estimation. In *2017 IEEE International Conference on Acoustics, Speech and Signal Processing (ICASSP)*, pages 5955–5959, March 2017.

[69] Junxing Zhang, Mohammad H. Firooz, Neal Patwari, and Sneha K. Kasera. Advancing wireless link signatures for location distinction. In *Proceedings of the 14th ACM international conference on Mobile computing and networking*, MobiCom '08, pages 26–37, New York, NY, USA, 2008. ACM.

[70] Q. Zhang, C. H. Foh, B. C. Seet, and A. C. M. Fong. RSS Ranging Based Wi-Fi Localization for Unknown Path Loss Exponent. In *Global Telecommunications Conference (GLOBECOM 2011), 2011 IEEE*, pages 1–5, Dec 2011.